POLARIZABILITY AND MAGIC-ZERO WAVELENGTH MEASUREMENTS OF ALKALI ATOMS

by

William Frederick Holmgren

———————————————

A Dissertation Submitted to the Faculty of the

DEPARTMENT OF PHYSICS

In Partial Fulfillment of the Requirements
For the Degree of

DOCTOR OF PHILOSOPHY

In the Graduate College

THE UNIVERSITY OF ARIZONA

2013

THE UNIVERSITY OF ARIZONA
GRADUATE COLLEGE

As members of the Dissertation Committee, we certify that we have read the dissertation prepared by William Frederick Holmgren
entitled Polarizability and magic-zero wavelength measurements of alkali atoms
and recommend that it be accepted as fulfilling the dissertation requirement for the Degree of Doctor of Philosophy.

_____   Date: 2 April 2013
   Alexander D. Cronin

_____   Date: 2 April 2013
   Arvinder Sandhu

_____   Date: 2 April 2013
   Charles S. Stafford

_____   Date: 2 April 2013
   Brian P. Anderson

Final approval and acceptance of this dissertation is contingent upon the candidate's submission of the final copies of the dissertation to the Graduate College.
I hereby certify that I have read this dissertation prepared under my direction and recommend that it be accepted as fulfilling the dissertation requirement.

_____   Date: 2 April 2013
   Dissertation Director: Alexander D. Cronin

STATEMENT BY AUTHOR

SIGNED: William Frederick Holmgren

TABLE OF CONTENTS

TABLE OF CONTENTS – *Continued*

LIST OF FIGURES

LIST OF FIGURES – *Continued*

LIST OF TABLES

ABSTRACT

Atomic polarizability plays an essential role in topics ranging from van der Waals interactions, state lifetimes, and indices of refraction, to next generation atomic clocks and atomic parity non-conservation experiments. Polarizability measurements, such as the ones described in this thesis, provide valuable input to these subjects and serve as benchmark tests for sophisticated atomic structure calculations. We measured the static polarizability of potassium and rubidium with record precision and 0.5% uncertainty using a Mach-Zehnder atom interferometer with an electric-field gradient. To support future precision measurements of polarizability, we developed a new atom beam velocity measurement technique called phase choppers. Using phase choppers, we demonstrated measurements of mean atom beam velocity with an uncertainty of 0.1%. We also developed a new way to probe atomic structure: a measurement of a zero-crossing of the dynamic polarizability of potassium, known as a magic-zero wavelength. We measured the first magic-zero wavelength of potassium with 1.5 pm uncertainty and established a new benchmark measurement for the ratio of the D1 and D2 line strengths. Finally, we propose the use of a resonant photoionization detector for measurements of strontium polarizability, and the use of contrast interferometry for measurements of alkali dimer tensor polarizabilities.

CHAPTER 1

INTRODUCTION

What happens to an atom in an electric field? An atom is a neutral particle so it will not accelerate in a uniform electric field, however, it is composed of positively charged protons and negatively charged electrons that do feel electric forces. If we place our test atom in a charged parallel-plate capacitor, the negatively charged electrons tend to move toward the positively charged surface, while the much heavier and positively charged nucleus moves only slightly toward the negatively charged surface. As a result of these movements, the atom becomes stretched out by an amount determined by its *polarizability*. Figure 1.1 shows a cartoon of this idea. The polarizability of a spherical particle is proportional to its volume and this remains approximately true for atoms as well. As such, polarizability is conveniently expressed in terms of a volume, typically a_0^3 or 10^{-24} cm^3. The SI unit of polarizability, C m^2/V, can be reduced to a volume by simply dividing by $4\pi\epsilon_0$.

More precisely, the polarizability α of an atom relates the induced dipole moment $\vec{p}$ to the applied electric field $\vec{E}$ by

$$\vec{p} = \alpha\vec{E} + ... \tag{1.1}$$

The dipole moment is $\vec{p} = e\vec{r}$, where $\vec{r}$ is the displacement of the electron cloud. Higher order terms, such as the hyperpolarizability, will be neglected in this work since we operate our experiments at more than 10^5 times below the scale of the atomic field ($\vec{E}_a \approx e/a_0^2 = 5 \times 10^{11}$ V/m).

The energy shift of a polarizable particle in an electric field is given by

$$U = -\frac{1}{2}\alpha\vec{E}^2, \tag{1.2}$$
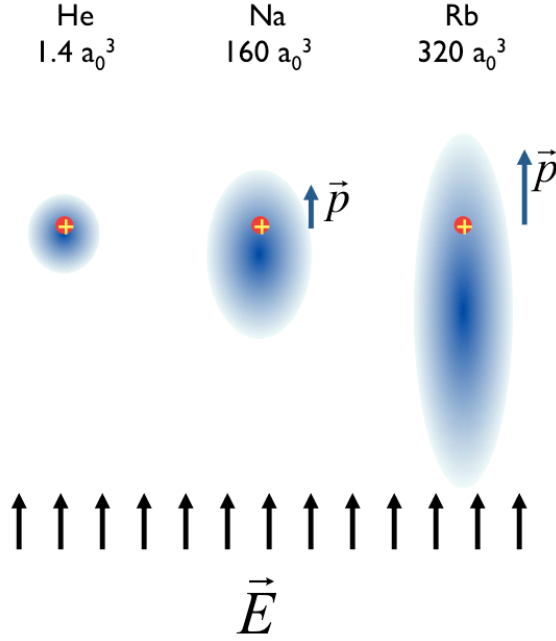
Figure 1.1: An electric field applied to three different atoms, helium, sodium, and rubidium, induces a dipole moment in proportion to the atomic polarizability. The polarizability roughly scales in proportion to the volume of the atom.

and this is commonly referred to as the Stark shift. Polarizability can also be defined through 2nd-order perturbation theory. The Hamiltonian of a polarizable particle is

$$H = H_{\text{atom}} - \hat{p} \cdot \vec{E} \tag{1.3}$$

where $\hat{p}$ is the dipole operator. Application of 2nd order perturbation theory leads to a ground-state static polarizability of

$$\alpha = 2e^2 \sum_{i \neq 0} \frac{|\langle i|\vec{r}.\vec{E}|0\rangle|^2}{E_i} \tag{1.4}$$

where e is the electron charge and E_i is the energy of the ith atomic state, assuming $E_0 \equiv 0$. So far we have assumed that the applied field is constant in time, but we will examine the frequency dependence of the dynamic polarizability in sections 2.3

and 5.1.

Equation 1.4 gives us insight into why polarizability is an interesting property to study: it can be expressed as a sum of dipole matrix elements. These matrix elements also describe properties such as transition strengths, state lifetimes, van der Waals interactions, indices of refraction, and scattering cross-sections, just to name a few. In fact, in a 1966 review of atomic polarizabilities, Bederson and Robinson referred to polarizability as a "seemingly ubiquitous parameter" [1] and T.M. Miller compiled a list of properties directly related to polarizability with more than 15 entries [2]. Since dipole matrix elements are notoriously difficult to calculate, experiments such as the ones described in this thesis can serve as input to a long list of calculations.

New applications of atomic physics continue to demand better knowledge of atomic polarizabilities. Next generation optical lattice clocks based on strontium and ytterbium atoms suffer from significant frequency shifts due to blackbody radiation and accurate calibration of these frequency shifts requires precise knowledge of polarizabilities [3, 4]. Parity non-conservation studies [5, 6] using atomic systems impose limits on physics beyond the standard model, but require accurate atomic structure calculations to interpret the measurements [7]. Polarizability measurements are some of the best ways to test these calculations.

This thesis describes three experiments all concerned with precisely answering the seemingly simple question of what happens to an atom in an electric field. The most important findings are as follows:

- I used an atom interferometer and a novel electric field gradient geometry to measure the polarizabilities of K and Rb with unprecedented precision (0.5% uncertainty) [8]. These measurements are now listed in the CRC Handbook of Chemistry and Physics, and they establish a roadmap for future polarizability measurements in our lab.

- I developed a new technique to measure atom beam velocities with 0.1% uncertainty using phase choppers [9]. This technique will enable more precise

polarizability measurements.

- I measured a wavelength, referred to as a magic-zero wavelength, for which the dynamic polarizability of potassium equals zero. We measured the first, i.e. the longest, magic-zero wavelength of potassium with 1.5 pm uncertainty [10]. I explain how this is a novel method to test atomic structure calculations and also establishes a foundation for future measurements of magic-zero wavelengths in our lab.

The remainder of this introduction provides a brief history of polarizability measurements and a review of the basic matterwave optics needed for understanding the experiments in this thesis. Chapter 2 summarizes the experiments, papers, and proposals that comprise this thesis work. Chapters 3-5 provide supporting material for our peer-reviewed publications on static polarizability measurements of Na, K, and Rb (Appendix A) [8], a new atom velocity measurement technique using phase choppers that will improve polarizability measurements (Appendix B) [9], and a measurement of the first magic-zero wavelength of the dynamic polarizability of potassium (Appendix C) [10]. Chapters 6 and 7 propose two new experiments: measurements of Sr polarizability using a resonant photoionization detector and measurements of the tensor polarizabilities of alkali dimers.

1.1 A brief history of polarizability measurements

In this section we provide a brief review of the history of polarizability measurements. For comprehensive reviews of polarizability measurements, see Mitroy, Safronova and Clark (2010) [11], Gould and Miller (2005) [12], Hohm (2000) [13], Miller and Bederson (1989) [14], Miller and Bederson (1978) [15], Bederson and Robinson (1966) [1], and the CRC Handbook of Chemistry and Physics [2].

Scheffers and Stark started the business of polarizability measurements in 1934 [16] by deflecting atomic beams of Li, K, and Cs in an inhomogenous electric field. More than 25 years later, Benjamin Bederson developed the E-H gradient spectrometer at NYU [17] and in 1961 made the first measurements of polarizabilities

since Stark [18]. These measurements were made with about 15% uncertainty and formed the foundation for a career's worth of impressive polarizability measurements discussed below.

In 1974, *Physical Review A* published two landmark polarizability measurement papers. Hall and Zorn [19] measured the polarizabilities of the alkalis Na through Cs with 7% uncertainty using beam deflection, and Molof, Schwartz, Miller, and Bederson [20] measured the polarizabilities of Li through Cs and the $^3P_2$ metastable nobel gas atoms with 2% uncertainty using the E-H gradient balance technique. Molof *et al.* provided measurements of polarizability unmatched for over 2 decades and has been cited over 200 times. Molof *et al.* achieved their relatively low uncertainties by measuring polarizabilities with respect to the polarizability of metastable He, which can be calculated with high precision. In this thesis, we continue the technique of using ratio measurements of polarizabilities for improved precision.

The Bederson group also measured the average dipole polarizabilities of homonuclear alkali dimers with 10% uncertainty in 1974 by using ratios with respect to the polarizabilities of the alkali atoms [21]. The polarizabilities of Ba, Sr [22] and Ca [23] were also measured with respect to Li over the next two years. In 1993, Tarnovsky *et al.* measured the polarizabilities of both the homonuclear and heteronuclear alkali dimers with Bederson [24]. These measurements were made with 6-10% uncertainty.

The 1990s saw the advent of atom interferometry and its promise of high precision measurements of atomic properties [25, 26, 27], fundamental constants of nature [28], and inertial displacements [29, 30]. The Pritchard group at MIT made the first interferometry-based precision polarizability measurement of an atom, Na, with 0.35% uncertainty using a three nanograting Mach-Zehnder atom interferometer [25]. In Toulouse, the Vigué group measured the polarizability of Li with 0.66% uncertainty using an atom beam interferometer with light gratings [26]. The Arndt group in Vienna measured the polarizability of C_{60} and C_{70} with 6% uncertainty and their ratio with 2.5% uncertainty using a near field interferometer [31].

The development of laser trapping and cooling enabled several new polarizability measurements, as well. The Sackett group in Virginia measured the dynamic

polarizability of Rb near the D1 and D2 lines with 7% uncertainty using a guided ultracold atom interferometer [32]. Amini and Gould used an atomic fountain to measure the polarizability of Cs with 0.14% uncertainty [33]. This measurement provides a valuable benchmark for calculations [7, 34] needed to interpret atomic parity non-conservation experiments [5]. Cold atom experiments offer much longer interaction times than atom beam experiments and ultracold atom interferometers may offer better than shot-noise limited precision. However, these experiments often suffer from additional systematic errors, such as density-dependent phase shifts, and therefore independent measurements provide valuable cross-checks.

Other notable measurements of polarizabilities of non-alkali or alkaline-earth atoms include the following. Schäfer *et al.* measured the polarizability of lead clusters using beam deflection [35]. The Bederson group also made measurements of the polarizability of mercury [36], indium [37], and the alkali halide dimers [38]. Knight *et al.* measured the polarizability of sodium clusters [39]. The Kresin group at UCLA measured the polarizability of sodium clusters [40] using electrodes from the Bederson group. These measurements all have uncertainties on the order of a few percent.

Mitroy, Safronova, and Clark recently wrote a comprehensive review of the theory of atomic polarizabilities with extensive references [11]. In addition, I recommend references [41, 42, 43, 44, 45, 46, 47] to trace the progress of polarizability calculation techniques through the past half-century.

I provide a recommendation for the best measurements and calculations of polarizability of the alkali atoms in Table 1.1. The theoretical uncertainty of polarizability for most alkalis is about 0.1%, while the measurement uncertainty is 0.2-0.5%. Note that our measurements of potassium and rubidium polarizability presented in this thesis are the best available.

Techniques developed in this thesis, specifically the use of ratio measurements of polarizability and the ability to measure the polarizability of heavy atoms using an atom beam interferometer, will enable measurements of alkali atom polarizabilities with better than 0.1% uncertainty. As I explain in Chapter 3 and Appendix B, we

Table 1.1: Recommended measured and calculated values of alkali static polariz-abilities in units of 10^{-24} cm^3. Some calculations rely on measurements of atomic properties. See Mitroy *et al.* [11] for more details.

Atom	α_{meas}		α_{calc}	
Li	24.33(16)	[26]	24.318(4)	[48]
Na	24.11(8)	[25]	24.09(4)	[44]
K	43.06(21)	[8]	42.91(9)	[49]
Rb	47.24(21)	[8]	47.17(9)	[50]
Cs	59.42(8)	[33]	59.26(3)	[44]

have demonstrated measurements of cesium polarizability with a precision of 0.1%, but not yet this accuracy.

1.2   Matterwave optics

Matterwave optics and atom interferometry is now a mature tool that has been extensively described in numerous reviews [51, 52, 53, 54, 55], primary references [56, 57, 58, 59, 60, 61, 62, 63], and Ph.D. theses [64, 65, 66, 67, 68]. Here, I summarize only the essential principles of our particular atom interferometer to provide background for the measurements described later in this thesis.

Our atom beam is created by supersonic expansion [69, 70] of an inert carrier gas seeded with alkali atoms and collimated with two small slits. A translatable hot-wire detector [71] and channel electron multiplier measures the atom beam flux. See V.P.A. Lonij's thesis, section 2.2, for more details of our updated atom beam source and detector [68].

A silicon-nitride nanograting diffracts the collimated atom beam, just as a traditional grating will diffract light waves. The path separation after the first grating is

$$s = \frac{\lambda_{dB}}{d_g} z = \frac{h}{mvd_g} z \qquad (1.5)$$
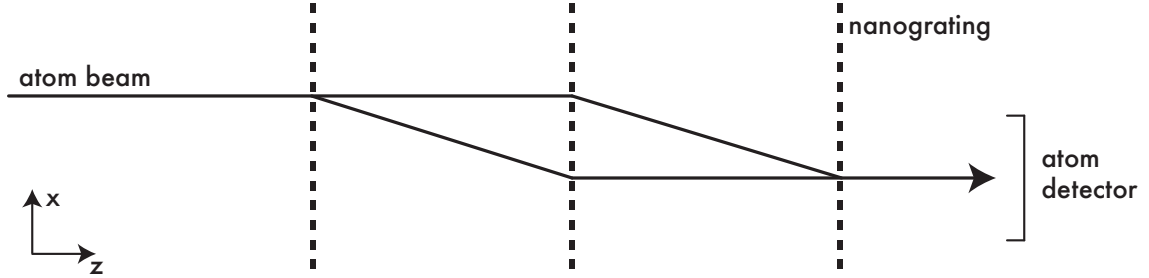
Figure 1.2: A three grating Mach-Zehnder atom interferometer. Atoms waves diffracted by the first and second nanogratings form an interference pattern at the third nanograting. A hot-wire detector measures the transmitted atom beam flux.

where $\lambda_{dB} = h/mv$ is the de Broglie wavelength of an atom with mass m and velocity v, $d_g = 100$ nm is the grating period, and z is the propagation distance from the first grating. For typical beam conditions in our experiments $\lambda_{dB} \approx 5$ pm, and this results in a diffraction angle of 50 μrad. Lonij *et al.* [72, 73] and Perreault *et al.* [74] used atom beam diffraction to study atom surface interactions.

We use a three-grating Mach-Zehnder atom interferometer (Figure 1.2) to make precision measurements of atomic properties. This interferometer is an evolution of the machine developed in Dave Pritchard's group at MIT in the 1980s and 1990s [56, 52, 64]. A superposition of two traveling waves, created by diffraction from the first and second nanogratings, forms a sinusoidal interference pattern in space at the plane of the third nanograting. These two traveling waves may be written as

$$\psi_0 = A e^{i(k_z z + \phi_0)} \tag{1.6}$$

$$\psi_1 = B e^{i(k_z z + k_x x + \phi_1)}. \tag{1.7}$$

The transverse wavenumber is determined by the period of the nanogratings: $k_x = 2\pi/d_g$.

The superposition of traveling waves overlaps at the location of the 3rd nanograt-

ing and make a probability of detecting each atom at location x given by

$$
\begin{aligned}
|\psi|^2 &= |\psi_0 + \psi_1|^2 \\
&= A^2 + B^2 + AB \left(e^{i(k_x x + \delta_\phi)} + e^{-i(k_x x + \delta_\phi)} \right) \\
&= A^2 + B^2 + 2AB \cos(k_x x + \delta_\phi) \quad\quad\quad (1.8)
\end{aligned}
$$

where $\delta_\phi = \phi_1 - \phi_0$. The probability density is described by a constant value plus a term that oscillates with a spatial frequency equal to the nanograting period, regardless of the atomic velocity $v = \hbar k_z / m$. As such, we can use a 3rd nanograting as a mask of the interference pattern. The transmitted flux, $I(x)$, can be written in terms of an average beam flux I_0, contrast C, and phase δ_ϕ:

$$
I(x) = I_0 + C \cos(k_x x + \delta_\phi). \quad\quad\quad (1.9)
$$

Moving any of the nanogratings in the x direction scans the atomic interference pattern across the third nanograting to yield intensity vs. position data. A co-propogating laser interferometer measures the relative position of the three nanogratings. Figure 1.3 shows an example of the atom interference fringe data.

The observed fringe pattern is the incoherent sum of the sinusoidal probability distributions from single-atom interference, repeated about 10^5 times per second. Different atoms have different velocities and also enter and exit the interferometer at different times. Atoms do not interfere with other atoms in our interferometer, only with themselves, because they are separated from other atoms by tens of micrometers on average. These characteristics are crucial for understanding contrast loss in our interferometer, and in particular the new velocity measurement technique described in section 2.2 and Appendix B.

Application of, say, an electric field gradient across the interferometer changes δ_ϕ and results in a measurable phase shift. We analyze these phase shifts to determine properties such as atomic polarizability, described in section 2.1 and Appendix A, and magic-zero wavelengths, described in section 2.3 and Appendix C.
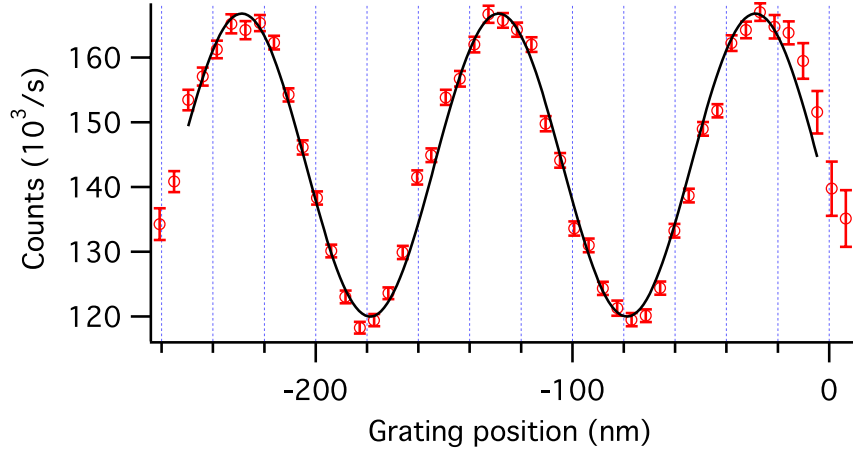
Figure 1.3: A typical atom interference fringe from our Mach-Zehnder atom interferometer determined from 5 sec of data. We fit this data to find the fringe contrast C and phase ϕ.

The phase of the atom waves along each path evolve according to

$$\phi = \frac{1}{\hbar} \int E(t)dt \tag{1.10}$$

where $E(t)$ is the total energy of the atom as a function of time. All of the phase shifts described in this thesis are created by energy shifts (~ 1 μeV) much smaller than the kinetic energy of the atoms (~ 0.1 eV), and much more slowly varying (~ 100 μm) than the de Broglie wavelength (~ 10 pm). These are, loosely, the conditions for the application of the WKB approximation. In the WKB approximation the phase is described by

$$\phi = \frac{1}{\hbar} \int p(z)dz \tag{1.11}$$

where

$$p(z) = \sqrt{2m(E - U(z))} \tag{1.12}$$

is the momentum of the atom. Since $U(z) \ll E$ we can simplify the phase:

$$\phi \quad = \quad \frac{\sqrt{2mE}}{\hbar} \int \sqrt{1 - \frac{U(z)}{E}} dz \tag{1.13}$$

$$\approx \quad \frac{\sqrt{2mE}}{\hbar} \int \left(1 - \frac{U(z)}{2E}\right) dz. \tag{1.14}$$

The first term will be common to both paths and not measurable, so we drop it from consideration. The second term corresponds to the change in phase of the wavefunction due to the application of a potential. Finally, plugging in the kinetic energy $mv^2/2$ for the total energy yields a phase shift of

$$\phi = -\frac{1}{\hbar v} \int U(z) dz. \tag{1.15}$$

Typical interaction distances in our experiments are 100 μm to 10 mm and at a typical atom beam velocity of $v_0 = 2000$ m/s, this corresponds to interaction times of 50 ns to 5 μs. As stated previously, the energy shift of a polarizable atom is given by

$$U(\omega) = -\frac{1}{2}\alpha(\omega)\vec{E}^2(\omega, z, t) \tag{1.16}$$

where we now allow for a frequency dependence for the polarizability and the electric field. Our static polarizability measurements investigate this energy shift in the limit $\omega \to 0$ and our magic-zero wavelength measurement investigates the frequency at which $\alpha(\omega)$, and thus $U(\omega)$, vanishes.

Depending on the geometry of the interaction region, both paths of the atom interferometer may receive a phase shift. However, we only measure the difference in the phase shifts along two interferometer paths. We refer to this as the differential phase shift. The experiments described in this thesis all apply phase shifts to both paths of the interferometer. Section 2.1 discusses some of the advantages of this configuration, such as the fact that it enables us to use heavier atoms that produce unresolved diffraction orders.

As discussed above, the measured interference pattern is the ensemble average of single-atom interference patterns. In general, interferometer phase shifts may be a function of many parameters, such as the atom velocity v, transverse position x, or the atomic state. For example, equation 1.15 shows that the phase shift is a function of the atom beam velocity. Our supersonic atom beam contains atoms with a narrow, but still significant velocity distribution $P(v)$. Figure 1.4 shows examples of typical velocity distributions in our interferometer. We use polar notation in the complex plane to more easily and compactly express and calculate the ensemble average of interference fringes. For the case of averaging over only a velocity distribution the expression is

$$C_m e^{i\phi_m} = C_0 e^{i\phi_0} \int_{v=0}^{\infty} P(v) e^{i\phi(v)} dv \qquad (1.17)$$

where $\phi(v)$ is the velocity-dependent differential phase shift, C_m are ϕ_m are the measured interferometer contrast and phase, respectively, and C_0 are ϕ_0 are the interferometer phase and contrast in the absence of the phase shift. We typically evaluate equations such as 1.17 by numerical integration of the real and imaginary parts of the right side of the equation. Then, C_m is given by the magnitude of the complex number on the right side of the equation, and ϕ_m is given by the polar angle. In the limit that $P(v) \rightarrow \delta(v - v_0)$ we obtain $\phi_m = \phi_0 + \phi(v_0)$ and $C_m = C_0$, as expected. Additional parameters, such as the transverse beam position, may be averaged over in a similar fashion. The distribution of phase shifts associated with these parameters typically leads to contrast loss in the interferometer.
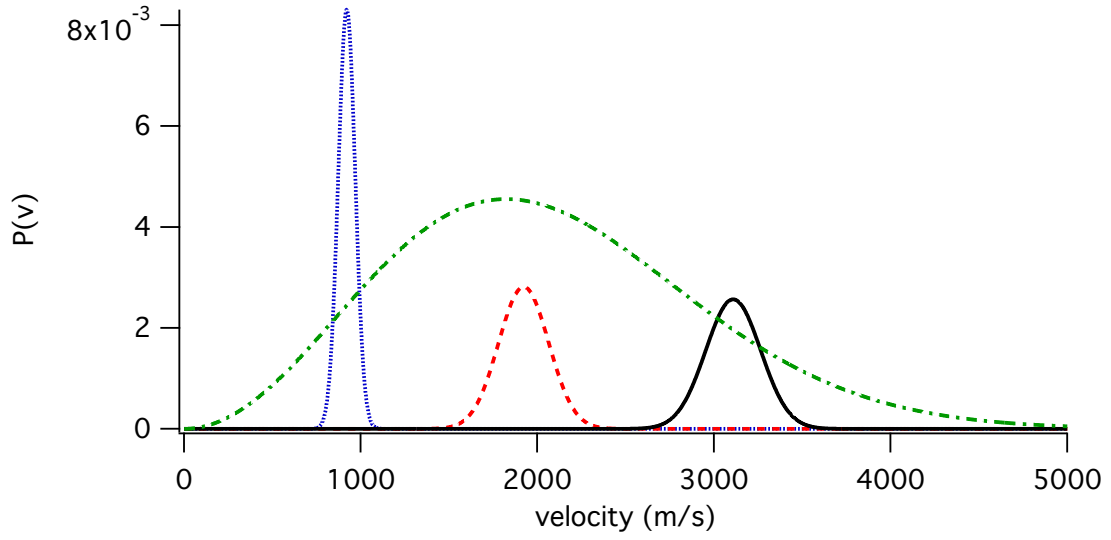
Figure 1.4: Probability distribution of velocities for supersonic beams of Rb (blue dotted), K (red dashed), and Na (black solid), as measured in Figure 2.4. Each distribution is normalized such that $\int_0^\infty P(v)dv = 1$. For comparison, we also show the velocity distribution of a Maxwell-Boltzmann gas of He atoms at 800 K (green dot-dashed) that is used as the carrier gas for the Na supersonic beam, normalized to 10 for visibility.

CHAPTER 2

THIS THESIS IN BRIEF

This chapter explains the essential components of the three experiments that make up the majority of this thesis work: First, a measurement of the static polarizabilities of sodium, potassium, and rubidium (section 2.1). Next, a novel and more precise method to measure the velocity of atom beams (section 2.2) that will improve future polarizability measurements. Then, a measurement of a wavelength of light at which the dynamic polarizability of potassium is zero, known as magic-zero wavelength (section 2.3). This chapter also contains summaries of a proposal to measure the polarizability of strontium using a photoionization detector, and a proposal to measure the tensor polarizabilities of alkali dimers.

2.1 Static polarizability measurements of Na, K, and Rb

In 2008, we set out to establish a new atomic polarizability measurement program in Arizona. In 2010 we published the first improved measurements of potassium and rubidium polarizability in over 35 years [8]. The paper, published in *Physical Review A*, is included in Appendix A. Chapter 3 explains additional details of this experiment. Section 1.1 reviewed the history of polarizability measurements and Figure 2.3 summarizes previous calculations and measurements of alkali polarizabilities.

We measured the polarizabilities of sodium, potassium, and rubidium using a Mach-Zehnder atom interferometer with an interaction region containing an electric-field gradient. The interferometer and electrodes are shown in Figures 2.1 and 2.2. We measured each polarizability (for Na, K, and Rb) independently, and we refer to these as absolute measurements. We also reported ratios of polarizabilities, since we can do this with even higher precision. Table 2.1 shows the absolute measurements (less than 1.0% uncertainty), and Table 2.2 shows the ratio measurements (0.3% precision).

Our measurements of polarizability ratios are new in atom interferometry, and are possible because nanogratings diffract all types of atoms and molecules. Although this unique feature of our interferometer has long been recognized, the work described in this thesis is the first time that the utility of nanogratings for multiple species has actually been used for a precision measurement of polarizability. The benefit of presenting ratios is that systematic errors are nearly the same for different atomic species and cancel when determining polarizability ratios. We combined our ratio measurements with the higher-precision measurement of sodium polarizability by Ekstrom *et al.* [25] to present the most precise measurements of potassium and rubidium polarizability currently available. Our measurements were recently included in an updated table of polarizabilities in the CRC Handbook of Chemistry and Physics [2].

Another unique feature of this work compared to other atom interferometry measurements of polarizability [25, 26] is that we use an electric-field gradient region to
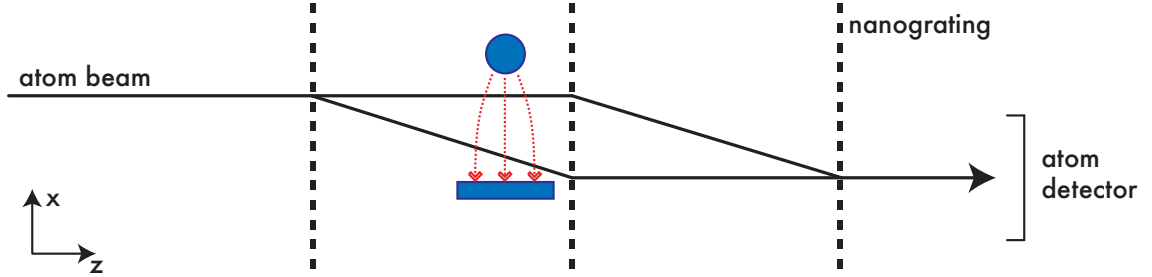
Figure 2.1: Atom interferometer with electric field gradient region (blue electrodes, red field lines) to measure static polarizabilities. An atom passing through the interaction region acquires a phase shift along each path and we measure the differential phase shift.
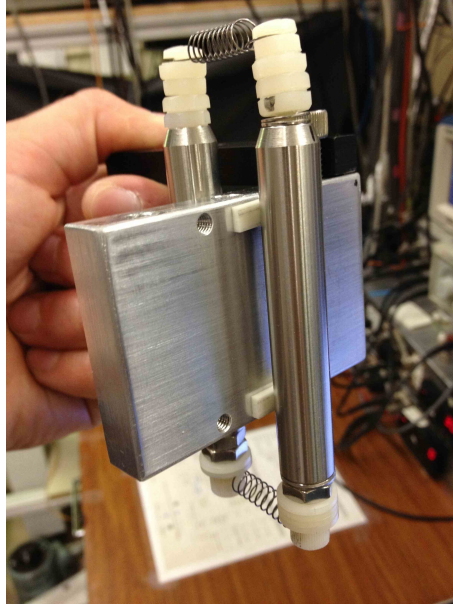
Figure 2.2: Photograph of the polarizability measurement electrodes. The atom interferometer paths pass through electric-field gradient between the rectangular ground plane and the cylindrical electrode.

Table 2.1: Measured absolute and recommended atomic polarizabilities in units of 10^{-24} cm^3. Our recommended polarizability values are based on our ratio measurements (see Table 2.2) combined with the sodium polarizability measurement from Ekstrom *et al.* [25].

	α_{abs}(stat.)(sys.)	α_{rec}(tot.)
Na	24.11(2)(18)	24.11(8)
K	43.06(14)(33)	43.06(21)
Rb	47.24(12)(42)	47.24(21)

Table 2.2: Measured atomic polarizability ratios with statistical uncertainties. Also included are several polarizability ratios from *ab initio* and semi-empirical calculations. See Fig. 2.3 for more calculations and measurements of polarizability ratios.

Atoms	α_{ratio}(stat. unc.) This work	Theory Ref [44]	Ref [45]	Ref [75]
Rb/Na	1.959(5)	1.959(5)	1.946	1.939
K/Na	1.786(6)	1.785(6)	1.779	1.781
Rb/K	1.097(5)	1.098(5)	1.094	1.089
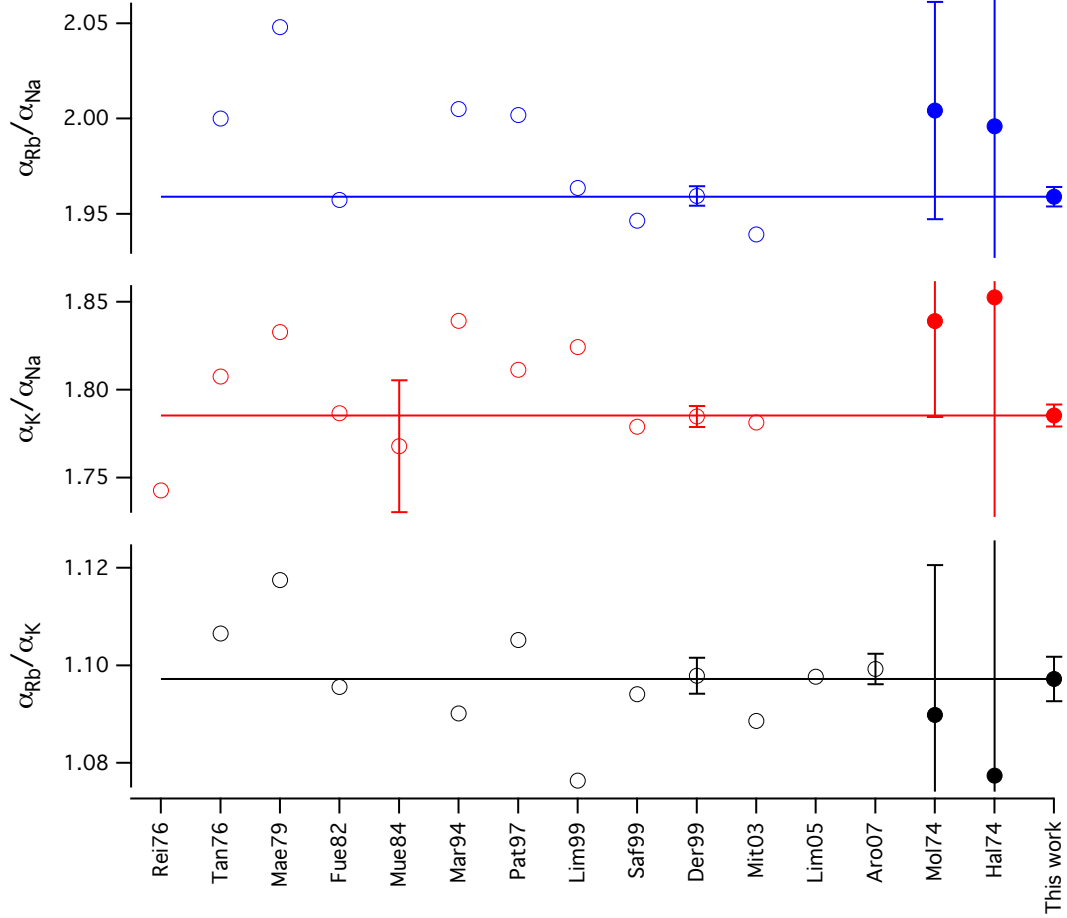
Figure 2.3: Previously calculated (unfilled) and measured (filled) alkali polarizability ratios. References are denoted by the abbreviated first author's name and the publication year. Calculations in references Derevianko *et al.* (1999) [44] and Arora *et al.* (2007) [49] incorporate state lifetime measurements.

apply phase shifts to both paths rather than a septum electrode, which would apply a phase shift to only one path. Electric-field gradient regions have the advantage of not requiring an electrode to be placed between the two atom beam paths. This allows us to study heavier atoms with shorter de Broglie wavelengths and therefore smaller path separations. Since the electric-field gradient interaction region does not require resolved diffraction orders, another advantage is that we can use a less collimated beam to increase the flux and reduce the systematic error caused by velocity-selective detection of atoms in the interferometer. However, electric-field gradient regions have the disadvantage that the measured differential phase shift is proportional to $1/v^2$, rather than $1/v$, so the uncertainty in beam velocity measurements contributes twice as much to uncertainty in polarizability measurements. The phase shift in an electric-field gradient region also depends sensitively on the location of the atom beam paths with respect to the electrodes, unlike in a septum geometry with a uniform electric field.

The primary limitation of the absolute polarizability measurements in this experiment was determining the velocity and velocity distribution of the atom beam. We determined the atom beam velocity by studying atomic diffraction patterns in the far-field of the first nanograting, such as those shown in Figure 2.4. The atom beam velocity is given by rewriting equation 1.5 as

$$v(x_n) = \frac{z_{det}hn}{md_gx_n} \tag{2.1}$$

where z_{det} is the distance from the first nanograting to the detector, and x_n is the position of the nth diffraction order. In reality, a distribution of velocities exists in the supersonic atom beam, and this leads to a distribution of diffraction patterns. The velocity distribution can be well described by a Gaussian with an average velocity v_0 and width σ_v. Figure 1.4 shows examples of typical supersonic atom beam velocity distributions. To better compare velocity distributions with different average velocities, it is useful to define a sharpness ratio $r = v_0/\sigma_v$.

Each observed diffraction pattern is a convolution of the atom beam profile, the
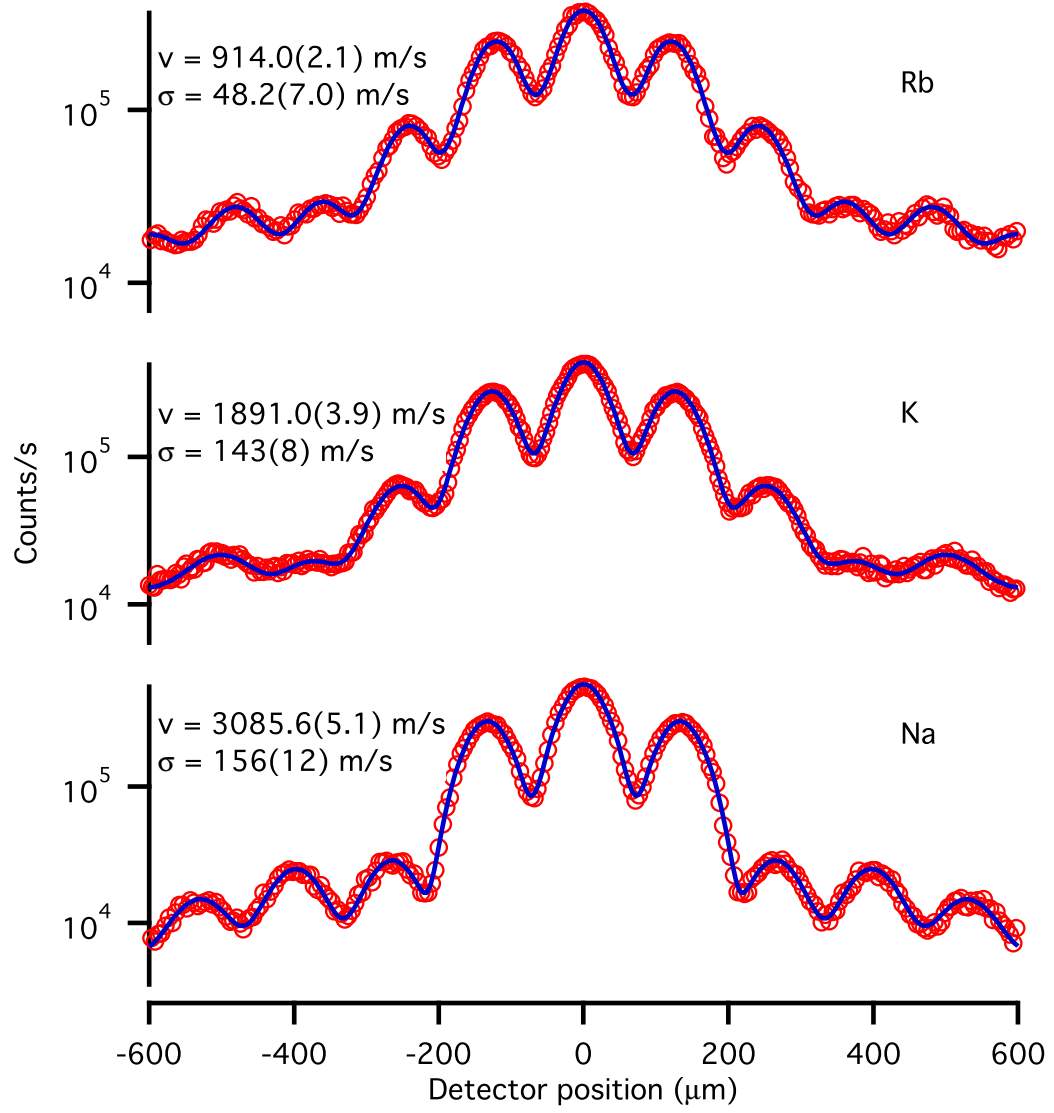
Figure 2.4: Diffraction of Na, K, and Rb atoms determines the average velocity, v_0, and the velocity distribution width, σ_v, of the atom beams. Figure 1.4 shows the velocity distributions determined by these measurements.

detector width, and the atom beam velocity distribution. Figure 2.5 illustrates the individual features that lead to the observed diffraction patterns. Uncertainties in z_{det}, the detector translation angle, and the details of this convolution limited the accuracy of the velocity measurement to 0.3%, and thus contributed 0.6% uncertainty to the absolute polarizability measurements.

If we ignore smaller effects such as the velocity distribution and the atom beam thickness (treated in detail in Appendix A), we can obtain a simple expression for the measured polarizability:

$$\alpha \approx \frac{v^2}{kV^2 x_{\text{int}}} \phi_\alpha. \tag{2.2}$$

Here, k is a constant that depends on the geometry of the interaction region, V is the voltage applied to the interaction region, and x_{int} is the transverse position of the interaction region. Figure 2.6 shows a plot of the phase shift as a function of the interaction region position.

To measure the atom beam position x_{int}, we blocked the atom beam with the high voltage electrode and then moved the electrodes until the atom beam was visible again. Analysis of the transmitted flux vs. electrode position allowed us to determine the atom beam position with a precision of 1 μm. We refer to this as the eclipse method. Unfortunately, we later determined that the motor position report was not as reliable as desired, and contributed a random error to the polarizability measurements. For the electrodes used in this experiment, a 10 μm error in beam position caused a 1% error in the polarizability measurement. We now believe that 5-10 μm position errors were likely for each of the phase measurements, and this led to additional random error in the polarizability measurements. See section 3.4 for more details.

All systematic sources of error, such as uncertainty in z_{det}, the interaction region geometry, or the electrode voltages, are nearly identical for each atomic species. At the level of precision of our experiment, these systematic uncertainties cancel when presenting ratio measurements of polarizabilities. We measured the polarizability of
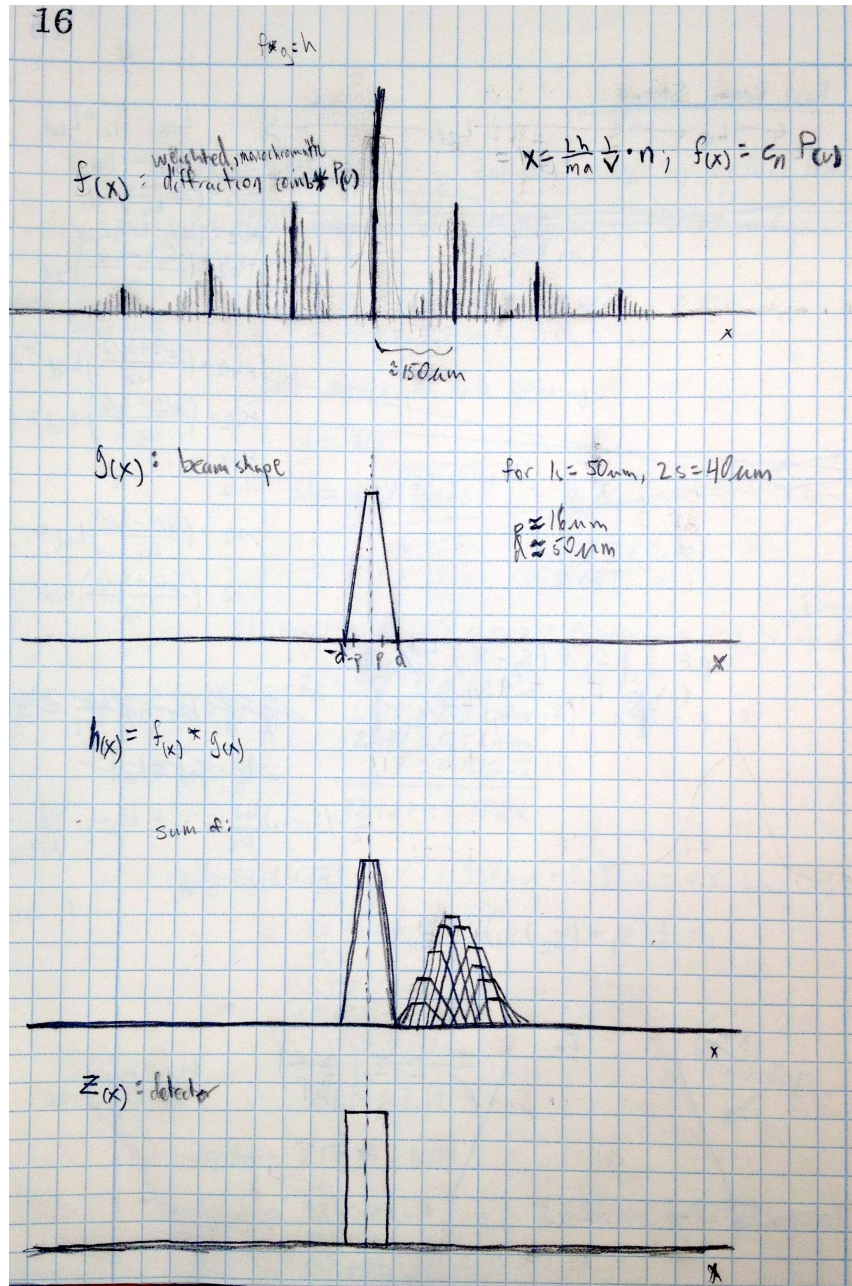
Figure 2.5: From top to bottom the plots show: the diffraction comb for different velocity classes, the trapezoidal atom beam profile obtained using two collimating slits, the convolution of the beam profile with the velocity distribution, and the hot-wire detector size. Figure from Will Holmgren lab notebook number 1 (June 2008).
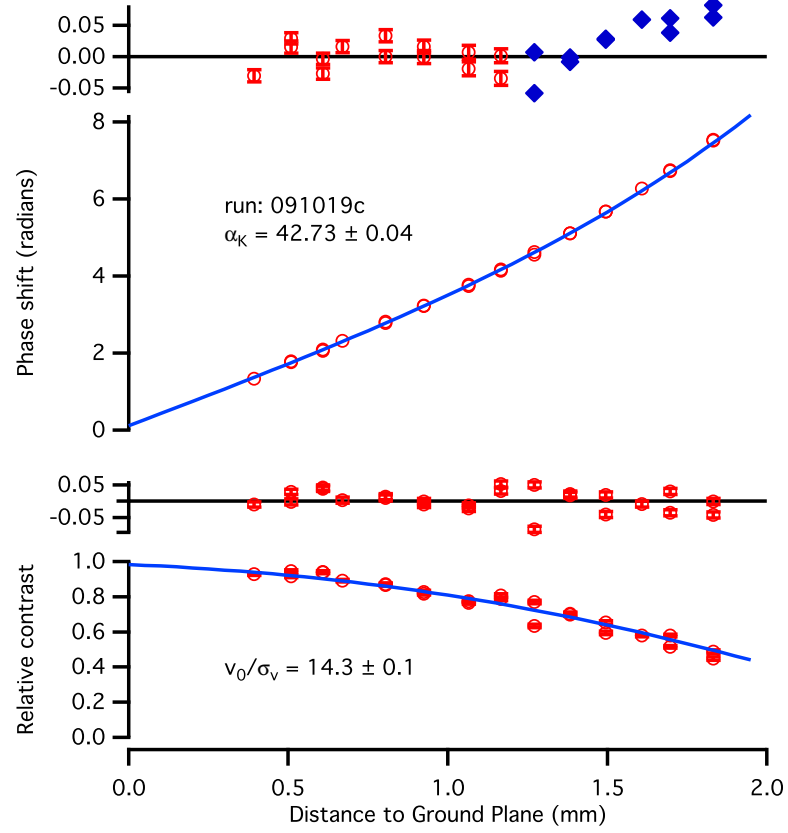
Figure 2.6: Interferometer phase shift and relative contrast vs. interaction region position. We fit the phase shift data to determine the atomic polarizability. Higher phase shift data (blue points) was excluded from the fit due to their higher sensitivity to uncertainties in the velocity distribution width.

each atomic species between 13 and 23 times (see Figure 3.3) and the reproducibility of the measurements determines the statistical uncertainty. The reported statistical uncertainty is the standard error of the mean. The irreproducibility of the data was larger than we expected given the interferometer contrast and count rate, primarily due to the faulty electrode position measurements.

To improve upon our 2010 polarizability measurements, we developed a next-generation static polarizability experiment to reduce most uncertainties associated with this experiment. We developed a new velocity measurement technique (described in the next section), changed the geometry of the electric-field gradient region, improved the electrode position measurement, improved a number of distance measurements, and developed a new data acquisition system. Sections 3.3 and 3.4 and Chapter 4 discuss the improved system in more detail.

2.2   Phase choppers: a new atom beam velocity measurement technique

Atom beam velocity was the largest source of uncertainty in our 2010 polarizability measurements. To reduce this uncertainty we developed a new technique to measure atom beam velocity called *phase choppers* [9]. Phase choppers provide a more precise and more accurate measurement of beam velocity than can be obtained with diffraction. Chapter 4, Appendix B, and C.E. Klauss' B.S. thesis [76] describe this technique in detail. Phase choppers are similar to the phase shifters described in [77] and their utility for measuring beam velocity was first proposed in [65]. Here, we summarize the most important features.

Phase choppers have numerous advantages over atom beam diffraction and other velocity measurement techniques:

1. Higher precision measurements in less time

2. Frequency-based instead of length-based measurement

3. No need for well-separated diffraction orders, so choppers can be used with faster beams (higher flux) and more massive atomic species

4. *in situ* measurement of velocity distribution of atoms contributing to the interference fringes

5. No moving parts

To understand how phase choppers can measure atom beam velocity, it helps to first consider mechanical choppers. Two spinning mechanical choppers (slotted disks) separated by a distance L and blocking the beam at frequency f can transmit atoms with velocity $v = nLf$, where n is an integer. An atom with velocity v will travel a distance L from the first chopper to the second chopper in a time $\tau = L/v$, corresponding to a fundamental chopping frequency $f_0 = v/L$.

Mechanical choppers simply block or transmit atoms, leading to a maximum in the transmitted flux when the chopping frequency is any integer multiple of f_0. In the method we present here, phase choppers are switched on and off by a
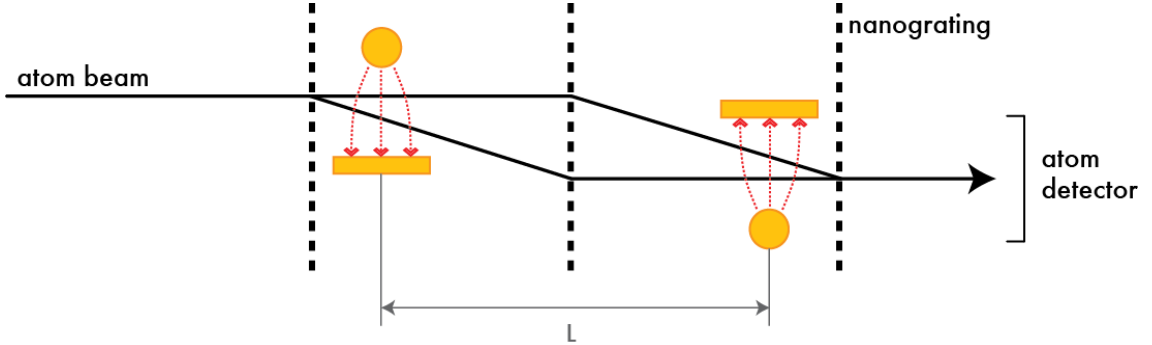
Figure 2.7: Two phase choppers are placed in the interferometer at a distance $L = 1270.68(25)$ mm apart. A square-wave voltage $V(t)$ applied across the choppers creates an electric field (dashed lines). Atoms with velocity v passing through chopper 1 and chopper 2 acquire net differential phase shifts $\phi_1(t) + \phi_2(t + L/v)$.

function generator to periodically apply phase shifts to atomic de Broglie waves in an interferometer. This leads to a maximum in the interferometer *contrast*, instead of the *flux*, when the chopping frequency satisfies $f = nf_0$. The ability to control wavefunction phase, rather than amplitude, provides a more featured and higher flux data set and allows for a more precise determination of velocity.

Figure 2.7 shows two phase choppers added to the atom interferometer. Before continuing, it is worth restating an important principle regarding how our atom interferometer works: the observed fringe pattern is the incoherent sum of the sinusoidal probability distributions from single-atom interference, repeated about 10^5 times per second. Different atoms have different velocities and enter and exit the interferometer at different times. We observe an "average" of all of these fringe patterns. Therefore, if half of the atoms receive phase shifts that are π different from the other half of the atoms, then the measured interference contrast C will be 0. Mathematically, we would observe an intensity $I = I_0 + C_0(0.5\sin(k_x x) + 0.5\sin(k_x x + \pi)) = I_0 + C\sin(k_x x)$ with $C = 0$.

Depending on its start time, velocity, and the chopping frequency, an atom will pass through the two choppers in one of four possible pairs of conditions (off-off, on-off, off-on, or on-on). We now describe what happens to the interference pattern created by atoms with a single velocity v when the choppers are switched at four

Switching frequency f=f_0/4

Position

$-\pi$

$+\pi$

Time

Reference fringe

Resulting fringe (f=f_0/4)

counts

grating pos. (x)

Switching frequency f=f_0/2

z_{c2} z_{c1} L

$-\pi$

$+\pi$

τ

Reference fringe

Resulting fringe (f=f_0/2)

counts

grating pos. (x)

Switching frequency f=f_0

$-\pi$

$+\pi$

Resulting fringe (f=f_0) is the same as the reference fringe

counts

grating pos. (x)
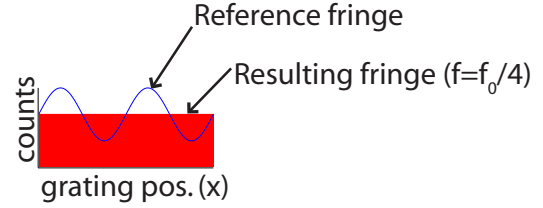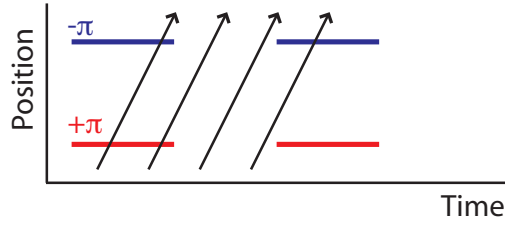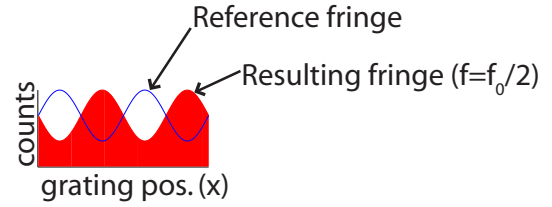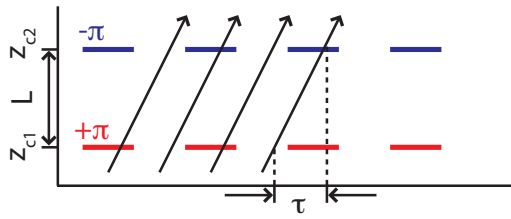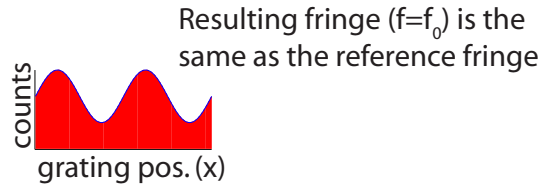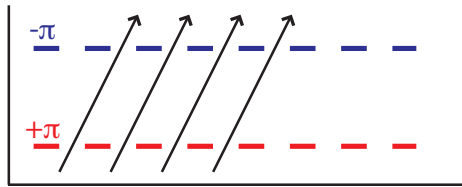
Figure 2.8: Atoms with different starting times will acquire 0, $+\pi$ (red), or $-\pi$ (blue) phase shifts as they pass through chopper 1 and chopper 2, depending on their velocity v and the chopping frequency f. The time it takes an atom with velocity v to travel the distance L between the choppers is τ and $f_0 = 1/\tau$. We measure the average of the sinusoidal probability distributions formed by each atom interfering with itself, shown at right. The reference interference pattern with the choppers off is shown in blue and the resulting interference patterns with the choppers on are shown in red.

particular frequencies (see Figure 2.8):

- $f \ll f_0$. Atoms experience the off-off (0 net differential phase shift) or on-on (0 net differential phase shift) pairs of conditions with equal likelihood, and all atoms emerge with 0 net phase shift. The contrast and phase of the detected ensemble remain unchanged.

- $f = f_0/4$. Atoms experience each of the four possible pairs of conditions, off-off (0), on-off (π), off-on (-π), or on-on (0), with equal likelihood. Therefore, half of the ensemble will acquire 0 net differential phase shift, and half will acquire a π net differential phase shift. The ensemble contrast is 0 and phase is indeterminate. Contrast minima repeat at frequencies $f = (2n + 1)f_0/4$, where n is an integer.

- $f = f_0/2$. Atoms experience on-off (π) or off-on ($-\pi$) pairs of conditions with equal likelihood. The ensemble contrast remains unchanged, but the phase shifts by π (modulo 2π). Contrast revivals with π phase shifts repeat at frequencies $f = (2n + 1)f_0/2$.

- $f = f_0$. Once again, all atoms experience the off-off (0) or on-on (0) states. The ensemble contrast and phase remain unchanged. Contrast revivals with no phase shift repeat at frequencies $f = nf_0$.

These simple cases show how by finding the value of f_0 one can find the velocity of an atom beam through the relation $v = Lf_0$. The contrast revivals and minima that occur at large n provide a way of leveraging small changes in velocity into large changes in revival and minima frequency. In practice, we find the velocity of our atom beam by measuring the contrast at many frequencies and fitting the contrast data to a model discussed in Appendix B. Figure 2.9 shows fitted data from a typical chopper frequency scan using this model. The major corrections to the simple model include methods to account for velocity distribution, velocity dependent phase shifts from the choppers, application of non-π average phase shifts, and velocity-dependent phase shifts due to the Sagnac effect.
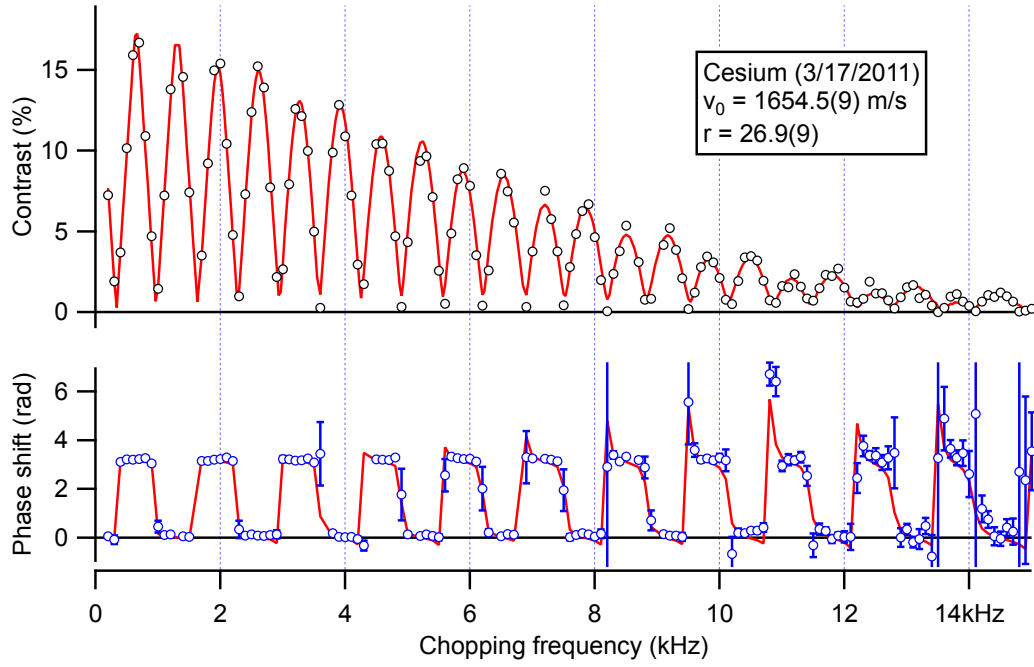
Figure 2.9: Phase chopper data (circles) and corresponding best-fit functions (red curves) for a cesium atom beam with a 70% helium, 30% argon carrier gas. We fit the contrast (black) to find the flow velocity v_0 and velocity ratio $r = v_0/\sigma_v$. The measured phase (blue) is also shown, but is not fit. Each point is derived from 5 seconds of data. Note that the asymmetric slope of the phase data is due to the Coriolis deflection (Sagnac phase shift).

We also tested the phase choppers by measuring the polarizability of cesium using beams with three very different flow velocities on three different days. Each day we alternated between measurements of beam velocity and polarizability every hour to account for small changes in velocity ($< 0.5\%$) over the course of a day due to instability in the beam source temperature. The statistical error of each measurement of velocity was less than 0.1%. We found the cesium polarizability (stat. unc.) to be 59.84(4), 59.71(7) and 59.85(8) Å^3 at flow velocities of 925, 1345 and 1680 m/s. This data is shown in Figure 3.10. These polarizability measurements are subject to a systematic correction due to a revised measurement of the interaction region geometry, but the consistency of the polarizability measurements provides strong evidence that our velocity measurements using phase choppers are reproducible at the 0.1% level, similar to the measurement of Amini and Gould [33].

2.3 Measurement of a magic-zero wavelength

Most measurements of static and dynamic polarizabilities are limited by uncertainty in the electric field strength and uncertainty in the time an atom interacts with the field. To avoid these limitations, we designed an experiment to measure the wavelength at which the dynamic polarizability of an atom goes to zero. This is known as the *magic-zero wavelength*, or *tune-out wavelength*. We published our measurement in *Physical Review Letters* [10] (Appendix C) and Chapter 5 includes supporting material for this experiment.

A magic-zero wavelength (λ_{zero}) occurs between atomic resonances, where the light is red-detuned from one resonance and blue-detuned from another. Opposing contributions from these resonances produce a root in the dynamic polarizability at λ_{zero} and so the energy shift of an atom vanishes at λ_{zero}. Figure 2.10 shows the dynamic polarizability in the vicinity of the four lowest energy transitions of potassium. Three magic-zero wavelengths occur between these four transitions.

Magic-zero wavelengths are understandable in terms of the Lorentz oscillator model of an atom. The equation of motion for an electron in the Lorentz oscillator model yields

$$x(t) = -\frac{e}{m}\frac{1}{\omega_0^2 - \omega^2 - i\omega\gamma}E(t) \qquad (2.3)$$

where e is the electron charge, m is the electron mass, ω_0 is the resonance frequency of the atom, ω is the frequency of oscillation of the electric field $E(t)$, and γ is the damping parameter. We can define a complex polarizability $\alpha(\omega)$ in terms of the dipole moment $p(t)$:

$$p(t) = -ex(t) = \alpha(\omega)E(t) \qquad (2.4)$$

$$\alpha(\omega) = \frac{e^2}{m}\frac{\omega_0^2 - \omega^2 + i\omega\gamma}{(\omega_0^2 - \omega^2)^2 + (\omega\gamma)^2}. \qquad (2.5)$$

The real part of the complex polarizability gives the dispersion and the imaginary part corresponds to absorption of light. Magic-zero wavelengths occur far from
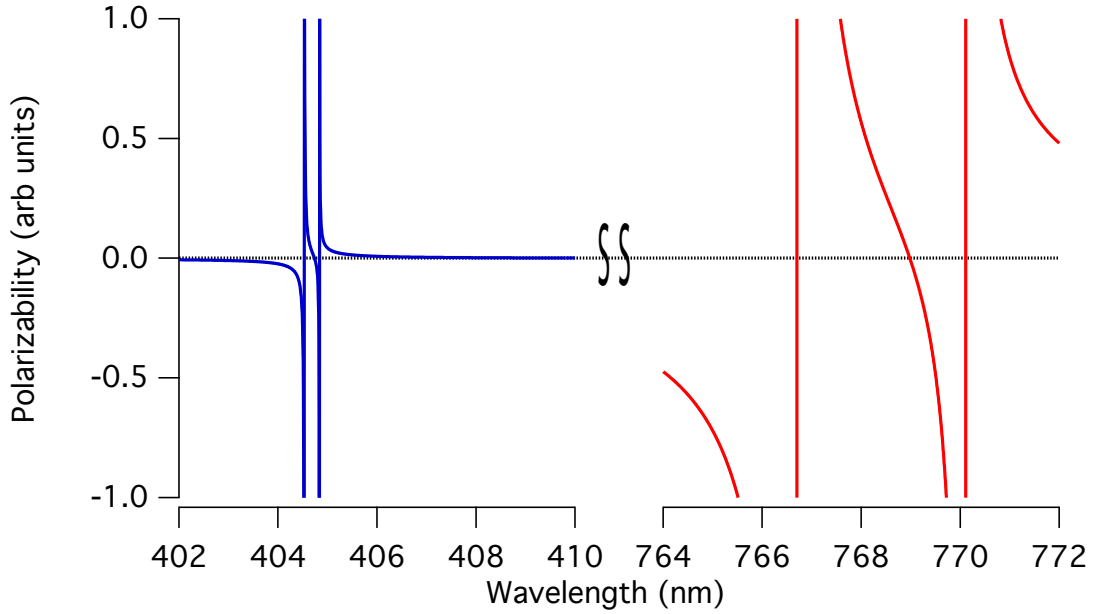
Figure 2.10: A plot of the dynamic polarizability of potassium in the vicinity of the $4s - 4p$ (red) and $4s - 5p$ (blue) transitions. Three zero-crossings, magic-zero wavelengths, are visible near 405 nm, 406 nm, and 769 nm. The blue and red transitions are shown using the same wavelength range to highlight the smaller fine structure splitting of the $4s - 5p$ transitions.

resonance, where the absorption probability is low and $|\omega_0 - \omega| \gg \gamma$, so we drop the imaginary component:

$$\alpha(\omega) = \frac{e^2}{m} \frac{1}{\omega_0^2 - \omega^2}. \tag{2.6}$$

Like any harmonic oscillator, the motion of the electron becomes π radians out of phase with the driving field as the frequency of the driving field passes through resonance, and thus the polarizability changes sign as well. Equation 2.6 clearly shows that the polarizability changes sign as the frequency ω of the driving field passes through resonance.

Chapter 5 and Appendix C describe in detail our measurement of the first magic-zero wavelength of potassium near 769.971 nm [10]. This novel method to probe atom structure yielded the most precise determination of the ratio of the $D1$ to $D2$

line strengths. We found

$$R = \frac{S_2}{S_1} = \frac{|\langle 4s||D||4p_{3/2}\rangle|^2}{|\langle 4s||D||4p_{1/2}\rangle|^2} = 2.0005(40). \tag{2.7}$$

Various λ_{zero} have been used in experiments to study entropy exchange [78], quantum information processing [79], and diffraction of matter waves from an ultracold atom crystal [80]. We have also discussed future applications for magic-zero wavelengths such as measurements of hyperpolarizability, rotation sensing, additional line-strength measurements, and measurements of the contribution of core electrons to polarizabilities.

The longest magic-zero wavelengths for alkali atoms are determined mostly by the transition energies $\hbar\omega_1$ and $\hbar\omega_2$ and the ratio R of the line strengths. We use the sum-over-states approach to describe the dynamic polarizability $\alpha(\omega)$ near these two transitions by

$$\alpha(\omega) = \frac{1}{3\hbar}S_1\left(\frac{\omega_1}{\omega_1^2 - \omega^2} + R\frac{\omega_2}{\omega_2^2 - \omega^2}\right) + A \tag{2.8}$$

where A accounts for contributions from core excitations, higher energy valence transitions, and core-valence coupling [47, 11]. At the longest magic-zero wavelength of potassium, A is 0.02% of the nearly equal and opposite contributions from the principal transitions to the polarizability and A changes λ_{zero} by 0.15(1) pm [81]. Therefore, the theoretical uncertainty in this magic-zero wavelength calculation, 3 pm, is nearly entirely determined by uncertainty in the ratio of the line strengths, R. The total uncertainty of our λ_{zero} measurement was 1.5 pm.

To measure the magic-zero wavelength, we focused 500 mW of laser light asymmetrically on the paths of our interferometer. As stated previously, the energy shift of a polarizable atom is given by

$$U(\omega) = -\frac{1}{2}\alpha(\omega)\vec{E}^2(\omega, z, t) \tag{2.9}$$

where we now allow for a frequency dependence for the polarizability and the electric

field. For optical frequencies, we can only measure the energy shift due to the time average of the electric field, i.e. the intensity. The phase acquired along one interferometer path is given by $\alpha(\omega)$ and the intensity of the light $I(x, z)$ at that location:

$$\phi_0(\omega) = \frac{\alpha(\omega)}{2\epsilon_0 c\hbar v} \int_{-\infty}^{\infty} I(x, z) dz. \tag{2.10}$$

Similar to the static polarizability experiment, where we used a static electric field gradient, here, we use an intensity gradient to apply different phase shifts to each interferometer path. We measure the differential phase shift of the two interferometer paths. Measurements of these differential phase shifts as a function of optical frequency, or wavelength, allow us determine λ_{zero}.

The uncertainty of our λ_{zero} measurement, 1.5 pm, was dominated by the reproducibility of the measurement. The statistical precision (2σ) of our experiment was 1.4 pm. Section 5.2 explains the relationship between the reproducibility and the data collection procedure in more detail. The broadband component of the light, shown in Figure 2.12, was the largest source of systematic error (0.5 pm) in our measurement.

Interferometer contrast loss is primarily due to averaging over large distributions in phase shifts due to the atom beam velocity distribution and the nonuniform differential phase shifts across the atom beam. However, at the magic-zero wavelength we would naively expect zero phase shift for all atoms, and therefore no contrast loss. Unintended elliptical polarization of the laser beam combined with the unpolarized atom beam explains the contrast loss near λ_{zero}. Circular polarization causes different Zeeman substates (m_F) to acquire different phase shifts even at λ_{zero}. Section 5.4 explains the interferometer contrast loss in more detail.

This experiment can in principle be significantly improved before the photon scattering rate places a fundamental limit on the precision of a λ_{zero} measurement. Let us imagine that we had unlimited laser power available and that we could focus all of the light on only one path of the atom interferometer to maximize the
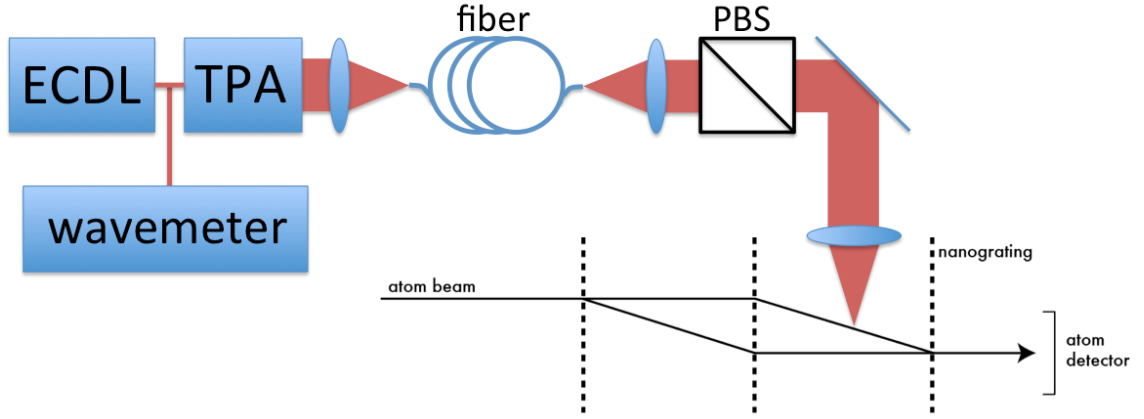
Figure 2.11: Laser system for λ_{zero} measurement. A grating-stabilized laser (ECDL) seeds a tapered amplifier (TPA). Light from the tapered amplifier is coupled into an optical fiber and then focused onto the atom interferometer. A wavelength meter measures the wavelength of the seed laser. Not shown is a shutter after the fiber to switch the light on and off, and an optical isolator on each side of the tapered amplifier.
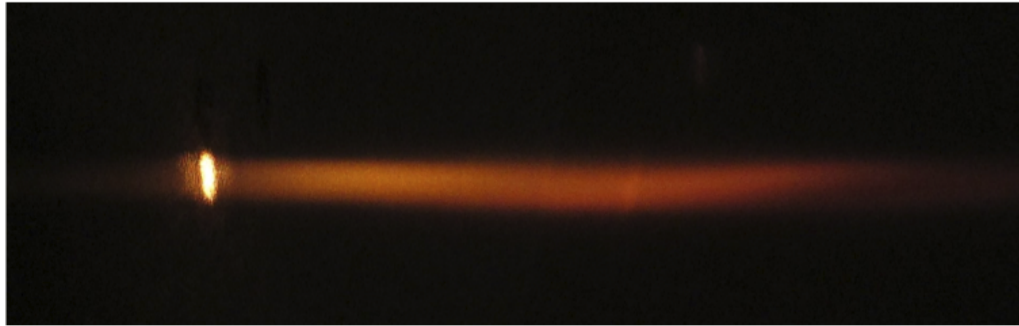
Figure 2.12: Photograph of the laser system spectrum. Light from the tapered amplifier was made to reflect off a diffraction grating and projected onto a screen. The spectrum shown spans approximately 50 nm. It is important to note that the photograph is a convolution of the frequency-dependent transfer function of the imaging system, including an infrared filter, with the spatially separated spectrum. Figure 5.7 shows the laser spectrum measured by a commercial grating spectrometer.

differential phase shift. Both the phase shift and the photon scattering rate grow in proportion to the laser power. However, the interferometer contrast, and thus the phase precision, decreases exponentially with the scattering rate. We therefore calculated a maximum achievable signal of

$$\frac{d\phi}{d\omega} \approx \frac{1}{2\Gamma} P_{\mathrm{s}} \tag{2.11}$$

where P_{s} is the probability that an atom scatters one or more photons and Γ is the excited state decay rate. With contrast loss due to scattering optimized to allow for maximum interferometric precision ($P_{\mathrm{s}} = 1 - e^{-1}$) the slope may become as large as $d\phi/d\lambda = 40$ rad/pm. In this way, future measurements of magic-zero wavelengths can be made with very high precision, possibly with accuracy limited by a shot noise sensitivity better than picometers per $\sqrt{\mathrm{Hz}}$. Section 5.3 contains a more detailed derivation of this limit.

Section 5.6 discusses ideas to improve the precision of λ_{zero} measurements in our lab. Improvements to the measurement precision would allow for benchmark tests of dipole matrix elements between the ns and $(n + 1)p$ levels in potassium and other alkali atoms. These matrix elements are more difficult to calculate due to larger relativistic corrections in the $(n + 1)p$ levels. Interestingly, core electron contributions to polarizabilities may also be determined with λ_{zero} measurements when combined with measurements of static polarizability and/or line strengths, depending on the particular atom and λ_{zero}.

2.4 Strontium polarizability measurement proposal

Polarizability measurements of strontium and ytterbium are currently highly desirable to support next-generation atomic clocks. The blackbody radiation environment surrounding atomic clocks changes the clock frequency by an amount proportional to the differential polarizability of the clock states and accurate polarizability measurements are required to calibrate this frequency shift. As an alkaline-earth atom with two valence electrons, strontium polarizability calculations are also more difficult due to electron correlations and call for experimental benchmarks.

Unfortunately, our atom interferometer is currently unable to measure Sr polarizability due to low detection efficiency. Hot-wire detectors, like the one we use in our atom interferometer, do not ionize strontium atoms as efficiently as the alkali atoms. This is due to the ionization energy of strontium (5.7 eV) being larger than the work function of a platinum wire (5.5 eV). As a result, we presently can only detect collimated beams of strontium atoms in the absence of the nanogratings.

We propose that resonant photoionization can be used to provide high-efficiency and low-noise detection of strontium atoms. The photoionization pathway, shown in Figure 2.13, involves absorption of a 461 nm photon to reach the $^1P_1$ state, and then absorption of a 405 nm photon to place the Sr atom in an autoionizing state. The existence of the autoionizing state increases the photoionization probability of Sr by a factor of about 10^3.

We propose a laser system consisting of a frequency doubled 922 nm laser diode and a free running 405 nm laser diode. A periodically poled KTP crystal can provide sufficient single pass frequency doubling efficiency (1-5%), so we can avoid the complexity of a placing the crystal in a cavity. Generation of 1 mW of 461 nm light with less than 30 MHz linewidth and locked to the $^1P_1$ transition is the most difficult part of this proposed experiment. The 405 nm ionization laser can be relatively simple. The linewidth of the autoionizing transition is nearly 1 nm, so a high power 500 mW, multimode free running diode can be used.

Chapter 6 describes this proposal in more detail and is the topic of current
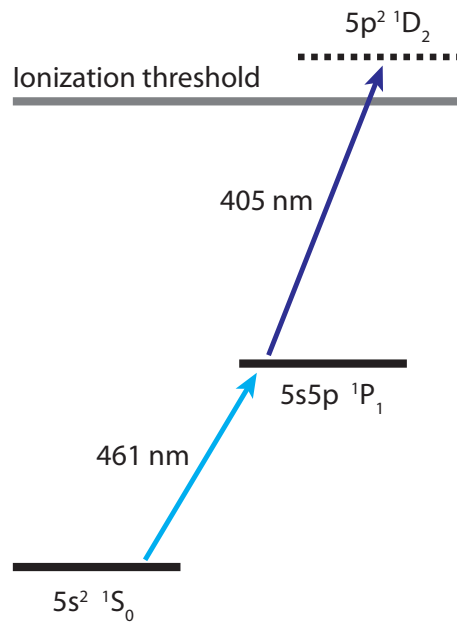
Figure 2.13: Resonance enhanced photoionization pathway of strontium.

research in our lab.
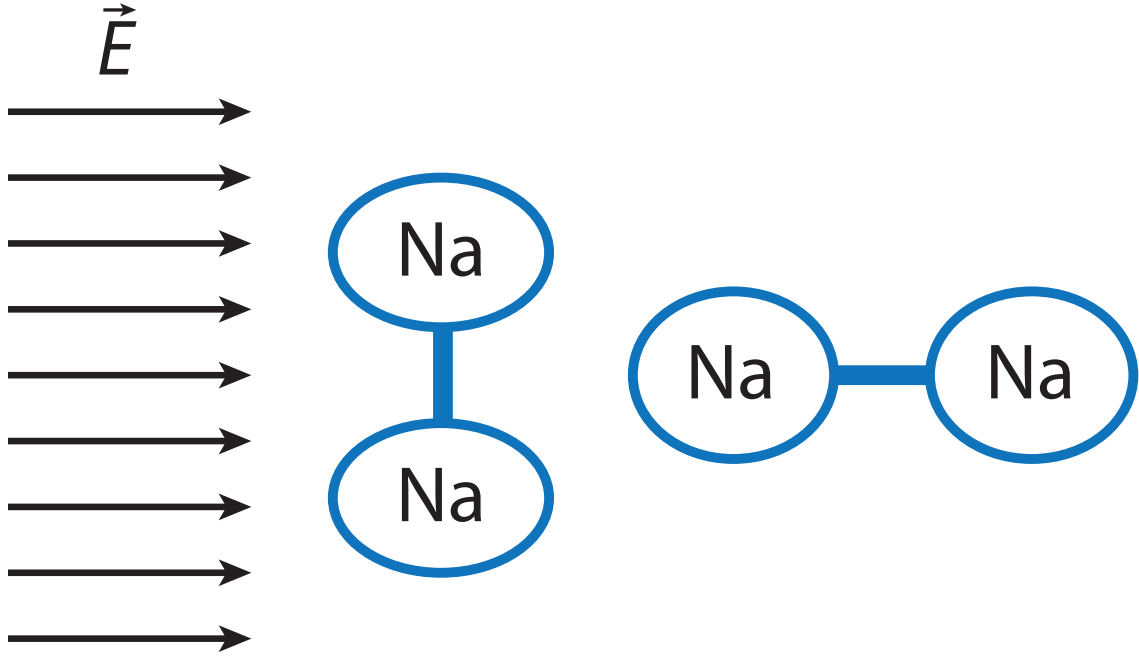
Figure 2.14: Two unique orientations of an alkali dimer with respect to the incident field. These two orientations have different polarizabilities, and thus different phase shifts in our atom interferometer.

2.5 Tensor polarizability measurement proposal

Ground-state alkali atoms are spherically symmetric, and as a result the polarizability may be described by a scalar that does not depend on the direction of the applied field. In contrast, molecules are generally not spherically symmetric and their polarizabilities must be described by a tensor $\overset{\leftrightarrow}{\alpha}$. For a simple molecule such as an alkali dimer, the tensor is diagonal if one chooses to use the obvious axes of symmetry: one along the bonding axis of the molecule and two additional axes that are mutually orthogonal to the bonding axis. Figure 2.14 shows the two unique orientations of an alkali dimer in an electric field. To our knowledge, only the average polarizability of this tensor has been measured [24, 20] for alkali dimers. Chapter 7 describes a proposal to measure the anisotropy of alkali dimer polarizability by studying contrast loss and revivals as a function of electric field strength.

CHAPTER 3

POLARIZABILITY MEASUREMENTS OF NA, K, AND RB

As introduced in Chapter 2, we measured the absolute and relative polarizabilities of sodium, potassium, and rubidium using a Mach-Zehnder atom interferometer with an electric-field gradient. Table 2.1 shows the absolute measurements (which have less than 1.0% uncertainty), and Table 2.2 shows the ratios of polarizability measurements (which we measured with 0.3% precision).

Our paper published in *Physical Review A*, and shown in Appendix A, explains the most important details of the experiment. In this chapter I provide supporting material. I explain how I improved the accuracy of the velocity measurements, I provide a reanalysis of the data set after discarding outliers, and I discuss subsequent improvements that I made to the polarizability measurement interaction region and data acquisition system.

3.1   Improved velocity measurement using a length gauge to study diffraction

Section 2.1 described how the atom beam velocity was measured by studying diffraction data (see Figure 2.4). This technique determines the de Broglie wavelength of atoms in the beam, but it relies on accurate knowledge of the displacement of the hot-wire detector. The DC motors used to move components in our atom beam machine, including the detector translation stage, report their position using rotary encoders and knowledge of the screw pitch as a proxy for linear displacement. However, because of variations in the screw pitch and stick/slip behavior in the translation stage, these position reports are subject to as much as 15 μm errors in linear displacement of the translation stage. Since the diffraction orders are typically spaced by about 130 μm, this corresponds to a $\sim$10% error in velocity. Figure 3.1 shows the displacement reported by a typical motor vs the displacement reported
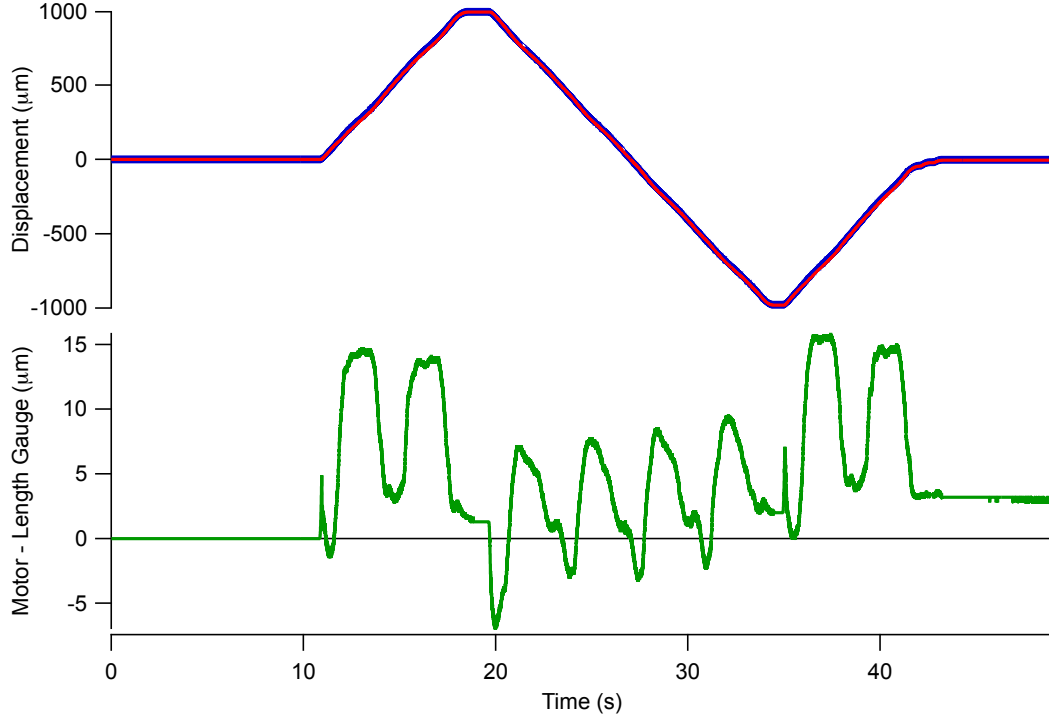
Figure 3.1: Displacement of the interaction region translation stage as measured by the motor encoder (blue) and a length gauge (red), and the difference in displacement measurements (green). Positive (negative) displacements correspond to retraction (extension) of the motor screw. Translating in the negative direction, corresponding to motor extension, is better for our experiments because the position error is lesser.

by a length gauge.

To overcome this problem, I installed a Heidenhain MT-2571 length gauge to measure the detector displacement using a linear encoder. Figure 3.2 shows atom beam velocities and velocity distribution widths determined by fitting diffraction data when using either the length gauge or the motor encoder to measure the detector position. The velocity measurement is clearly more reproducible when using the length gauge to measure detector displacement. I also note that it is possible that detector position measurement errors were significant and neglected in the Ekstrom *et al.* measurement of sodium polarizability [25]. The addition of this length gauge was also crucial for studies of van der Waals potentials using atom beam diffraction in our lab [72, 73].
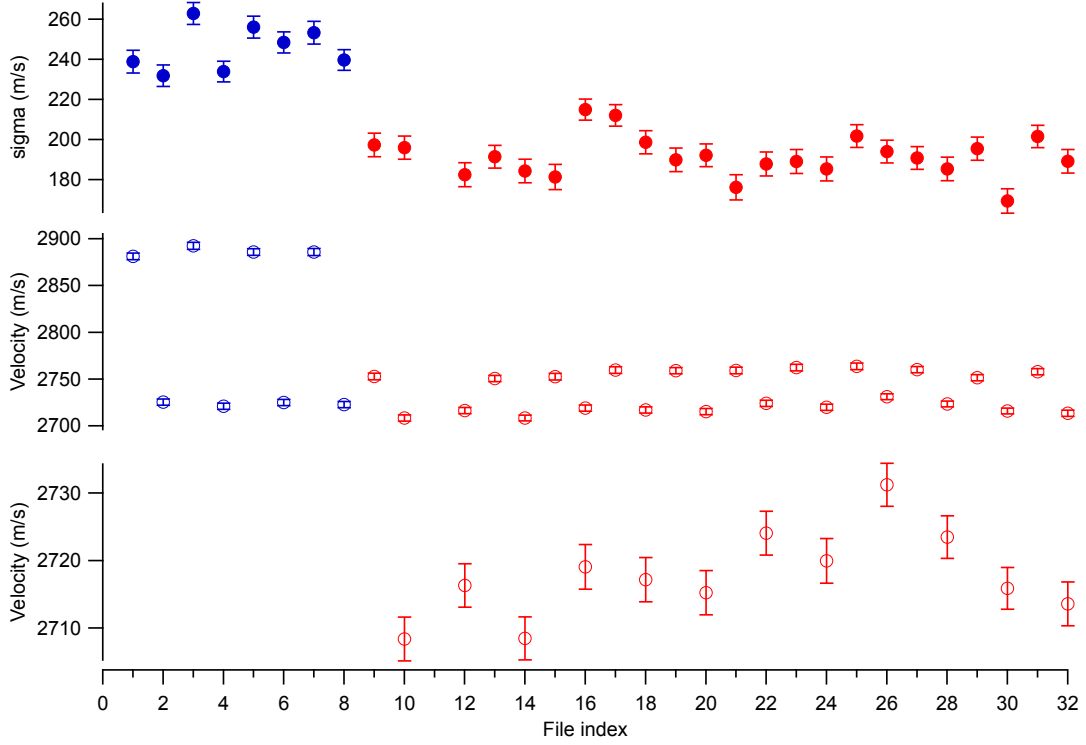
Figure 3.2: Sodium atom beam velocity (open circles) and velocity distribution width (filled circles) using the detector motor (blue, files 1-8) or length gauge (red, files 9-32) to measure detector displacement. The up-down pattern in velocity reflects the fact that the motor direction was alternated and the translation stage exhibits stick/slip behavior. We only use the measurements corresponding to the extension of the motor screw (even numbered file indices), since this minimizes errors due to stick/slip of the translation stage. This subset of measurements yield $v = 2717.8(6.5)$ m/s and $\sigma_v = 190(11)$ m/s, where the uncertainties are the standard deviation and are statistical only.

Table 3.1: Measured absolute atomic polarizabilities using all data points and the central 80%. Also shown are the polarizabilities of K and Rb obtained using our ratios of polarizabilities using the central 80% of the data (see Table 3.2) combined with the sodium polarizability measurement from Ekstrom *et al.* [25].

	$\alpha_{\text{abs All}}(\text{stat.})(\text{sys.})$	$\alpha_{\text{abs Trim}}(\text{stat.})(\text{sys.})$	$\alpha_{\text{Trim ratio \& Eks}}(\text{tot.})$
Na	24.11(2)(18)	24.12(1)(18)	
K	43.06(14)(33)	43.08(11)(33)	43.06(19)
Rb	47.24(12)(42)	47.21(10)(42)	47.20(20)

Table 3.2: Measured atomic polarizability ratios with statistical uncertainties for the entire data set and the trimmed data set.

	$\alpha_{\text{ratio}}(\text{stat. unc.})$	
Atoms	All data	Trimmed
Rb/Na	1.959(5)	1.958(4)
K/Na	1.786(6)	1.786(5)
Rb/K	1.097(5)	1.096(4)

3.2 Reanalysis using a trimmed mean

I reanalyzed the 2010 polarizability data using a trimmed mean, so that the lowest and the highest 10% of the data were discarded before calculating the mean and the standard error of the mean. This procedure is useful when outliers occur more frequently than a normal distribution of measurements would predict. Figure 3.3, Table 3.1 and Table 3.2 show the results of this analysis. The statistical uncertainty of each polarizability measurement improves by about 20%. As a result, the uncertainty of our measurements of α_{K} and α_{Rb} (determined by our ratio measurements of polarizabilities combined with the Ekstrom *et al.* measurement of α_{Na}) improve slightly as well. These changes are well within the statistical uncertainty of the original measurements.
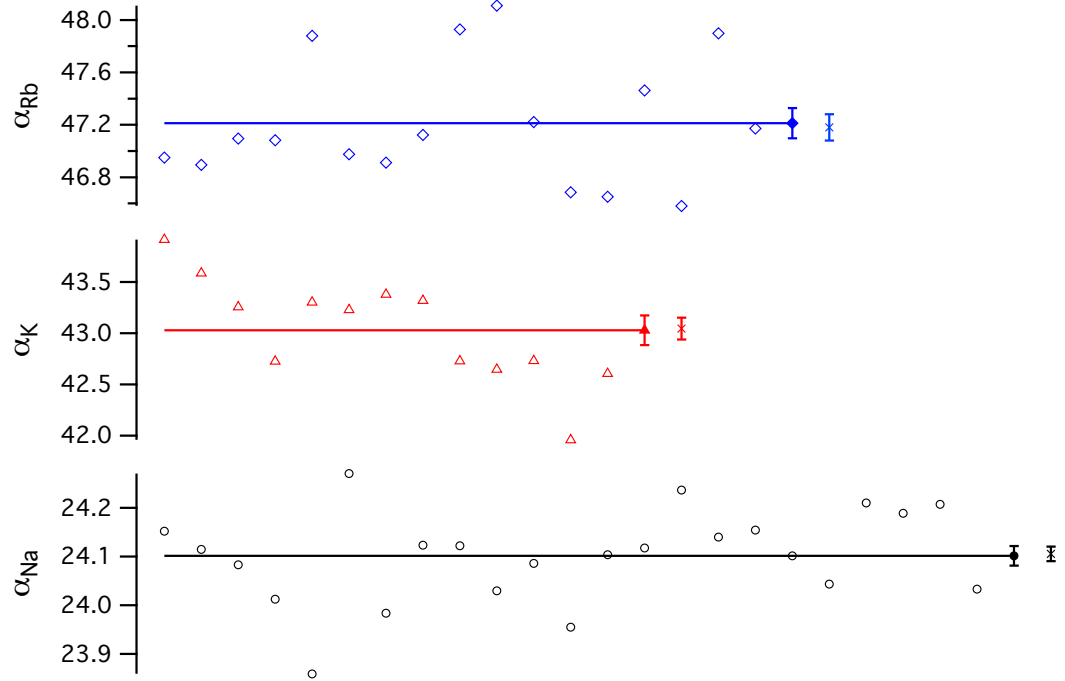
Figure 3.3: Multiple measurements of the polarizability of sodium (circles), potassium (triangles), and rubidium (diamonds). The mean polarizabilities are denoted by filled markers and lines. The trimmed means are denoted by crosses. The error bars represent the standard error of the mean. Units are 10^{-24} cm^3. Final results are shown in Table 3.1.

3.3 Data acquisition system upgrades

The 2010 polarizability measurements were accomplished by manually moving the interaction region and switching the high-voltage electrode on and off about once per minute. This quickly became mind-numbing, tedious work. Higher precision measurements of polarizability clearly demanded a more automated data acquisition system.

We developed a new data acquisition system in LabView 2010 with the ability to move and accurately record the distance traveled by any motor (via on-board quadrature decoding) in the atom beam machine and automatically control multiple high-voltage power supplies and a function generator. Figure 3.4 shows a screen shot of the data acquisition system. The new data-acquisition system uses a producer-consumer architecture to simultaneously record and analyze atom fringe data. This *in situ* processing of atom fringe data has proven to be immensely valuable. Hardware controlled timing signals ensure that measurements of the atom beam count rate and the grating position are commensurate. A second screen enables viewing of the interferometer data from the optical table in our lab.

3.4 Next-generation polarizability measurements

After publishing our 2010 polarizability measurements we designed a new experiment to improve both the precision and accuracy of polarizability measurements in our lab. We chose to replace the ground plane from the previous interaction region with a 2nd pillar. Figure 3.5 shows a schematic of the atom interferometer and a two-pillar interaction region. Figures 3.6 and 3.7 show a photo and a schematic of the new interaction region, respectively. The pillars are made of two 0.5 inch diameter rods separated by 3.81 mm. Figure 3.8 shows a measurement of cesium polarizability using the new interaction region.

As discussed in section 2.1, the electric fields of the two regions are nominally identical, however, there are several advantages to the two-pillar geometry. First, two pillars allows us to measure phase shifts on both sides of the plane of symmetry
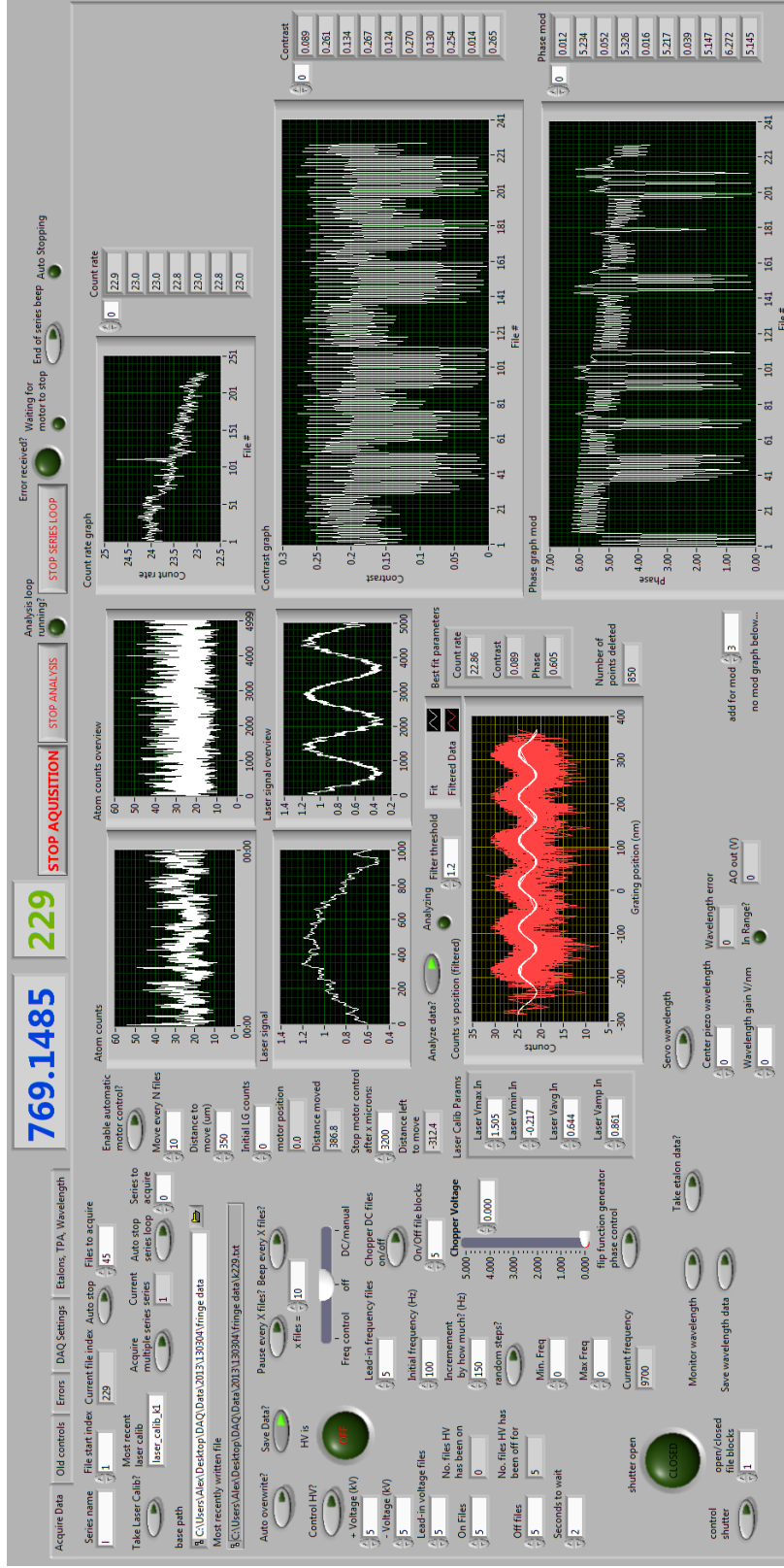
Figure 3.4: Screenshot of the data acquisition system. The left side contains experiment controls, such as data series name, the type of measurement (polarizability, velocity, or magic-zero wavelength), and high voltage settings. The middle section shows the atom count rate and laser interferometer data as a function of time and a plot of the interference fringe determined from the previous 5 s worth of data. Finally, the right side shows a history of the average count rate, contrast, and interferometer phase for the current data series. Additional tabs contain channel controls, error reporting displays, and some additional laser system monitors. While perhaps overwhelming at a glance, this suite of controls and instruments provides a significantly more powerful grasp of the experiment than the previous data acquisition system.
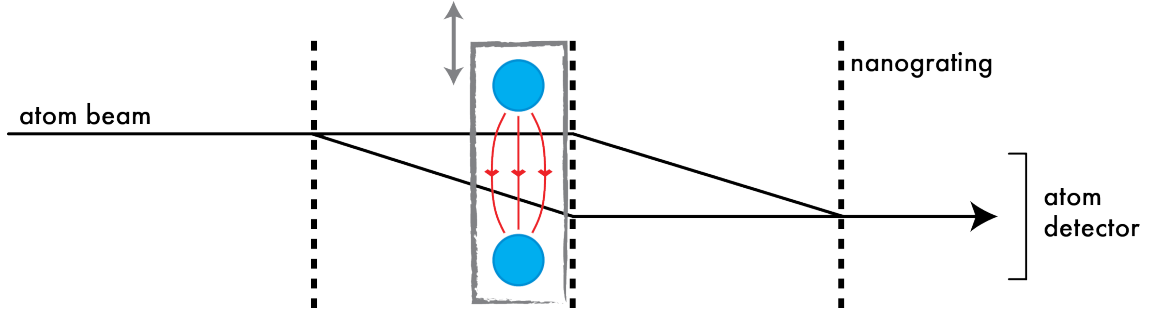
Figure 3.5: Atom interferometer with two-pillar interaction region. Measuring differential phase shifts as function of interaction region position, such as those shown in Figure 3.8, allows us to determine the polarizability of an atom.

in the electric field calculation. This in turn enables us to use phase shift data to independently determine both the polarizability and the position of the pillars relative to the atom beam. Measuring phase shifts on both sides of the symmetry plane also allows us to better control for the Sagnac phase shift. This is because the Sagnac phase shift makes the total phase shift closer to zero on one side of the pillars and farther from zero on the other, leading to an unambiguous signature. See Appendix A for a description of how the Sagnac phase shift effects the atom interferometer contrast and phase.

We also added a Heidenhain MT-2571 length gauge to measure the interaction region position. Irreproducibility in the interaction region position may have been a large source of the statistical error of the polarizability measurements in the first generation experiment. Section 3.1 discussed the advantages of using a length gauge to measure displacement instead of relying on built-in rotary motor encoders.

Figure 3.9 shows a single day of cesium polarizability measurements using the new electrodes, phase choppers for measuring atom beam velocity, and the new data acquisition system. Note the approximately 6 times improvement in statistical precision compared to our 2010 work, shown in Figure 3.3. Figure 3.10 shows consistent cesium polarizability measurements at three different atom beam velocities.
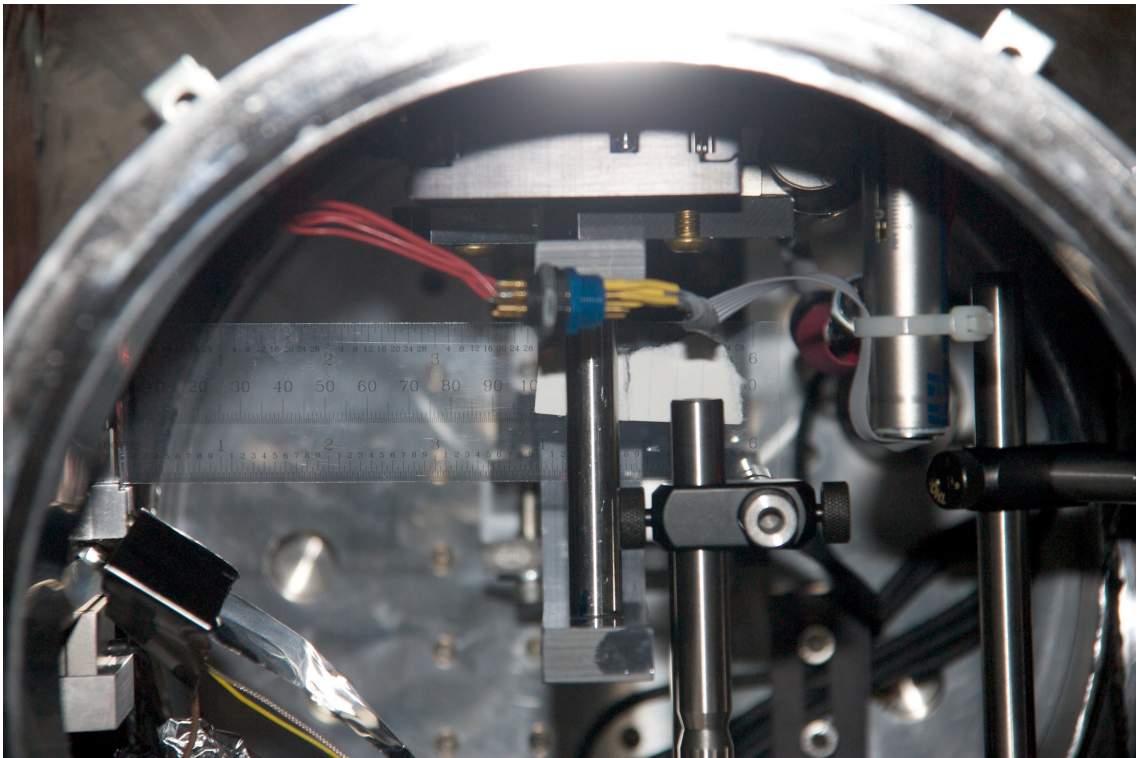
Figure 3.6: Measurement of the distance between the two-pillar interaction region and the 2nd nanograting (left side, nearly edge-on).
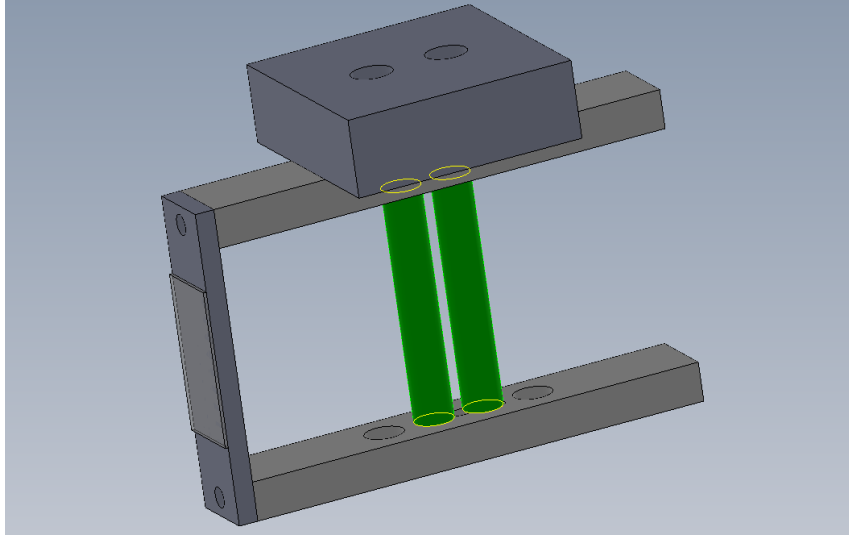
Figure 3.7: Perspective rendering of the new interaction region. The electrodes (green) are held by PVC mounting bracket (light grey) and attached from below to a translation stage (dark grey). A microscope slide (semi-transparent) contacts a length gauge (not shown) for precise displacement measurements.
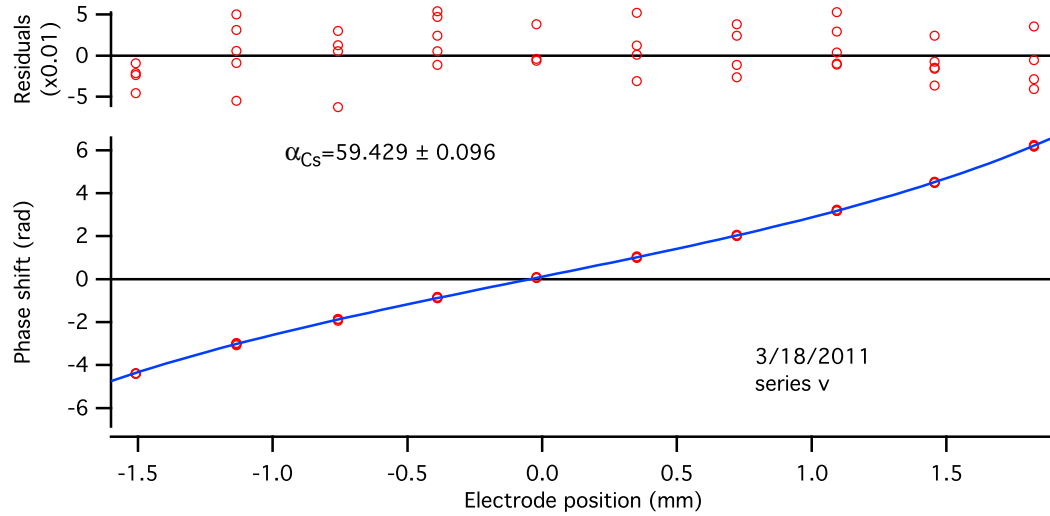
Figure 3.8: Measurement of cesium polarizability using a two-pillar interaction region. A least-squares fit to the phase shift data determines both the atomic polarizability and the atom beam position simultaneously. The reported uncertainty is statistical only.
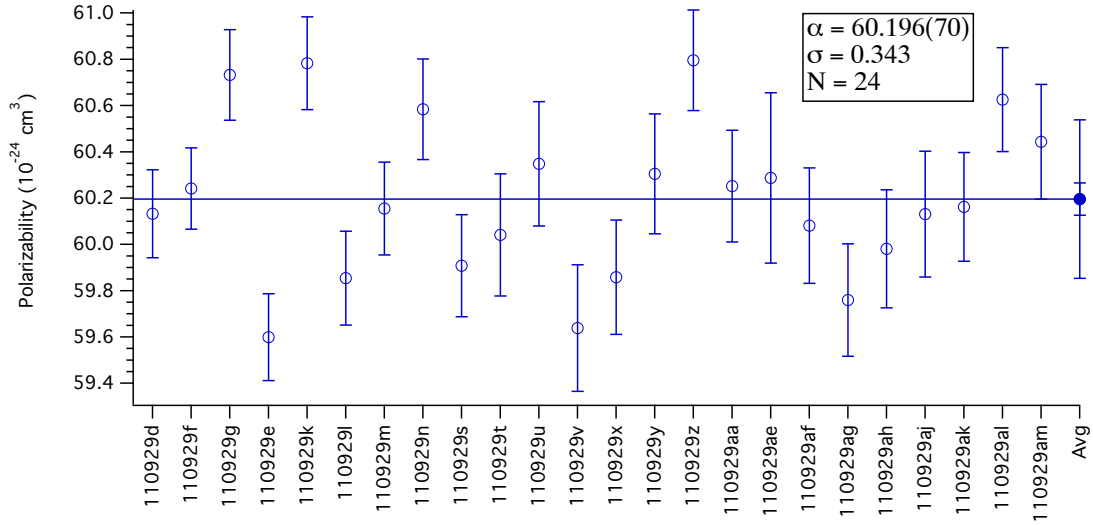
Figure 3.9: One day of polarizability measurements of cesium. The statistical precision (standard error of the mean) is 0.12% (standard deviation of 0.5%). However, the accuracy of this measurement is 1% due to several uncalibrated parameters, such as the distance between the electrodes. The statistical uncertainty of each measurement is not used in determining the polarizability or the uncertainty, but is shown as a measure of consistency.
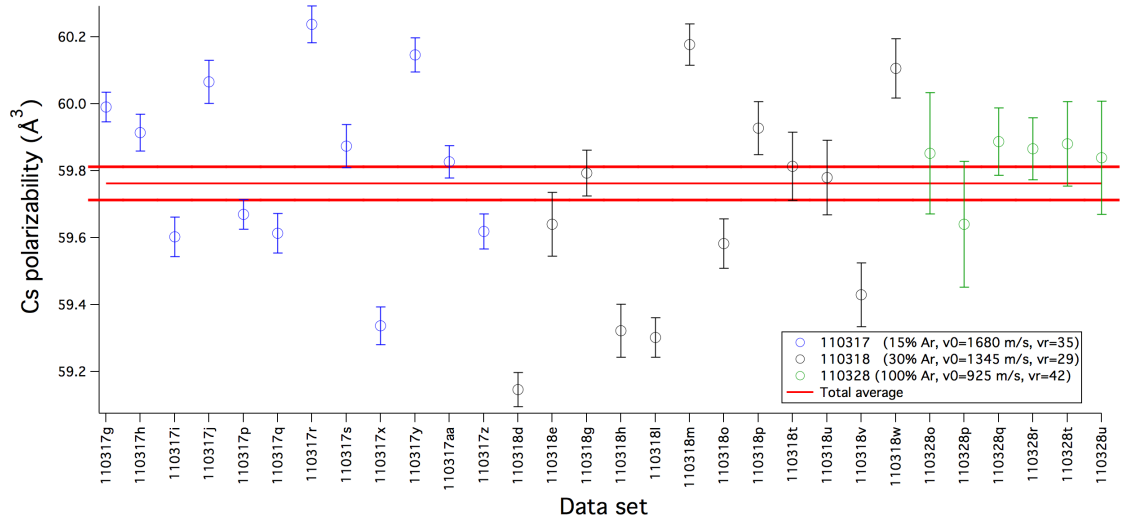
Figure 3.10: Consistent cesium polarizability measurements at three different velocities: 1680 m/s (blue), 1345 m/s (black), and 925 m/s (green). The total average and standard error of the mean is shown in red.

CHAPTER 4

MEASUREMENTS OF ATOM VELOCITY USING PHASE CHOPPERS

Section 2.2, Appendix B and C.E. Klauss' B.S. thesis [76] discuss our use of phase choppers to measure atom beam velocity. Section 3.4 shows polarizability measurements obtained after measuring atom beam velocity using phase choppers. Here, we provide samples of the pictures used to determine the distance between the phase choppers. I also discuss the ability of phase choppers to act as lenses for atomic de Broglie waves.

4.1   Distance measurements using high resolution pictures

The accuracy of the velocity measurement using phase choppers can only be as good as the measurement of the distance between the two choppers. To measure this distance (and others in the machine) we carefully inserted a series of rulers and tape measures into the vacuum chamber and took high resolution pictures of the choppers next to the measuring devices, such as the ones shown in Figure 4.1 and Figure 4.2. We mounted the camera (a Canon PowerShot S90) on a translation stage to accurately center the high-voltage wire in the middle of the frame and avoid angular misalignments. This minimized errors due to distortion and parallax. We then used optical and digital zoom to determine the positions of the choppers with respect to the tape measures with 100 μm precision. We used additional rulers and calipers to calibrate the accuracy of the tape measure.

We also took additional pictures with a vertically oriented ruler to determine the height at which the atom beam crosses the phase choppers, as well the angle of the choppers with respect to vertical by placing a plumb line next to the choppers. An example of the plumb line is shown in Figure 4.1. These two measurements are combined to measure the distance between the two choppers where it counts: at the
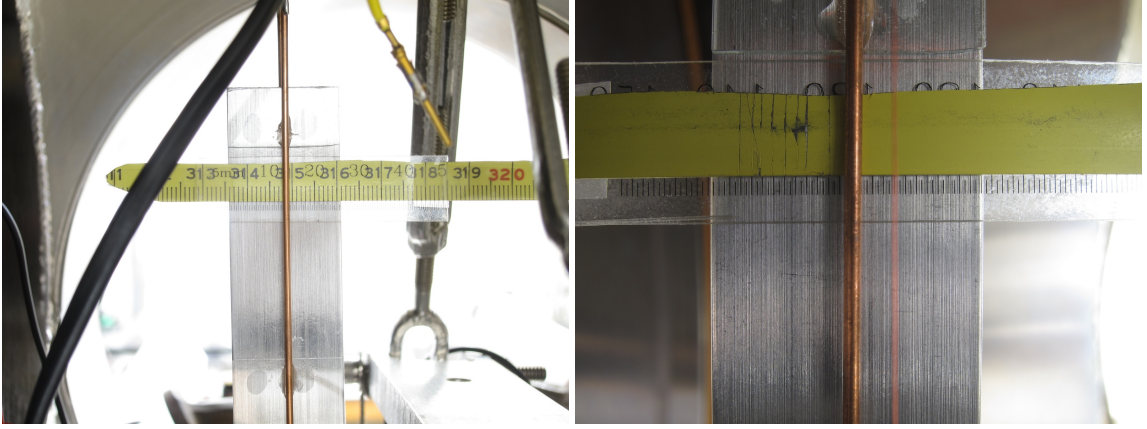
Figure 4.1: Measurement of the distance between chopper 1 and chopper 2 using a tape measure strung through the vacuum chamber above the atom beam path. Chopper 1 east side (left), and chopper 2 west side (right) are pictured. A transparent ruler serves as a translator between the two sides of the tape measure. The total uncertainty of this distance measurement is 250 μm. A plumb line (red) next to chopper 2 is also shown. Figure 4.2 shows the approximate midpoint of the ruler above the 2nd nanograting.

height of the atom beam.

4.2 An electrostatic lens for matter waves inside an atom interferometer

In trying to reconcile small but persistent differences between the expected and observed interferometer contrast when using phase choppers, we discovered that our phase choppers can act as a lens for matter waves in our atom interferometer. Phase choppers, like all of the interaction regions described in this thesis, apply phase shifts that are a function of atom beam velocity. We would therefore naively assume that this dispersive phase shift would lead to a decrease in the measured contrast due to the velocity distribution of the atom beam. Instead, we observed that chopper 2 could *increase* the interferometer contrast. Figure 4.3 shows an example of the interferometer contrast increasing when chopper 2 applies a differential phase shift.

The key to understanding this effect is to realize that we detect the fringes formed by two complementary interferometers (formed by the +1, 0, and -1 diffrac-
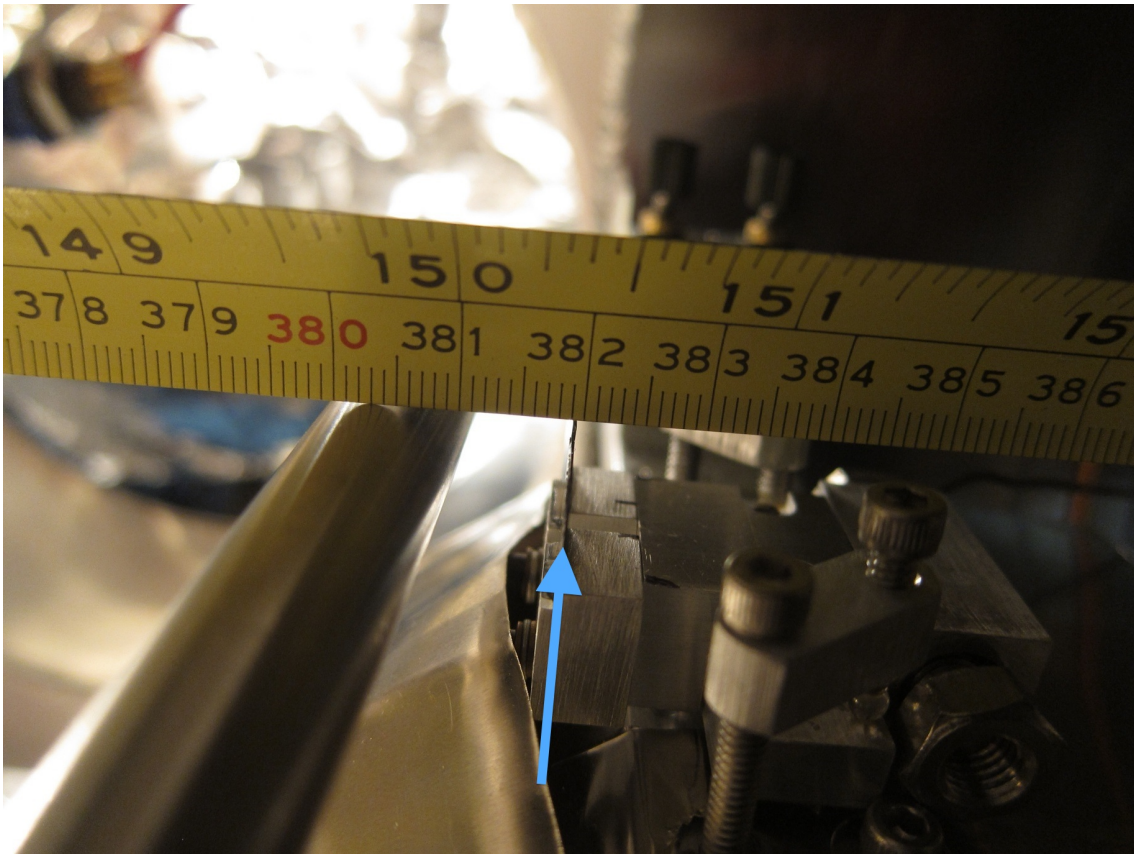
Figure 4.2: Measurement of the distance between chopper 1 and chopper 2. Two different nanogratings (both suitable for use as the second nanograting in the interferometer) are viewed edge-on and highlighted with a blue arrow. This allows us to determine the position of the 2nd grating with respect to the two phase choppers.

tion orders from the first nanograting) and that the fringes formed by the two interferometers will not have the same phase unless the distance between the first and second nanogratings is exactly equal to the distance between the second and third nanograting. That is, if $d_{1G2G} \neq d_{2G3G}$ there will be a phase mismatch between the two interferometers, and thus a loss of contrast. Figure 4.4 shows a two interferometer model with chopper 1, the polarizability pillars, and chopper 2. Any of these electrodes can in principle correct for a phase mismatch between the two interferometers, provided that the sign of the phase shift is correct and the contrast loss due to the velocity distribution is negligible. However, chopper 2 can more easily correct the phase mismatch because of the larger spatial separation between the two interferometers at its location. This process is analogous to a diverging lens for matter waves in the atom interferometer acting to magnify the atom interference fringes. The consequences of this mechanism will be detailed in a future publication from our group.

Our *New Journal of Physics* paper [9], included in Appendix B, acknowledges that we could not explain the small difference between the measured reference contrast and the best-fit contrast determined using χ^2 minimization. This problem was largely irrelevant to the determination of the atom beam velocity because it does not directly effect the frequencies at which the contrast revivals and minima occur. The contrast discrepancies do, however, effect the determination of the width of the velocity distribution. This in turn slightly changes the best estimate of the average velocity. In Holmgren *et al.* [9], we estimated a 0.04% systematic error in velocity may be present due to this discrepancy. We now understand that the magnitude of the error depends on the distance mismatch between the three nanogratings and may be several times larger unless we take more care to align the interferometer. Clearly, the highest accuracy measurements of atom beam velocity demand a full understanding of the data, and we are developing a more sophisticated model to incorporate these lensing effects.
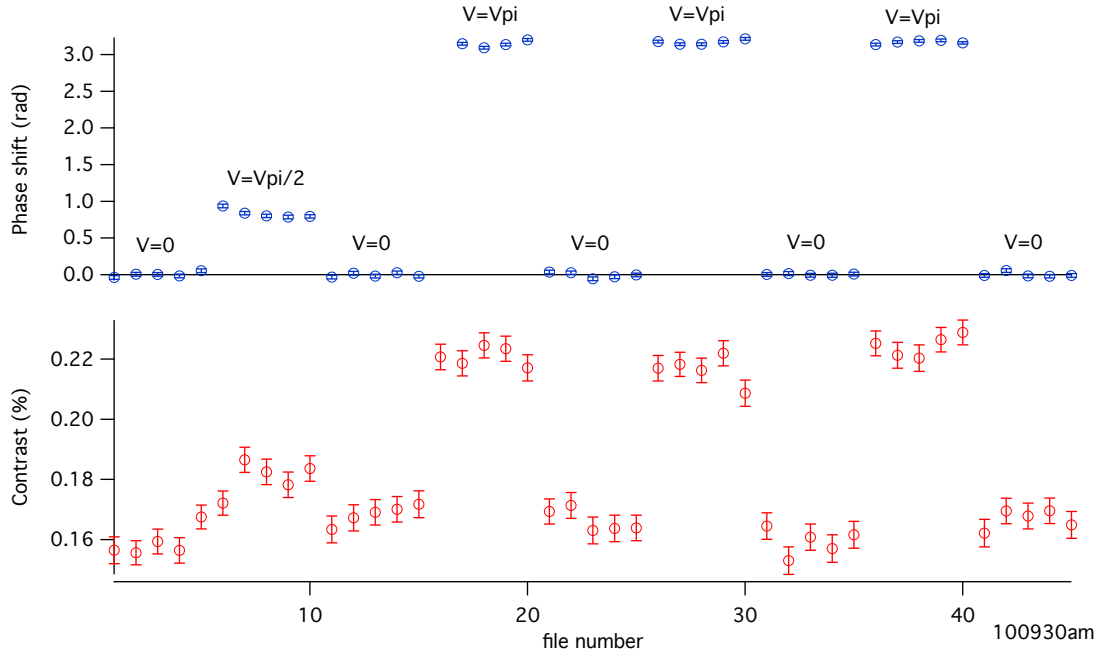
Figure 4.3: Interferometer phase shift (blue) and contrast (red) for three different voltages applied to chopper 2. V_π is the voltage necessary to create a π phase shift. The interferometer contrast *increases* when a voltage is applied due to the *rephasing*, or alternatively, the *lensing* ability of chopper 2.
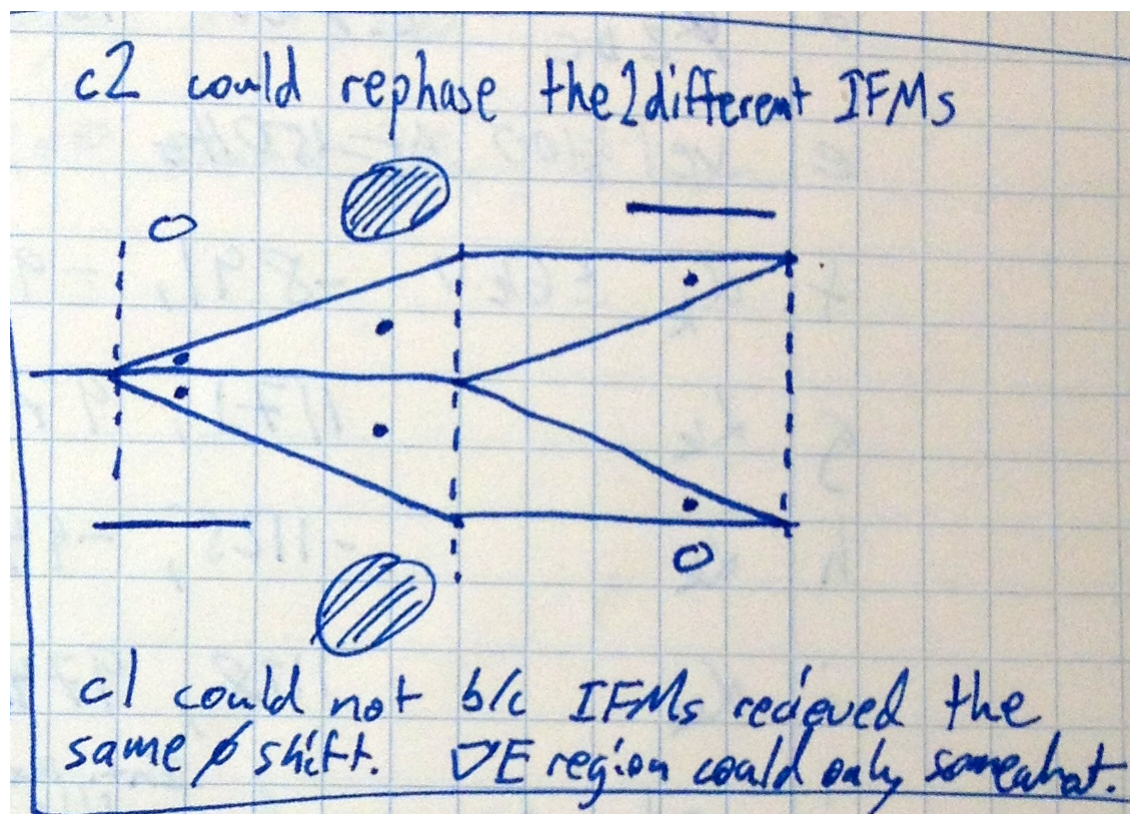
Figure 4.4: Nanogratings form multiple interferometers whose centerlines (marked with dots) diverge as a function of distance from the first nanograting. These two interferometers acquire different phase shifts because the electric field gradient is not uniform. The mismatch between interferometer phase shifts normally leads to a loss of observed contrast, but it can also lead to an increase in observed contrast if the distance between the first and second nanogratings is not equal to the distance between the second and third nanogratings. The phase choppers c1 and c2 are represented by small circles and thin lines (see Figure 2.7) and the polarizability interaction region is represented by slashed circles (see Figure 3.5). Figure from page 31 of Tucson Book 13, October 5, 2011.

CHAPTER 5

MEASUREMENT OF A MAGIC-ZERO WAVELENGTH

Section 2.3 and Appendix C describe our measurement of the first λ_{zero} of potassium, published in *Physical Review Letters* (2012) [10]. In this chapter I will discuss the relationship between dynamic polarizability, oscillator strengths, and line strengths. I will then discuss our data analysis procedures, derive the fundamental limit to the precision of any λ_{zero} measurement, discuss contrast loss mechanisms, and discuss the effect of an impure optical spectrum on λ_{zero} measurements. Finally, I will discuss several possible new experiments to improve the precision of λ_{zero} measurements.

5.1 Polarizability, oscillator strengths, matrix elements, and all that

The dynamic polarizability $\alpha(\omega)$ can be written most compactly in atomic units as

$$\alpha(\omega) = \sum_k \frac{f_k}{\omega_k^2 - \omega^2} \tag{5.1}$$

where f_k is the oscillator strength. Note that the conversion between frequency in atomic and S.I. units is

$$\begin{aligned} \omega_{\text{a.u.}} &= \frac{\hbar}{E_h}\omega_{\text{SI}} \\ &\approx \frac{\omega_{\text{SI}}}{4.1341 \times 10^{16} \text{ Hz}}. \end{aligned} \tag{5.2}$$

The sum of f_k is approximately equal to the number of valence electrons, i.e. 1 for alkali atoms and 2 for alkaline-earth atoms. f_k is related to the reduced dipole matrix elements through

$$f_k = \frac{2|\langle\psi||D||\psi_k\rangle|^2\omega_k}{3(2j+1)} \tag{5.3}$$

where j is the degeneracy of the state of interest, $|\psi\rangle$, and D is the dipole operator. For ground state alkali atoms, $J = 1/2$, so $j = 2$. We can combine equations 5.1 and 5.3 to write the dynamic polarizability as

$$\alpha(\omega) = \frac{2}{3(2j+1)} \sum_k \frac{|\langle\psi||D||\psi_k\rangle|^2 \omega_k}{\omega_k^2 - \omega^2}. \tag{5.4}$$

It is also common to refer to a line strength $S_k = |\langle\psi||D||\psi_k\rangle|^2$. Using this definition, the polarizability becomes

$$\alpha(\omega) = \frac{2}{3(2j+1)} \sum_k \frac{S_k \omega_k}{\omega_k^2 - \omega^2}. \tag{5.5}$$

I have found the conversion of quantities between atomic and S.I. units to be easy to miscalculate and I recommend checking every calculation against a benchmark such as static polarizabilities, transition energies, and literature values of matrix elements. In addition, I recommend keeping a copy of Hilborn's article "Einstein coefficients, cross sections, f values, dipole moments, and all that" [82] nearby.

So far we have only considered the valence electrons in our polarizability model. Equation 5.1 is typically modified to include a core polarizability term, α_{core}, and a valence-core coupling term, α_{vc}:

$$\alpha(\omega) = \sum_k \frac{f_k}{\omega_k^2 - \omega^2} + \alpha_{\text{core}} + \alpha_{\text{vc}}. \tag{5.6}$$

The core and valence-core coupling terms do not have a significant frequency dependence in the optical range. In addition, the valence term is typically broken up into the strongest terms that are explicitly written out with a frequency dependence, plus a "tail" contribution that is frequency independent and small. When considering the polarizability in the vicinity of the D1 or D2 lines in alkali atoms it is often sufficient to write

$$\alpha(\omega) = \frac{f_{D1}}{\omega_{D1}^2 - \omega^2} + \frac{f_{D2}}{\omega_{D2}^2 - \omega^2} + \alpha_{\text{tail}} + \alpha_{\text{core}} + \alpha_{\text{vc}}. \tag{5.7}$$

Table 5.1: Theoretical contributions to the polarizability at $\lambda_{\text{zero}} = 769.971$ nm ($\omega_{\text{zero}} = 2\pi \times 389.356$ THz), the first magic-zero wavelength of potassium [81]. Atomic units are used for the matrix elements and the polarizability. The slope of the dynamic polarizability near this λ_{zero} is $\partial\alpha/\partial\lambda = -42500\ a_0^3/\text{nm}$ and the uncertainty in the polarizability near this λ_{zero} is 100 a_0^3. This results in a theoretical uncertainty in λ_{zero} of $\delta\lambda_{\text{zero}} = (\partial\alpha/\partial\lambda)|_{\lambda_{\text{zero}}}^{-1}\delta\alpha(\lambda_{\text{zero}}) = 2.5$ pm.

Contribution	$|\langle 4s_{1/2}||D||np_{1/2}\rangle|$	$\alpha(\omega_{\text{zero}})$
$4p_{1/2}$	4.106(6)	-32085(62)
$4p_{3/2}$	5.807(7)	32079(77)
$5p_{1/2}$	0.271(5)	0.30(1)
$5p_{3/2}$	0.398(8)	0.65(2)
α_{tail}		0.16(12)
α_{core}		5.46(27)
α_{vc}		-0.18(1)
α_{total}		0(100)

The rotating wave approximation, $\omega_0^2 - \omega^2 \approx 2\omega_0(\omega_0 - \omega) = 2\omega_0\Delta$, can also be used to simplify the polarizability near resonance. A factor of ω_0 conveniently cancels in the numerator and the denominator when expressing polarizability near resonance using the line strengths S_k:

$$\alpha(\omega) = \frac{2}{3(2j+1)} \sum_k \frac{S_k}{\Delta_k}. \tag{5.8}$$

Static terms corresponding to tail, core, and valence-core contributions can be added if desired.

Table 5.1 summarizes the contributions of each of these parameters near the first magic-zero wavelength of potassium. Uncertainties in the $4s$ to $4p_{1/2}$ (D1) and $4p_{3/2}$ (D2) line strengths dominate the uncertainty of λ_{zero}. Our λ_{zero} measurement determines the ratio of these line strengths. Future measurements of additional λ_{zero} in potassium and other atoms will determine different ratios of matrix elements or the core polarizability, depending on the the relative uncertainties of these parameters.

As stated previously, the energy shift of a polarizable atom is given by

$$U(\omega) = -\frac{1}{2}\alpha(\omega)\vec{E}^2(\omega, z, t) \tag{5.9}$$

where we now allow for a frequency dependence for the polarizability and the electric field. For optical frequencies, we can only measure the energy shift due to the time average of the electric field, i.e. the intensity. The intensity is related to the electric field amplitude by $I = c\epsilon_0|E|^2/2$. From this, we can find that the phase acquired along one interferometer path is given by $\alpha(\omega)$ and the intensity of the light $I(x, z)$ at that location:

$$\phi_0(\omega) = \frac{\alpha(\omega)}{2\epsilon_0 c\hbar v}\int_{-\infty}^{\infty} I(x, z)dz. \tag{5.10}$$

Similar to the static polarizability experiment, where we used a static electric field gradient, here, we use an intensity gradient to apply different phase shifts to each interferometer path. We measure the differential phase shift of the two interferometer paths. Measurements of these differential phase shifts as a function of optical frequency, or wavelength, let us determine λ_{zero}.

5.2   Data analysis procedures

In this section we will describe in detail how we processed approximately 12,000 atom interferometer fringes (the result of about 6 billion atoms) to ultimately report our precision measurement of λ_{zero}.

We measured atom interferometer fringes in 5 s chunks of data and fit these fringes to determine the interferometer phase and contrast [52, 54]. During each 5 s of data, the measured atom beam flux was typically 10^5 counts/s and the measured fringe contrast was typically 25%. We used a mechanical shutter to alternately measure the interferometer fringes with and without laser light. The interferometer phase drifted at a rate of about 5 rad/hr, due primarily to thermal fluctuations of the apparatus. We fit the light-off reference phase to a smoothing spline and

then subtracted the spline from the light-on phase to determine the interferometer phase shift. Figure 5.1 shows the measured laser power, laser wavelength, phase shift, reference phase residuals, and contrast for each 5 s data file during a 30 min measurement of λ_{zero}. The statistical uncertainties of the contrast and phase were determined by the χ^2 minimization algorithm (reduced χ^2 values were typically 1.2-1.4). Unfortunately, the interferometer phase was less stable than the precision that each data file suggested that it should be, and this is ultimately the dominate source of statistical uncertainty in our experiment. Improving the interferometer stability is a long-standing goal of our lab. Changing the parameters of the smoothing spline can result in a random change of up to several picometers to the best-fit λ_{zero} of most of the individual data series but does not significantly alter the overall average λ_{zero}.

After the initial data processing, we normalized the phase shift data by laser power to control for drifts of the tapered amplifier power and fiber coupling efficiency. In addition, polarization changes due to propagation through the fiber were converted to power instability by a polarizing beam splitter. The power-normalized phase shift data were then binned by wavelength, and the average, standard deviation, and standard error of the mean of the central 80% of each bin was calculated. Figure 5.2 shows the resulting average power-normalized phase shift data vs. wavelength. We performed a non-linear least-squares fit of this data to equation 4 from Appendix C to determine the λ_{zero} for each data series. For this fit, we weighted the normalized phase shift data by the standard error of the mean for each wavelength bin. The statistical error of each λ_{zero} measurement was determined by the fit routine. The standard deviation is only shown for reference. The quality of fit shown in Figure 5.2 is typical of the entire data set.

Our reported λ_{zero} measurement is the result of 35 individual measurements of λ_{zero}, such as the one shown in Figure 5.2. Each λ_{zero} measurement and an estimate of its statistical uncertainty is shown in Figure 5.3. A histogram of the 35 measurements is shown in Figure 5.4. Note that these measurements have not been corrected for a constant Doppler shift of 0.56(5) pm.
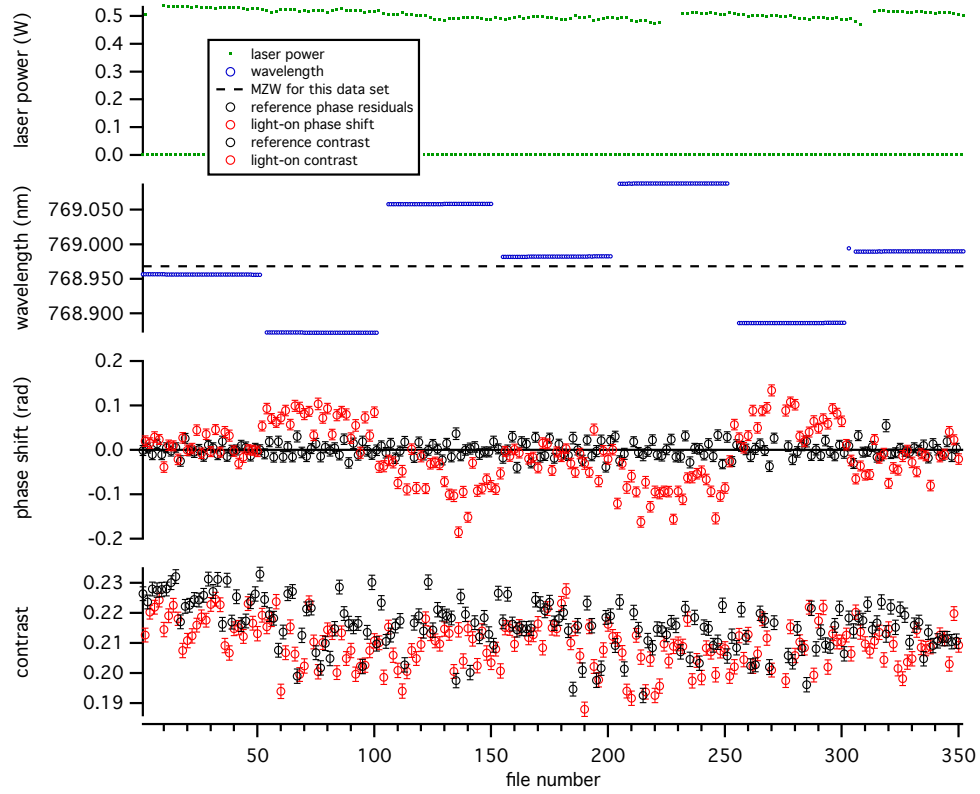
Figure 5.1: Laser power, laser wavelength, reference atom interferometer phase residuals and contrast, and light-induced atom interferometer phase shift and contrast vs. data file number. Each data point corresponds to 5 s of integration time. 29 out of 350 data points were deleted in this data set due to instabilities in either the laser power or wavelength during the 5 s integration time, and the phase shift data is ignored for these files. These deletions are accomplished using an unbiased and automated filter algorithm. These data are then further analyzed by normalizing the phase shift data by the laser power, and then binning and averaging the normalized phase shift data by wavelength, as shown in Figure 5.2. The particular data shown here is data set 120509e.
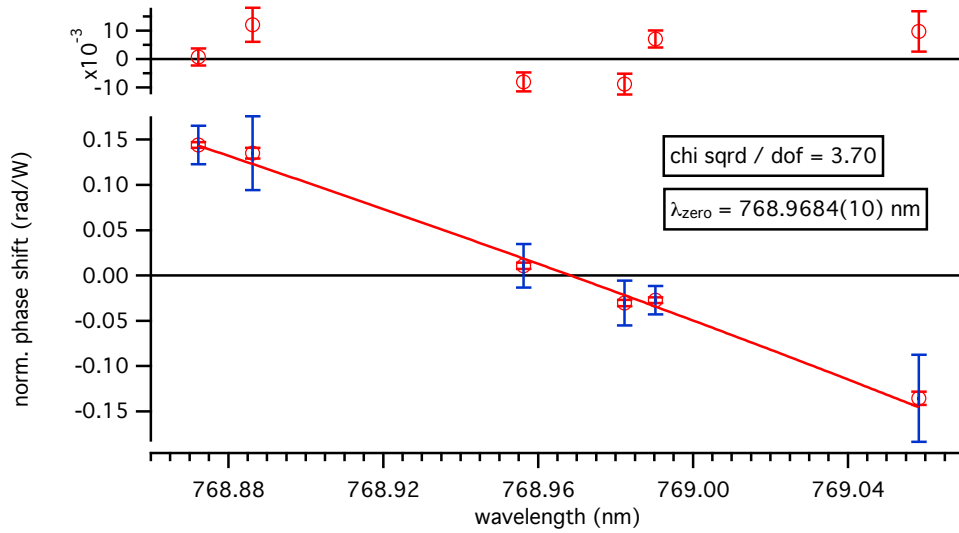
Figure 5.2: Power-normalized average phase shift vs. wavelength for data series 120509e. The red error bars are the standard error of the mean and the blue error bars are the standard deviation of the phase shifts measured at each wavelength. The 1.0 pm best-fit uncertainty of λ_{zero} in this data series comes from χ^2 minimization using input uncertainties of the standard error of the mean of the averaged phase shifts at each wavelength. The λ_{zero} reported from this data series is compared to 34 other measurements each made in a similar way in Figure 5.3.
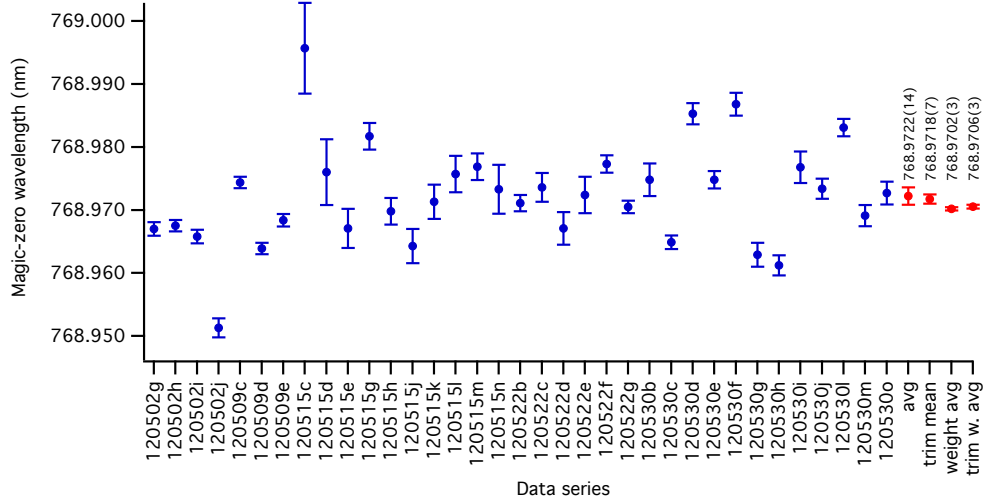
Figure 5.3: 35 separate λ_{zero} measurements (blue) and the average calculated in 4 different ways (red). The overall average is $\lambda_{\text{zero}} = 768.9722(14)$, the average of the central 80% of the data is $\lambda_{\text{zero}} = 768.9718(7)$ nm, the weighted overall average is $\lambda_{\text{zero}} = 768.9702(3)$ nm, and the weighted average of the central 80% of the data is $\lambda_{\text{zero}} = 768.9706(3)$ nm. The error bars for each individual measurement show the uncertainty that was determined by χ^2 minimization. However, as shown here, we found the experiment was not as reproducible as the reported individual measurement errors would suggest. Furthermore, the deviation from the mean was also uncorrelated with the size of the statistical error. Therefore, we assumed the statistical errors of all measurements were the same, and we report the standard error of the trimmed mean as the final statistical uncertainty. This data has not been corrected for a 0.56(5) pm Doppler shift. Figure 5.4 shows a histogram of these data.

The reproducibility of the 35 λ_{zero} measurements shown in Figure 5.3 is clearly much worse than the individual statistical errors. Furthermore, even the relative sizes of the individual statistical errors appear highly suspect since the reproducibility of the measurements i.e. the deviation from the mean, is uncorrelated with the size of the statistical errors. We therefore chose to assume that the statistical error of each data set was the same. We do not feel justified taking the weighted mean of these measurements because we do not believe the statistical errors associated with the each of the 35 individual measurements are accurate.

If we take the average of all 35 measurements and calculate the standard error
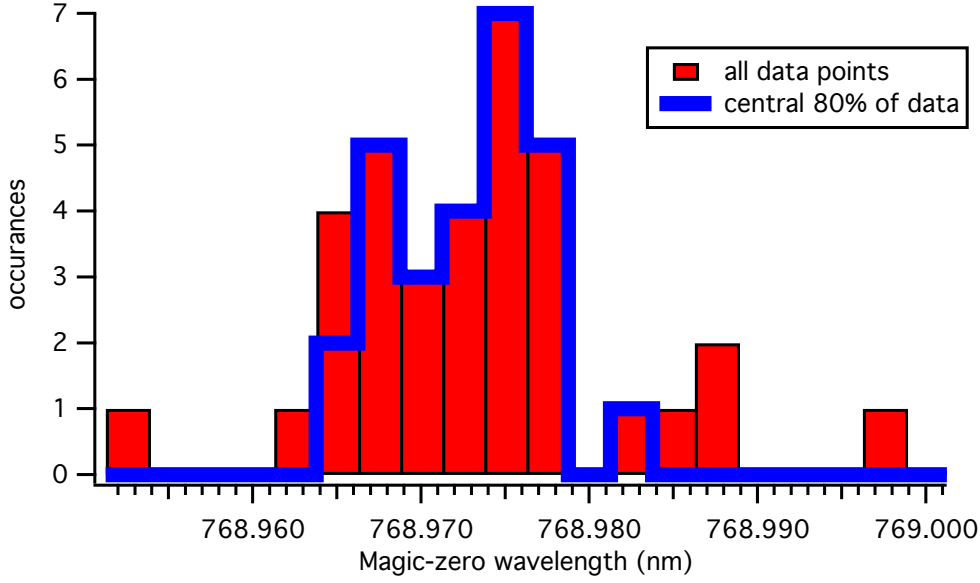
Figure 5.4: Histogram of λ_{zero} measurements. The central 80%, used for the calculation of the trimmed mean, is highlighted in blue.

of the mean, we find $\lambda_{\text{zero}} = 768.9722(14)$ nm. Eliminating the highest and lowest 10% of the data yields the reported measurement of $\lambda_{\text{zero}} = 768.9718(7)$ nm (again, without the Doppler shift correction). The weighted average of all 35 points is $\lambda_{\text{zero}} = 768.9702(3)$ nm, and the weighted average of the central 80% of the data is $\lambda_{\text{zero}} = 768.9706(3)$ nm. The statistical errors associated with the weighted averages are unrealistically small, yet, the central values are within 1.2 pm (2σ) of unweighted averages.

5.3 Derivation of a fundamental limit for the sensitivity of a λ_{zero} measurement

Decoherence due to spontaneous emission [83, 84] limits the precision with which λ_{zero} can be measured. The probability of an atom scattering zero photons, $P(0)$, affects the interferometer contrast through $C = C_0 P(0)$, where C_0 is the reference contrast. Given a Poisson distribution for $P(0)$,

$$C = C_0 e^{-N(\omega)} \tag{5.11}$$

where $N(\omega)$ is the average number of photons an atom scatters while exposed to the laser beam with frequency ω for a time T. $N(\omega)$ is proportional to the time-averaged probability for atoms to be in an excited state, P_{ex}, and the decay rate Γ:

$$N(\omega) = P_{ex}T\Gamma. \tag{5.12}$$

When the excitation probability is much less than 1, and using the rotating wave approximation, we can write P_{ex} in terms of the Rabi frequencies $\Omega_e = |\langle e|\boldsymbol{d}.\hat{\boldsymbol{\epsilon}}|g\rangle|E_0/\hbar$ and the detunings Δ_e from each resonance:

$$P_{ex} = \frac{1}{2}\sum_e \frac{\Omega_e^2}{\Delta_e^2 + \Omega_e^2} \tag{5.13}$$

The probability of an atom scattering 1 or more photons is $P_s = 1 - P(0)$. To obtain a simple expression for P_s we make the approximation

$$P(0) \approx 1 - N(\omega) \tag{5.14}$$

Using this approximation, we can write

$$P_s = N(\omega) = P_{ex}T\Gamma = T\Gamma\frac{1}{2}\sum_e \frac{\Omega_e^2}{\Delta_e^2 + \Omega_e^2}. \tag{5.15}$$

To compare P_s to the phase shift, we further assume $\Delta_e^2 \gg \Omega_e^2$ and rewrite P_s as

$$P_s = P_{ex}T\Gamma = \frac{IT\Gamma}{\epsilon_0 c\hbar^2}\sum_e \frac{|\langle e|\boldsymbol{d}.\hat{\boldsymbol{\epsilon}}|g\rangle|^2}{\Delta_e^2}. \tag{5.16}$$

In the rotating-wave approximation, the slope of the phase shift is

$$\frac{d\phi}{d\omega} = \frac{IT}{2\epsilon_0 c\hbar^2}\sum_e \frac{|\langle e|\boldsymbol{d}.\hat{\boldsymbol{\epsilon}}|g\rangle|^2}{\Delta_e^2}. \tag{5.17}$$

Comparison of Eqs. (5.17) and (5.16) yields a maximum achievable slope of

$$\frac{d\phi}{d\omega} \approx \frac{1}{2\Gamma} P_s.$$ (5.18)

In terms of the wavelength, the slope is

$$\frac{d\phi}{d\lambda} = \frac{d\phi}{d\omega}\frac{d\omega}{d\lambda} \approx \frac{\pi c P_s}{\lambda^2 \Gamma}.$$ (5.19)

As discussed in Appendix C, the highest sensitivity could be achieved if $P_0 = e^{-1}$, implying an optimum $P_s = 1 - e^{-1}$. Given this requirement, we determine that the error made by the approximation in Eq. (5.14) is $\approx 30\%$. Still, the simple formulation of the maximum achievable slope presented in Eq. (5.18) remains a useful guide to possibility of large improvements in the precision of λ_{zero} measurements.

5.4 Contrast loss due to inhomogeneous mechanisms

Although the phase shift is the primary signal in our measurement of λ_{zero}, it is still important to have a full understanding of the interferometer contrast loss. This provides a valuable check on our understanding of the potential errors associated with the measurement. Here we will examine three mechanisms of contrast loss, all analogous to inhomogenous broadening.

As stated in equation 5.10, the phase acquired along one path in the atom interferometer is

$$\phi_{0,q,|Fm_F\rangle}(\omega, x, v) = \frac{\alpha_{q,|Fm_F\rangle}(\omega)}{2\epsilon_0 c\hbar v} \int_{-\infty}^{\infty} I(x, z)dz.$$ (5.20)

Here we have written the phase as an explicit function of the atom wave position x, velocity v, light polarization q, and state $|Fm_F\rangle$ to more easily explain the contrast loss mechanisms. Next, we assume that the focused laser beam intensity distribution in the plane of the interferometer is represented by a Gaussian function

$$I(x_l, z_l) = I_0 e^{-2(x_l^2 + z_l^2)/w_0^2}$$ (5.21)

where w_0 is the beam waist, $I_0 = 2P_L/(\pi w_0^2)$ and P_L is the laser power. Integrating the acquired phase (Eq. (5.20)) along the beam path (z) gives

$$\phi_{0,q,|Fm_F\rangle}(\omega, x, v) = \frac{\alpha_{q,|Fm_F\rangle}(\omega)\sqrt{\pi/2}w_0 I_0}{2\epsilon_0 c\hbar v}e^{-2(x-x_l)^2/w_0^2},$$ (5.22)

or in terms of the laser power and beam waist

$$\phi_{0,q,|Fm_F\rangle}(\omega, x, v) = \frac{\alpha_{q,|Fm_F\rangle}(\omega)P_L}{\sqrt{2\pi}\epsilon_0 c\hbar v w_0}e^{-2(x-x_l)^2/w_0^2}.$$ (5.23)

The differential phase shift between the two paths of the two interferometers formed by the +1 and 0, and the 0 and -1 diffraction orders is

$$\phi_{1,q,|Fm_F\rangle}(\omega, x, v) = \phi_{0,q,|Fm_F\rangle}(\omega, x + s(v), v) - \phi_{0,q,|Fm_F\rangle}(\omega, x, v)$$ (5.24a)

$$\phi_{-1,q,|Fm_F\rangle}(\omega, x, v) = \phi_{0,q,|Fm_F\rangle}(\omega, x, v) - \phi_{0,q,|Fm_F\rangle}(\omega, x - s(v), v)$$ (5.24b)

where $s(v)$ is the velocity-dependent path separation [8].

The velocity distribution in our supersonic atom beam is well-described by a Gaussian distribution

$$P(v) = \frac{1}{\sqrt{2\pi\sigma_v^2}}\exp\left(-\frac{(v-v_0)^2}{2\sigma_v^2}\right)$$ (5.25)

where v_0 is the mean velocity and σ_v is the velocity distribution width. In our experiment $v_0 \approx 1600$ m/s and $v_0/\sigma_v \approx 15$.

Finally, we can predict the measured interferometer phase $\phi(\omega)$ and contrast $C(\omega)$ from the expression

$$C(\omega)e^{i\phi(\omega)} = C_0 e^{i\phi_0} \sum_{q=-1,0,1} f_q \sum_{k=-1,1} \frac{1}{2} \sum_{|Fm_F\rangle} \frac{1}{8} \int_{v=0}^{\infty} P(v) \int_{x=-d/2}^{d/2}$$
$$P(x)\exp(i\phi_{k,q,|Fm_F\rangle}(\omega, x, v))dvdx.$$ (5.26)

Here, f_q is the fraction of the power with q polarization, typically $f_0 = 80\%$ and
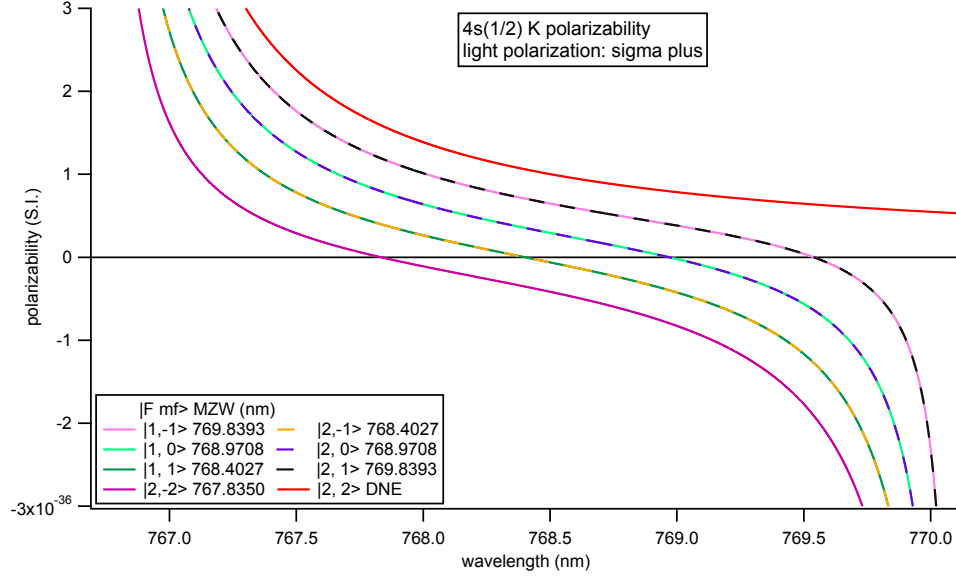
Figure 5.5: Polarizabilities and magic-zero wavelengths for different $|Fm_F\rangle$ ground states of potassium for σ^+ light.

$f_1 = 20\%$. The factor of $1/2$ accounts for equal detected intensity from the $+1$ and -1 interferometers. The factor of $1/8$ accounts for the fact that all 8 $|Fm_F\rangle$ states are equally likely in our thermal atom beam. We also assume that the atom beam intensity $P(x) = 1/d$ is uniform over the width d of the detected fringes. Figure 5.6 shows contrast loss spectra based on Eq. 5.26 with several conditions (e.g. zero beam width). Figure 1b in Appendix C shows the same data and the calculated contrast loss spectra for the conditions $d = 100$ μm, $\sigma_v = 110$ m/s, $w_0 = 110$ μm.

5.5 The effect of broadband light on λ_{zero} measurements

We have assumed, until now, that the optical spectrum contains only one frequency of significance. Unfortunately, due to the nature of our laser system, this assumption is not valid. Our laser system consists of tunable a 50 mW external cavity diode laser seeding a 2 W tapered amplifier [85, 86, 87]. Tapered amplifiers are notorious for producing a significant amount of broadband spontaneous emission ($\sim 10\%$ of the total power output) in addition to the amplified stimulated emission. Figure 2.12 shows a picture of the spectrum of the tapered amplifier power output after
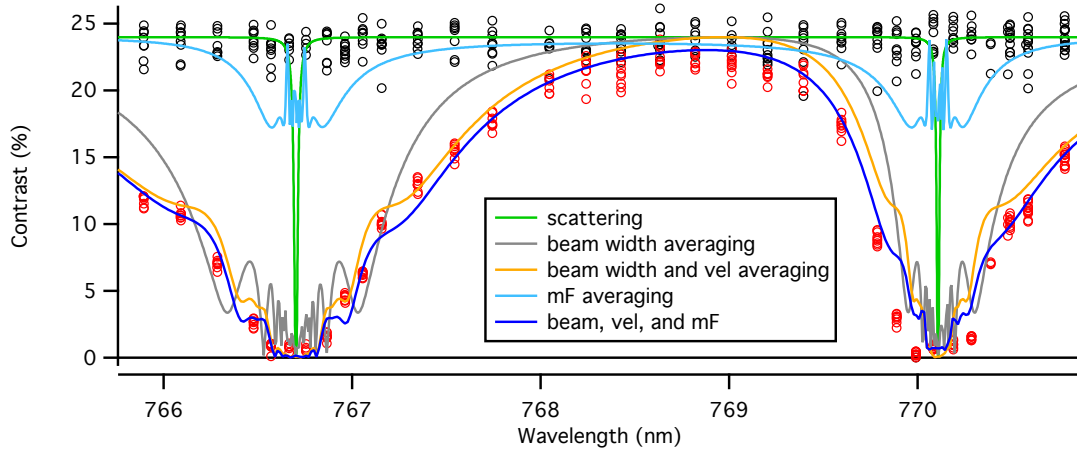
Figure 5.6: Measured interferometer reference contrast C_0 (black circles) and contrast C when exposed to light (red circles). Also shown is predicted interferometer contrast loss due to averaging over the beam width only (grey line), the beam width and the velocity distribution (orange line), multiple $|Fm_F\rangle$ states only (light blue line), and all three of the above mechanisms (dark blue line). Contrast loss from photon scattering only is also shown (green line).

diffraction from a grating. Figure 5.7 shows data acquired with a grating spectrometer under different TPA conditions. Under normal operating conditions (40 mW of seed light and a TPA current of 2.6 A) the broadband light spectrum is consistent with a gaussian with a center wavelength of $\lambda_{\mathrm{spon}} = 763$ nm and a width of $\sigma_{\mathrm{spon}} = 3$ nm. Spontaneous emission from the tapered amplifier diverges at a different rate than the stimulated emission. We use this fact to reduce the fraction of spontaneous emission by an order of magnitude by spatially filtering the tapered amplifier output with a single mode fiber [88].

To account for the broadband light, the phase shift (equation 5.10) becomes

$$\phi(\omega) = \frac{1}{\epsilon_0 c \hbar v} \int_{z=-\infty}^{\infty} \int_{\omega=0}^{\infty} \alpha(\omega) I(\omega; x, z) dz d\omega. \tag{5.27}$$

Figure 5.8 shows a model of the broadband light spectrum with the dynamic polarizability near the potassium D1 and D2 lines.
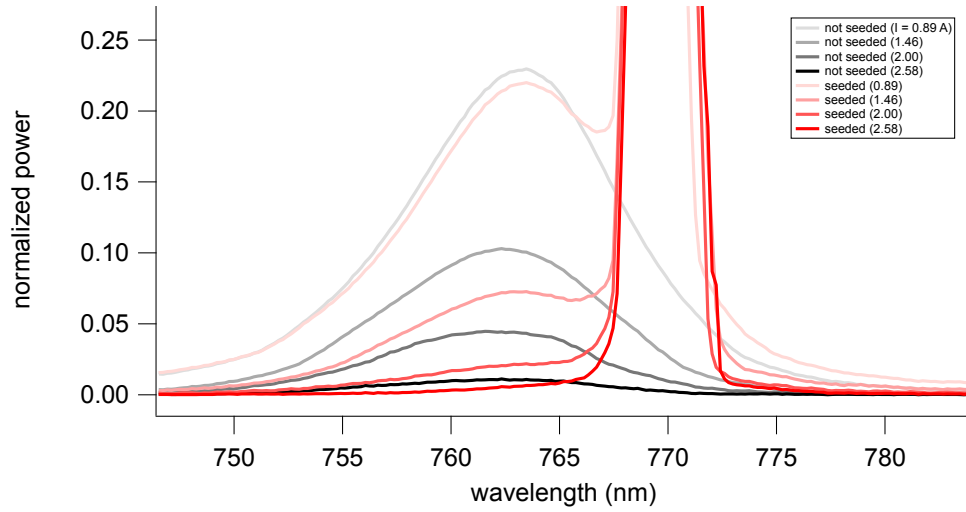
Figure 5.7: Laser system spectrum before filtering by a single mode fiber for 4 different tapered amplifier injection currents: 0.89 A, 1.46 A, 2.00 A, and 2.58 A. Black curves are the unseeded tapered amplifier spectrum (spontaneous emission only). Red curves are the spectrum when the tapered amplifier is seeded. The darkness gradient corresponds to low (faint) to high (dark) currents. For each of the 4 currents, both the unseeded and seeded spectrum is normalized so that the maximum observed power is equal to 1. Thus it is evident that as the tapered amplifier injection current increases, the broadband light component decreases. The grating spectrometer resolution is approximately 0.3 nm, and this causes a blurring of the high power stimulated emission peak.
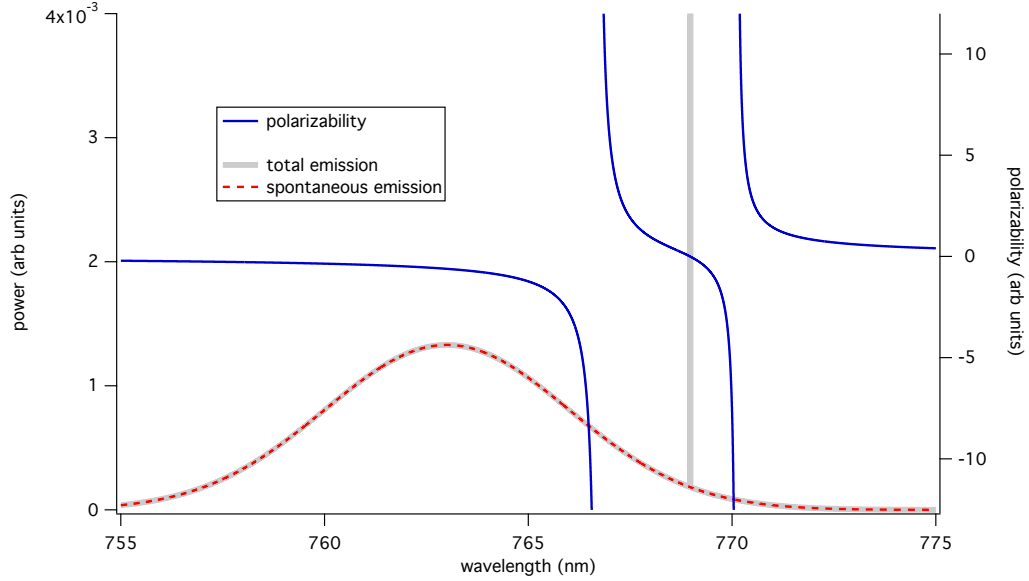
Figure 5.8: Model of the laser system spectrum and the dynamic polarizability of K. The broadband light component is set to be 1% of the total laser power. The majority of the broadband light is blue-detuned of the D2 line, and thus there is a net phase shift due to the integrated spectral density of the broadband light.

5.6 Next-generation λ_{zero} measurements

The existence of a λ_{zero} near 770 nm in potassium was fortunate for our lab. We chose to study this particular λ_{zero} for several reasons. First, potassium is cheap and easy to handle, and it is easy to generate and detect beams of potassium atoms in our lab. Second, the primary transitions are strong and the fine structure splitting of the $4p$ levels in potassium is only 3 nm, and this leads to a larger slope and thus easier to determine λ_{zero}. Third, inexpensive and easy-to-operate diode lasers and amplifiers are available near 770 nm.

Future measurements of magic-zero wavelengths in our lab will not have all of these advantages. Therefore, we are exploring ways to increase the light-induced phase shift in our atom interferometer and improve the reproducibility of the measurements. Three ideas to improve the signal size are a "hall of mirrors" (Figure 5.9), a power build-up cavity (Figure 5.10), and a coaxial atom-light interaction region (Figure 5.11). All of these ideas would rely on light delivered into the vacuum
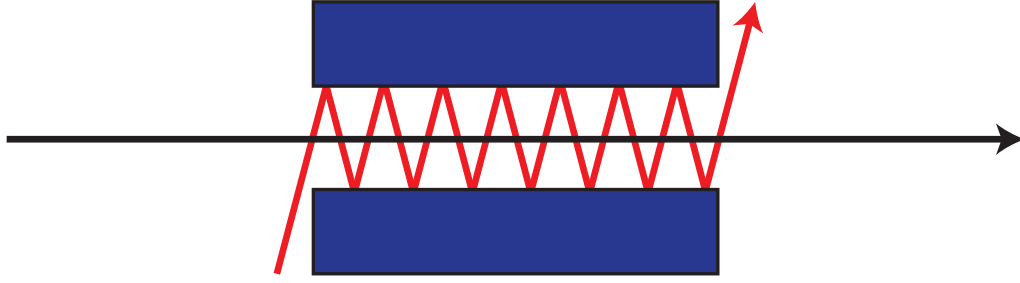
Figure 5.9: A "hall-of-mirrors" for improved measurements of λ_{zero}. A hall-of-mirrors allows the laser beam to intersect the atom beam multiple times to create a larger phase shift. Nearly parallel mirrors and an appropriate choice of the focusing power of the lens may result in 30-50 times larger phase shifts.

chamber by a single-mode optical fiber, and all optics would be rigidly attached to improve the stability and reproducibility of the experiment.

We have already built a hall of mirrors and used it to measure the same λ_{zero}. The slope $d\phi/d\lambda$ is as much as 10 times larger as in our published experiment. Furthermore, the reproducibility during a single day is also improved and now consistent with the statistical error of a single λ_{zero} measurement. We attribute this improvement in reproducibility to the increased mechanical robustness of the hall of mirrors system.
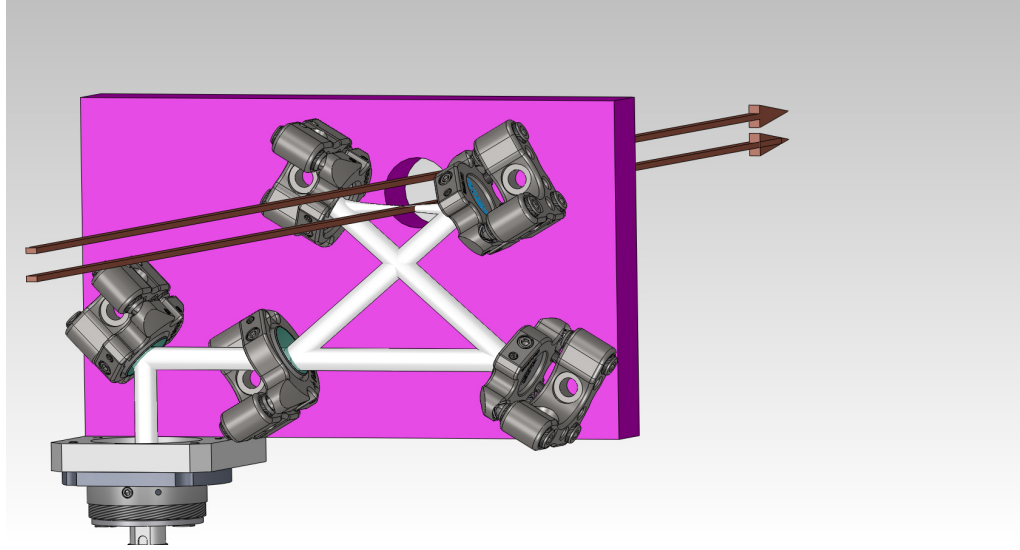
Figure 5.10: A power build-up cavity for improved measurements of λ_{zero}. A power build-up cavity could provide 50-100 times larger phase shift for reasonable mirror reflectivities.
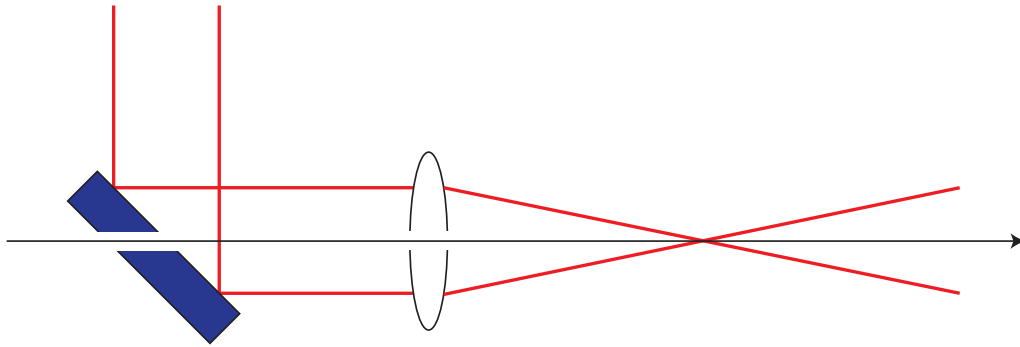
Figure 5.11: A coaxial atom-light interaction region for improved measurements of λ_{zero}. Light focused along the path of the atom beam could interact with the atoms for a significantly longer amount of time, leading to 50-100 times larger phase shifts. A small hole drilled in the mirror and lens would allow the atom beam to pass through while only reducing the total optical power by a few percent. The atoms would see significantly Doppler-shifted light, so an accurate measurement of the atom beam velocity is required in this system.

CHAPTER 6

STRONTIUM POLARIZABILITY MEASUREMENT PROPOSAL

We propose to measure the strontium ground $5s^2$ $^1S_0$ and metastable $5s5p$ $^3P_0$ polarizabilities to provide crucial tests of atomic structure calculations needed for next generation atomic clocks [11] and [3]. Due to uncertain polarizabilities of the clock states, the Sr and Yb clocks until recently had an uncertainty that is 70-250 times larger than their ultimate lifetime-limited precision [3, 89]. The polarizability influences the clock frequency because blackbody radiation from the thermal environment causes relatively large, uncertain Stark shifts of the clock states. Recent *in situ* measurements of the differential polarizability of the clock states of Sr [90] and Yb [91] have significantly reduced the uncertainties due to the BBR shift. However, measurements of the polarizabilities of the individual states are still in high demand due to the importance of accurate calibration of the BBR shift and due to the difficulty of calculating these polarizabilities.

In this chapter we will discuss in detail the three technical challenges of measuring α_{Sr} and α_{Sr*}:

- Detection of ground state Sr with resonant photoionization.

- Detection of metastable state Sr using resonant and non-resonant photoionization.

- Metastable Sr generation using electron impact ionization.

6.1 Detection of ground state Sr

6.1.1 Photoionization via 461 and 405 nm transitions

The ionization energy of the ground $5s^2$ $^1S_0$ state of strontium is 5.7 eV. This high ionization energy makes strontium difficult to ionize using our current hot-wire
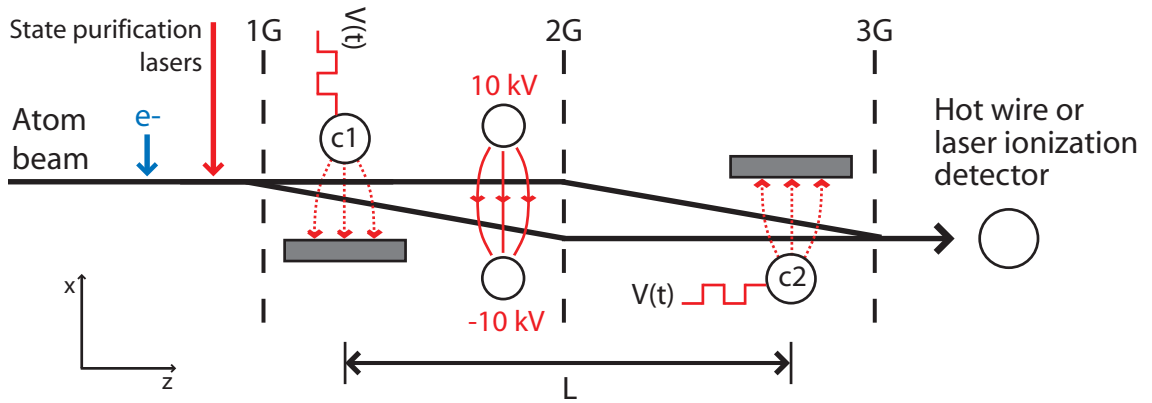
Figure 6.1: Atom interferometer set-up for strontium and ytterbium polarizability measurements. Nanogratings 1G, 2G, and 3G form a Mach-Zehnder atom interferometer. To measure beam velocity, we apply a periodic voltage $V(t)$ to two phase choppers (c1 and c2) separated by a distance L and study the contrast of the interferometer as a function of switching frequency. To measure polarizability, we apply ± 10 kV across the interferometer to induce a polarizability-dependent phase shift. We will use an electron bombardment region to promote Sr and Yb atoms to a metastable state, followed by resonant lasers to purify the beam in the $^3P_0$ state. Beam detection will be accomplished with resonant laser ionization. Diagram not to scale.

detector. We will discuss an efficient resonant photoionization pathway via a 461 nm photon to the 5s5p $^1P_1$ state and a 405 nm photon to the autoionizing state $5p^2$ $^1D_2$ [92, 93, 94] (see Figure 6.2). We show that resonant photoionization will provide ~20% ionization probability with nearly zero background. We will assume that all lasers will be focused to a spot size of $A=(100\ \mu m)^2$ and that the atom beam velocity $v = 3000$ m/s.

The $^1S_0$ - $^1P_1$ transition at 461 nm has an A_{21} coefficient of 1.9×10^8 Hz. This corresponds to a state lifetime $\tau = 5.3$ ns and $I_{sat} = 40$ mW/cm^2. Assuming a spot size of $(100\ \mu m)^2 = 10^{-8}$ m^2, 4 μW is needed to saturate this transition. The Rabi frequency $\Omega = \Gamma\sqrt{I/2I_{sat}}$ and for a two-state atom $\Gamma = A_{21}$. We will approximate the probability of finding a two-level atom in the excited state when $I = I_{sat}$ as $P \approx 1/2$.

Absorption of a 405 nm photon takes an atom in the excited 5s5p $^1P_1$ to the $5p^2$ $^1D_2$ autoionizing state. The presence of this autoionizing state causes the ionization cross-section of the $^1P_1$ state with 405 nm light to be 10^3 to 10^6 times larger than typical non-resonant photoionization cross-sections: $\sigma = 5600$ Mb (1 Mb = 10^{-22} m^2).

We will now calculate the ionization probability a strontium atom in the ground state via this resonant ionization path. First, we write the single atom ionization rate from the $^1P_1$ state as

$$\Gamma_{1P1-Sr^+} = \sigma\Phi_\gamma = \sigma\frac{I_{405}}{E_\gamma} \tag{6.1}$$

where σ is the ionization cross-section, Φ_γ is the 405 nm photon flux, I_{405} is the laser intensity for a beam with power P_{405} focused to a spot size A, and $E_\gamma = hc/\lambda$ is the photon energy. We calculate $\Gamma_{1P1-Sr^+} = 10^7$ s^{-1}, assuming $P_{405} = 100$ mW and $A=(100\ \mu m)^2$. Next, we must consider the time that the atom beam interacts with the ionization laser: $T = l/v$, where $l = \sqrt{A}$ is the interaction length. $T = 30$ ns, assuming a beam velocity of 3000 m/s. The probability of photoionization from
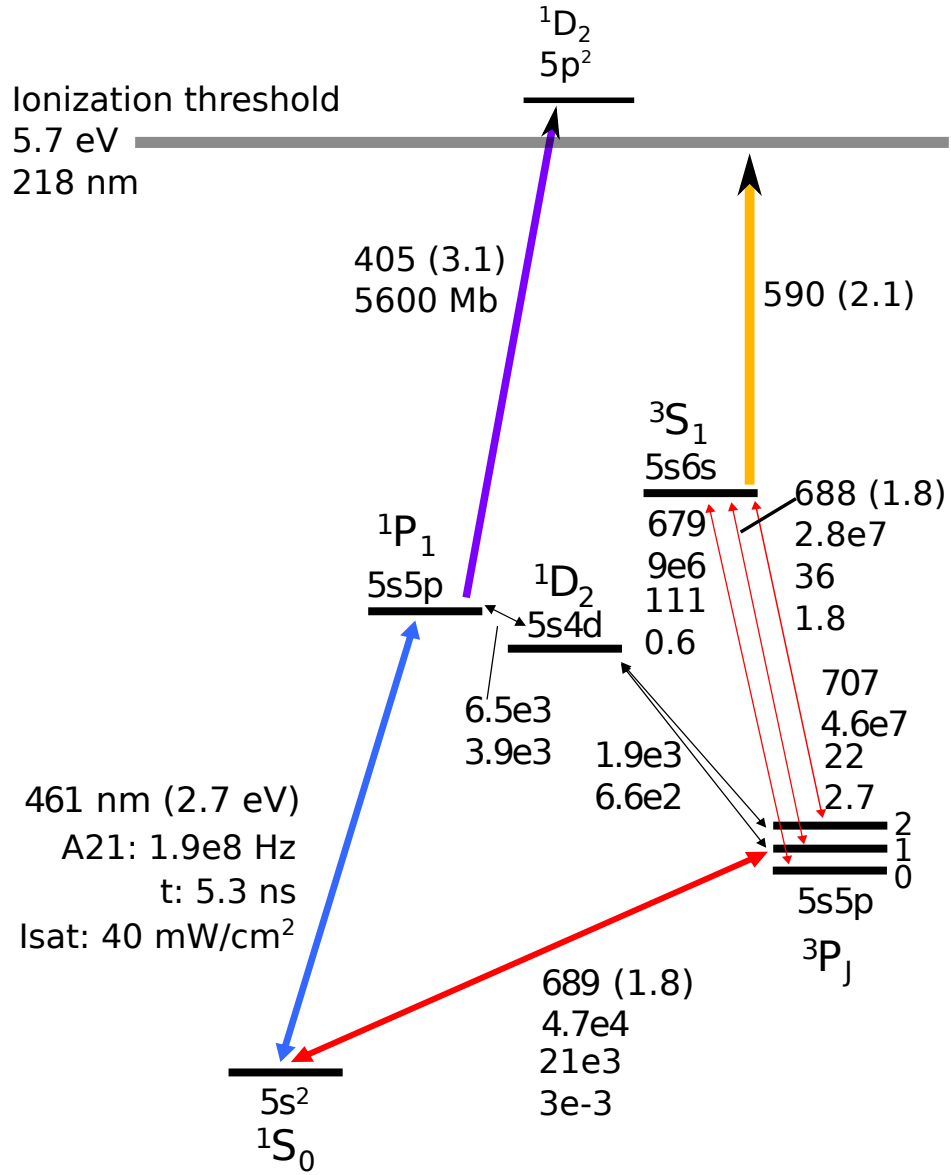
Figure 6.2: Sr term diagram. Transition wavelengths (nm), photon energies (eV), Einstein A_{21} coefficients (Hz), lifetimes (ns), and I_{sat} (mW/cm^2) are shown next to each transition. Adapted from Ludlow [3]. Note: $\Omega = \Gamma\sqrt{2I/I_{sat}}$.

the $^1P_1$ state is then

$$\mathrm{Prob}_{1P1-Sr^+} = \Gamma_{1P1-Sr^+}T = \sigma\frac{P}{E_\gamma v\sqrt{A}}. \qquad (6.2)$$

Using the above assumptions, we calculate an ionization probability of 38% from the $^1P_1$ state. We assume that the intensity of light resonant with the $^1S_0$ - $^1P_1$ transition is sufficient to put atoms in the $^1P_1$ state 50% of the time, and then estimate the ground state ionization probability of our system to be $\mathrm{Prob}_{1S0-Sr^+} = 10 - 20\%$.

This resonant photoionization detection efficiency is comparable to our hot-wire detector efficiency with potassium, rubidium, and cesium atoms. However, the resonant photoionization method will presumably have a much lower noise floor than the hot-wire method. Therefore, we can expect that resonant photoionization will work for our system even if our ionization probability estimates are off by several orders of magnitude.

6.1.2 Generating 461 and 405 nm light

Several possibilities exist for generating 461 nm light: frequency doubling 922 nm light, a blue LED, a strontium hollow cathode lamp, and an AR-coated laser diode.

First, we discuss second harmonic generation of 461 nm light. The efficiency of SHG of 922 nm to 461 nm varies from 0.01-75% [93, 95] depending on the effort expended, expertise of the lab, cavity specifications, and type of crystal used. A PPKTP crystal can achieve 1% conversion efficiency with a single pass through the crystal when pumped with about 100 mW of 992 nm light, so no cavity would be needed. This may yield sufficient power and would be relatively simple. The crystal would need to be temperature tuned to 40-70 °C. We estimate that it is reasonable that 100 μW of resonant 461 nm light may delivered to the beam using SHG with a PPKTP. A prototype in our lab using a PPKTP crystal currently outputs about 10 μW of 461 nm light.

We also explored several other methods to generate 461 nm light. Blue LEDs with center wavelengths near 460 nm provide another possibility for generating 461

nm light. LEDs with optical powers of 1 W are available. The typical $\Delta\lambda = 25$ nm, corresponding to a frequency dispersion of $df = c/\lambda^2 d\lambda = 3 \times 10^{13}$ Hz. The linewidth of the ^{1}S$_0$ -^{1}P$_1$ transition is 30 MHz, so approximately 10^{-6} of the light generated in the LED, 0.1-1 μW, may be resonant with the atom beam.

Hollow cathode lamps are typically specified as producing 10-20 mA discharge current, however, the corresponding optical power is unknown. Typical operating voltages are 300 V. We assume an optical output power P, and that owing to the extended nature of the source, only 10% of the light may be delivered to the atom beam. The doppler-broadening of the light from a hollow cathode lamp will further reduce the effective power. We assume a temperature of 900 K and calculate a corresponding doppler width of 1.5 GHz. The linewidth of the ^{1}S$_0$ -^{1}P$_1$ transition is 30 MHz, so approximately 2% of the light generated in the lamp may be resonant with the atom beam. The above factors yield an efficiency of $0.002P$. Hollow cathode lamps are relatively inexpensive ($355), and require a 550 V, 20 mA power supply (available for $2125, although we have a supply that would probably work). Hollow cathode lamp lifetimes are warranted to 5000 mA hours. At 10 mA, the lifetime would be 500 hours, or about 20 days of continuous operation. This can be quickly implemented with little expertise, and may provide sufficient power.

Finally, Shimada *et al.* recently used a prototype AR coated diode from Nichia to generate 40 mW at 461 nm from an ECDL [96]. Commercialization of this diode technology would greatly simplify our strontium polarizability measurement.

6.2   Detection of metastable Sr

We now consider photoionization of the metastable ^{3}P$_0$ state. To our knowledge, no autoionizing triplet states exist, so non-resonant photoionization must be used with the metastable state. The ionization energy of the ^{3}P$_0$ state is 3.9 eV (318 nm). Therefore, direct photoionization of the ^{3}P$_0$ state would require an intense UV source. The near-threshold photoionization cross-section of the ^{3}P$_1$ state is $\sigma_{3P1} \approx 10$ Mb [94]. A UV lamp may provide sufficient power at this wavelength

to directly ionize the $^3P_0$ state. Wang [97] used a UV LED to photoionize $^3P_0$ Ba atoms. We are exploring if we can use UV light to photoionize the $^3P_0$ with sufficient efficiency. UV LEDs with 0.5 mW available for $\sim$\$150. High power (0.5 W) UV LEDs are common down to 365 nm.

We also considered the possibility of using a two photon ionization process via the 5s5p $^3P_0$ to 5s6s $^3S_1$ at 679 nm (1.8 eV), and then an ionizing photon with $\lambda < 590$ nm (2.1 eV). To our knowledge, no published photoionization cross-sections exist for the 5s6s $^3S_1$ state. Therefore, we estimate that the photoionization cross-section for the $^3S_1$ state is similar to that of the 5s6s $^1S_0$ state: $\sigma_{1S0} = 0.4$ Mb [98]. $^3S_1$ will also decay to $^3P_1$ and $^3P_2$, so we must apply the state purification lasers at detector as well to keep atoms in the $^3S_1$ state.

Another possible intermediate state is $5p^2$ $^3P_1$. The transition between 5s5p $^3P_0$ and $5p^2$ $^3P_1$ is at 474 nm (2.6 eV). The transition rate is 4×10^7 Hz [99]. A photon with $\lambda < 950$ nm (1.31 eV) would be needed to photoionize the $5p^2$ $^3P_1$ state. 473 nm diodes with several 10s of mW are available from several sources, including ThorLabs.

Yet another possible intermediate state is 5s5d $^3D_1$. The transition between 5s5p $^3P_0$ and 5s5d $^3D_1$ is at 483 nm (2.6 eV). The transition rate is 4×10^7 Hz [99]. A photon with $\lambda < 915$ nm (1.35 eV) would be needed to photoionize the 5s5d $^3D_1$ state. 490 nm diodes with several 10s of mW are available from several sources (Renesas NX6414EH, CrystaLaser, ThorLabs).

6.3   Generating metastable Sr

Metastable strontium and ytterbium will be generated in an electron bombardment region [100] and state purification will be accomplished with resonant lasers. The electron bombardment region will populate the nsnp^3P metastable triplets with 40% efficiency. We will build diode lasers at 679 and 707 nm to optically pump metastable strontium atoms from the $^3P_1$ and $^3P_2$ states into the $^3P_0$ state. We will also build diode lasers at 649 and 770 nm to purify the ytterbium metastable triplet. We have

prototypes of two of these lasers (679 and 770 nm) available from experiments with lithium and potassium atoms.

CHAPTER 7

TENSOR POLARIZABILITY MEASUREMENT PROPOSAL

Ground-state alkali atoms are spherically symmetric, and as a result the polarizability may be described by a scalar that does not depend on the direction of the applied field. In contrast, molecules are generally not spherically symmetric and their polarizabilities must be described by a tensor $\overset{\leftrightarrow}{\alpha}$. Knowledge of the tensor polarizabilities of alkali dimers is currently of interest for ultracold molecules [101]. Figure 2.14 shows the two unique orientations of an alkali dimer in an electric field. To our knowledge, only the average polarizability of this tensor has been measured [24, 20].

M.S. Chapman first proposed to measure the tensor polarizability of Na_2 by studying interferometer contrast loss as a function of applied electric field but dismissed the idea in favor of applying orthogonal electric fields to two well-separated paths of a molecule interferometer [102]. While there is significant merit to the orthogonal field approach, a separated path molecule interferometer even for Na_2 is a formidable challenge, and becomes more difficult for heavier atoms. Here, we examine in more detail the possibility of determining the tensor components of the molecular polarizability of alkali dimers by studying the unique contrast loss signal in our interferometer as a function of the applied electric field.

The Stark shift of a molecule with a tensor polarizability $\overset{\leftrightarrow}{\alpha}$ is given by

$$U = -\frac{1}{2}\vec{E}\overset{\leftrightarrow}{\alpha}\vec{E}. \tag{7.1}$$

In general, the polarizability tensor is most easily expressed in the body coordinates of the molecule. For a simple molecule such as an alkali dimer, the tensor is diagonal if one chooses to use the obvious axes of symmetry: one along the bonding axis of the molecule and two additional axes that are mutually orthogonal to the bonding

axis. If we let the z-axis coincide with the bonding axis of the dimer we can write the polarizability tensor as

$$\overset{\leftrightarrow}{\alpha} = \begin{pmatrix} \alpha_\perp & 0 & 0 \\ 0 & \alpha_\perp & 0 \\ 0 & 0 & \alpha_{||} \end{pmatrix} \tag{7.2}$$

Let the average polarizability of the molecule be defined as

$$\alpha = \frac{\alpha_{||} + 2\alpha_\perp}{3} \tag{7.3}$$

and let the anisotropy be defined as

$$\gamma = \alpha_{||} - \alpha_\perp. \tag{7.4}$$

We transform the electric field from the lab coordinate system into the body coordinate system to calculate the energy shift. From symmetry we expect that the energy can only depend on the polar angle θ. Let the electric field in the lab coordinate system be coincident with the lab z-axis. Following the standard coordinate system transformation matrices [103] we find

$$\begin{aligned} \vec{E}_{\text{body}} &= \begin{pmatrix} \cos(\psi) & \sin(\psi) & 0 \\ -\sin(\psi) & \cos(\psi) & 0 \\ 0 & 0 & 1 \end{pmatrix} \begin{pmatrix} 1 & 0 & 0 \\ 0 & \cos(\theta) & \sin(\theta) \\ 0 & -\sin(\theta) & \cos(\theta) \end{pmatrix} \begin{pmatrix} \cos(\phi) & \sin(\phi) & 0 \\ -\sin(\phi) & \cos(\phi) & 0 \\ 0 & 0 & 1 \end{pmatrix} \begin{pmatrix} 0 \\ 0 \\ E \end{pmatrix} \\ &= E \begin{pmatrix} \sin(\psi)\sin(\theta) \\ \cos(\psi)\sin(\theta) \\ \cos(\theta) \end{pmatrix} \end{aligned} \tag{7.5}$$

We may now calculate the energy shift

$$U = -\frac{1}{2}E^2 \left(\alpha_{||} - \gamma \sin^2 \theta \right). \tag{7.6}$$

We assume that a uniform electric field is applied to one path of the interferometer for a distance l. The interaction phase shift is then

$$
\begin{aligned}
\phi(E, \theta, v) &= -\frac{1}{\hbar v} \int U dx \\
&= \frac{E^2 l}{2\hbar v} \left(\alpha_{||} - \gamma \sin^2 \theta \right)
\end{aligned}
\tag{7.7}
$$

where v is the velocity of the molecule.

The phase shift of the measured interference fringe will be an incoherent sum of the phase shifts of molecules with a random spatial orientation. Additionally, we must the average the phase shifts of the velocity distribution, $P(v)$. The measured contrast C_m and phase shift ϕ_m will be

$$
C_m \exp(i\phi_m) = \int_{\theta=0}^{\pi} \int_{v=0}^{\infty} \exp(i\phi(E, \theta, v)) P(v) \sin(\theta) d\theta dv.
\tag{7.8}
$$

The incoherent sum of fringes formed by molecules with different spatial orientations leads to contrast loss and revivals. The revivals occur when the phase shift corresponding to $\alpha_{\perp}$ is an integer multiple of 2π times the phase shift corresponding to $\alpha_{||}$. The velocity distribution only leads to contrast loss. Figure 7.1 shows contrast loss due to these two different mechanisms for Na_2 molecules and the contrast loss due to both mechanisms combined for two different velocity distributions. Here, the velocity distribution width is parameterized by the sharpness $r = v_0/\sigma_v$.

A velocity distribution with a sharpness $r > 20$ is necessary to see the effect of anisotropy on the contrast loss signal. Alternatively, we could apply a counter-phase to reverse the contrast loss due to the velocity distribution at a given phase [77, 65]. We routinely observe velocity distributions sharper than 20, and even as large as 45 for Cs atoms. Significant experimental challenges include generating a bright enough molecule beam and eliminating the atomic component of the beam. It would also be interesting to consider the signal from a planar molecule such as benzene if a suitable detector (such as an electron impact ionizer) could be developed.
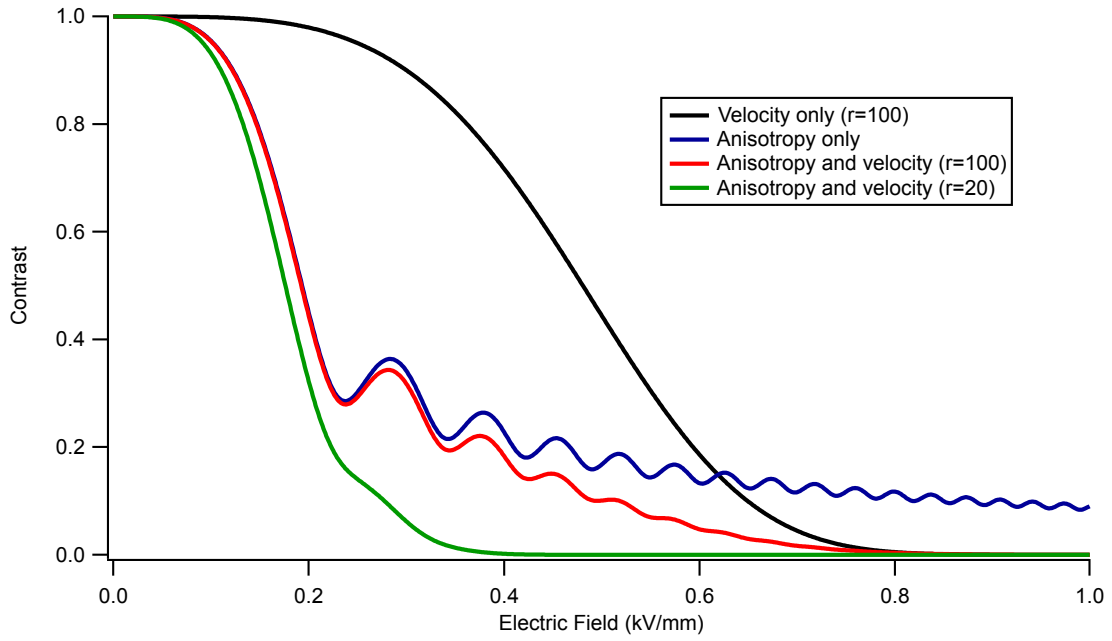
Figure 7.1: Contrast loss due to anisotropy, velocity distribution, and both mechanisms combined for Na_2 molecules. A velocity distribution with a sharpness better than $r = v_0/\sigma_v > 20$ is necessary to see the effect of anisotropy on the contrast loss signal.

CHAPTER 8

CONCLUSIONS AND OUTLOOK

We began this thesis by asking: what happens to an atom in an electric field? The work described here answered this question with unprecedented precision. We measured the static polarizability of potassium and rubidium with 0.5% uncertainty, and measured polarizability ratios with 0.3% precision. We measured a magic-zero wavelength of potassium – the wavelength at which nothing happens to the atom in the electric field – for the first time. We also developed a new atom beam velocity measurement technique, phase choppers, to enable even more precise polarizability measurements in the future.

Looking forward, we can realistically anticipate improved measurements of static polarizabilities and magic-zero wavelengths in the Cronin lab. The experiments described in this thesis form the foundation of a long program of static and dynamic polarizability measurements in Arizona. At this time, new measurements of cesium, strontium, and ytterbium polarizabilities appear to be of the highest importance. We have already measured the polarizability of Cs with 0.1% precision (Figure 3.9). We have also generated beams of Sr and Ba, as well as beams of metastable He and Ar. Preliminary results using a hall-of-mirrors interaction region have shown a 5-10 times increase in the precision of λ_{zero} measurements.

Have we answered the question of what happens to an atom in an electric field well enough? What will we learn by continuing to improve upon polarizability and magic-zero wavelength measurements?

We believe that there is significant value in pursuing improved measurements of static and dynamic polarizability. Table 1.1 showed the state-of-the-art measurements and calculations of the static polarizabilities of the alkalis. Theory uncertainty is currently about a factor of 2-5 better than the experiment uncertainty for most of these atoms, but theory uncertainty is difficult to estimate and theorists

still routinely request new benchmark measurements of polarizabilities. New experiments are underway to probe parity non-conservation in Cs and Yb, and these experiments will need higher precision measurements of polarizabilities to test the associated atomic structure calculations. Next-generation optical clocks also need higher precision measurements of polarizabilities to accurately correct for blackbody radiation shifts in the clock frequencies.

Future measurements of magic-zero wavelengths will determine difficult-to-calculate matrix elements with high precision, and may provide a sensitive way to probe the core electron contribution to polarizabilities. The many-body physics involved in the calculation of core electron polarizabilities has wide applications in atomic, nuclear, and condensed matter physics.

Polarizability, magic-zero wavelength, and van der Waals potential measurements of small molecules will have applications ranging from testing density functional theory to nanotechnology. We are currently working on implementing an electron ionization detector and mass filter to enable these measurements with molecules and non-alkali atoms.

Finally, it is worthwhile to reflect on the fact that when the Bederson group started its polarizability measurement program in the early 1960s there were no proposals to measure parity non-conservation in atomic systems (although the idea had been considered and dismissed as impractical [7]) nor had atomic clocks been built with such incredible precision that blackbody radiation became an important component in the error budget. However, the Bederson group recognized the wide applications of polarizability measurements and their utility as benchmarks for the rapidly growing field of atomic physics. Similarly, future atomic physics experiments may well benefit from our measurements of polarizabilities today.

APPENDIX A

REPRINT: ABSOLUTE AND RATIO MEASUREMENTS OF THE POLARIZABILITY OF NA, K, AND RB WITH AN ATOM INTERFEROMETER

The following manuscript was published as a peer-reviewed article in Physical Review A. The results of this article are summarized in section 2.1 and Chapter 3 provides supplementary information. The manuscript is reprinted with permission from the American Physical Society. Original reference: W. F. Holmgren, M. C. Revelle, V. P. A. Lonij, and A. D. Cronin, "*Absolute and ratio measurements of the polarizability of Na, K, and Rb with an atom interferometer*", Physical Review A **81**, 053607, (2010). Copyright (2010) by the American Physical Society.

Absolute and ratio measurements of the polarizability of Na, K, and Rb with an atom interferometer

William F. Holmgren, Melissa C. Revelle, Vincent P. A. Lonij, and Alexander D. Cronin[*]

Department of Physics, University of Arizona, Tucson, Arizona 85721, USA

(Received 21 January 2010; published 10 May 2010)

We measured the ground-state electric-dipole polarizability of sodium, potassium, and rubidium using a Mach-Zehnder atom interferometer with an electric-field gradient. We find $\alpha_{\mathrm{Na}} = 24.11(2)_{\mathrm{stat}}(18)_{\mathrm{sys}} \times 10^{-24} \mathrm{cm}^3$, $\alpha_{\mathrm{K}} = 43.06(14)(33)$, and $\alpha_{\mathrm{Rb}} = 47.24(12)(42)$. Since these measurements were all performed in the same apparatus and subject to the same systematic errors, we can present polarizability ratios with 0.3% uncertainty. We find $\alpha_{\mathrm{Rb}}/\alpha_{\mathrm{Na}} = 1.959(5)$, $\alpha_{\mathrm{K}}/\alpha_{\mathrm{Na}} = 1.786(6)$, and $\alpha_{\mathrm{Rb}}/\alpha_{\mathrm{K}} = 1.097(5)$. We combine our ratio measurements with the higher-precision measurement of sodium polarizability by Ekstrom *et al.* [Phys. Rev. A **51**, 3883 (1995)] to find $\alpha_{\mathrm{K}} = 43.06(21)$ and $\alpha_{\mathrm{Rb}} = 47.24(21)$.

PACS number(s): 03.75.Dg, 32.10.Dk

I. INTRODUCTION

Precision measurements of polarizability serve as benchmark tests for methods used to model atoms and molecules [1,2]. Accurate calculations of van der Waals interactions, state lifetimes, branching ratios, indices of refraction, and polarizabilities all rely on sophisticated many-body theories with relativistic corrections, and all of these quantities can be expressed in terms of atomic-dipole matrix elements. Polarizability measurements, such as the ones presented here, are some of the best ways to test these calculations.

Over 35 years ago, Molof *et al.* [3] measured ground-state alkali-metal and metastable noble-gas polarizabilities with an uncertainty of 2% using beam deflection and the E-H gradient-balance technique. More recently, atom interferometers were used to measure the polarizability of lithium [4] and sodium [5] with an uncertainty of 0.7% and 0.35%, respectively. Near-field molecule interferometry was used to measure the polarizability of C_{60} and C_{70} with 6% uncertainty [6], and guided Bose-Einstein-condensate (BEC) interferometry was used to measure the dynamic polarizability of rubidium with 7% uncertainty [7]. A fountain experiment was used to measure the polarizability of cesium with 0.14% uncertainty [8]. The measurements of potassium and rubidium polarizability made by Molof *et al.* remained the most precise until now.

In this article, we present absolute and ratio measurements of the ground-state electric-dipole polarizability of sodium, potassium, and rubidium using a Mach-Zehnder atom interferometer with an electric-field gradient. The uncertainty of each absolute measurement is less than 1.0% and the precision of each ratio measurement is 0.3%. Our interferometer is constructed with nanogratings that diffract all types of atoms and molecules and enable us to measure the polarizabilities of different atomic species in the same apparatus. The systematic errors are nearly the same for the different atomic species and cancel when calculating polarizability ratios. Finally, we combine our polarizability ratios with the absolute measurement of sodium polarizability by Ekstrom *et al.* [5] to provide measurements of potassium and rubidium polarizabilities with 0.5% uncertainty.

———————
*cronin@physics.arizona.edu

A unique feature of this work compared to references [4,5] is that we use an electric-field gradient region rather than a septum electrode. In addition, we use a less collimated beam to increase the flux and reduce the systematic error caused by velocity-selective detection of atoms in the interferometer.

II. APPARATUS

Our apparatus is described in detail elsewhere [9,10]. In brief, we use three 100-nm period nanogratings to diffract a supersonic beam of sodium, potassium, or rubidium atoms and form multiple Mach-Zehnder interferometers (see Fig. 1). An atom diffracted by the first and second gratings may be found with a sinusoidal probability distribution at the plane of the third grating. The third grating acts as a mask of this interference pattern and also diffracts the interferometer output. We measure the flux as a function of grating position to determine the phase and contrast of the fringe pattern. We detect 10^5 atoms/s with a typical contrast of 30% using a hot-wire detector 0.5-m beyond the third grating.

We measure the output of the two interferometers formed by first-order diffraction from the first and second nanogratings (see Fig. 1). Although other interferometers are present, they do not contribute to the measured phase shift because they either are not white-light interferometers, have fringes with a periodicity different than that of the third grating, or are simply not incident upon the detector. The interferometers formed by second-order diffraction from the first grating [11] contribute less than 1% of the detected signal and cause an error in our polarizability measurements of less than 0.01%.

Before the second grating, the path separation in the interferometer is

$$s = \frac{\lambda_{\mathrm{dB}}}{d_{\mathrm{g}}} z = \frac{h}{mvd_{\mathrm{g}}} z \qquad (1)$$

where $\lambda_{\mathrm{dB}} = h/mv$ is the de Broglie wavelength of an atom with mass m and velocity v, d_{g} is the grating period, and z is the propagation distance from the first grating. We adjust the beam velocity for each atomic species such that $s \approx 50 \ \mu\mathrm{m}$ in the interaction region, where the beam width of each diffraction order is approximately 80 μm. We designed the beam parameters to be similar for each atomic species
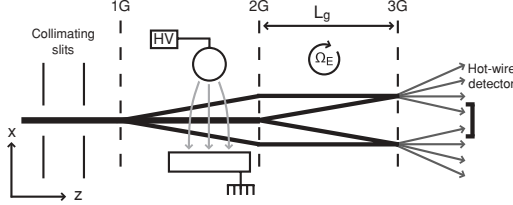
FIG. 1. Nanogratings 1G, 2G, and 3G form multiple Mach-Zehnder interferometers (two are shown). An atom passing through the interaction region acquires a phase ϕ_1, ϕ_0, and ϕ_{-1} along each path. The third grating acts as a mask for the 100-nm period interference fringes and also diffracts the interferometer output. The hot-wire detector is centered on the zeroth-order path. The distance between two gratings is $L_g = 940$ mm. The vertical (transverse) scale is exaggerated 10^4 times. The Earth rotation rate Ω_E modifies the measured phase shift.

in order to minimize systematic errors in measurements of polarizability ratios.

As in previous work [4–6], we place an interaction region between the first and second gratings to induce a differential phase shift in the interferometer. The phase shift is proportional to the atomic polarizability. Unlike references [4,5], we use an electric-field gradient region rather than a septum electrode as an interaction region. We use an electric-field gradient because the septum electrode would require fully separated diffraction orders and this is more difficult with heavier atoms such as potassium and rubidium.

The geometry of our interaction region is depicted in Fig. 2. The interaction region consists of a cylindrical electrode and a grounded plane. This geometry is the familiar "two-wire" configuration [12] rotated by 90° so that the height of the cylinder electrode is perpendicular, rather than parallel, to
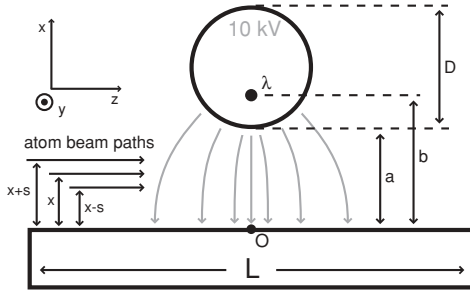
FIG. 2. Cross section of the interaction region (not to scale). The high-voltage electrode of diameter $D = 12.66$ mm is fixed at a distance $a = 1.998$ mm from the ground plane by precision spacers (not shown). The effective line charge λ is located a distance b from the ground plane, as discussed in the text. The ground plane is of length $L = 90$ mm. The high-voltage electrode and ground plane are 50-mm long in the y direction, while the beam height is only 1 mm. The zeroth order beam is a distance x from the ground plane and the $\pm$first-order beams are a distance $x \pm s$ from the ground plane. Electric-field lines are shown in gray. The beam propagates along the z axis. O is the origin for the electric-field calculations.

the beam paths. Our electrode orientation yields a relatively small fringe displacement (200 nm) compared to the standard electrode orientation for Stark deflections (200 μm) [3,13–17], but the sensitivity of atom interferometry allows us to make precise measurements of such small deflections. Two advantages of our electrode orientation are that the phase shift is homogeneous across the height of the atom beam and that there are no fringing fields entering and exiting the interaction region.

We apply a voltage of 0–12 kV to the cylindrical electrode to create the electric-field gradient. Our electrode geometry is easily analyzed via the method of images [18]. The boundary conditions of our geometry, with cylindrical symmetry and an infinite ground plane, correspond exactly to the geometry in which an infinitely long line charge λ is fixed a distance b from the ground plane. The equipotential surfaces are circles of increasing radius centered at an increasing distance from the ground plane. We identify one of these equipotential surfaces as our electrode at a voltage V with radius R and located a distance a from the ground plane to determine its corresponding effective line charge λ and its position b:

$$\lambda = 2\pi\epsilon_0 V \ln^{-1}\left(\frac{a+R+b}{a+R-b}\right), \quad (2)$$

$$b = a\sqrt{1+2R/a}. \quad (3)$$

The resulting electric field is given by

$$\boldsymbol{E}_{(x,z)} = \frac{\lambda}{\pi\epsilon_0}\left\{\left[\frac{x-b}{(x-b)^2+z^2} - \frac{x+b}{(x+b)^2+z^2}\right]\hat{\boldsymbol{x}} + \left[\frac{z}{(x-b)^2+z^2} - \frac{z}{(x+b)^2+z^2}\right]\hat{\boldsymbol{z}}\right\}. \quad (4)$$

The potential energy of an atom in an electric field is given by the Stark shift $U_{\text{Stark}} = -\frac{1}{2}\alpha E^2$. We use the WKB approximation to find the phase $\phi_\alpha(x,v)$ acquired by an atom along a path a distance x from the ground plane with velocity v and polarizability α:

$$\phi_\alpha(x,v) = \frac{\alpha}{2\hbar v}\int_{-\infty}^{\infty} E_{(x,z)}^2 dz. \quad (5)$$

For our atom beam $U_{\text{Stark}} \approx 10^{-7}$eV and $U_{\text{kinetic}} \approx 0.1$eV, so the WKB approximation is valid. The integral of E^2 along the path of the atom may be performed using complex analysis and yields an acquired phase of

$$\phi_\alpha(x,v) = \frac{\lambda^2\alpha}{\pi\epsilon_0^2\hbar v}\left(\frac{b}{b^2-x^2}\right). \quad (6)$$

We induce a polarizability phase ϕ_α of up to 2500 rad along one path.

We will now discuss how the phase and contrast of the measured fringe pattern depends on the polarizability phase $\phi_\alpha(x,v)$. First, we define the phase difference between the paths of the two detected interferometers:

$$\begin{aligned}\phi_{\alpha,1}(x,v) &= \phi_\alpha(x+s,v) - \phi_\alpha(x,v),\\ \phi_{\alpha,-1}(x,v) &= \phi_\alpha(x,v) - \phi_\alpha(x-s,v).\end{aligned} \quad (7)$$

We studied phase differences $\phi_{\alpha,1}$ of up to 18 rad. Next, we perform an incoherent sum of the fringe patterns formed by atoms

of multiple velocities traversing multiple interferometers. The resulting fringe pattern is described by

$$C_{\text{sum}}(x)e^{i\phi_{\text{sum}}(x)} = C_0 e^{i\phi_0} \sum_{j=-1,1} P_j \int_0^\infty P(v)e^{i\phi_{\alpha,j}(x,v)}dv, \tag{8}$$

where C_{sum} is the real-valued contrast of the fringe pattern, ϕ_{sum} is the phase of the fringe pattern, C_0 and ϕ_0 are the initial contrast and phase of the interferometer, j denotes the interferometer number (upper or lower diamond in Fig. 1), $P_j = 0.5$ is the probability of an atom being found in interferometer j, and $P(v)$ is the velocity distribution of the beam. In our experiment, the phase shift ϕ_{sum} is reduced by as much as 4% by performing the sum described in Eq. (8) compared to a simple weighted average of phases, and the contrast is reduced by more than 50%.

The Sagnac phase must also be accounted for in our experiment and modifies Eq. (8) [19,20]. Because the Sagnac phase is dispersive, ignoring it would lead to an error in polarizability of up to 1%. The Sagnac phase in our interferometer is given by

$$\phi_{\text{Sag}}(v) = \frac{4\pi L_g^2 \Omega}{d_g v}, \tag{9}$$

where L_g is the distance between adjacent nanogratings and Ω is the rotation rate of the Earth projected into the plane of the interferometer. At our latitude, the Sagnac phase is as much as 4.8 rad for our rubidium beam. The reference phase ϕ_{ref} and contrast C_{ref} of the interferometer are determined by the Sagnac phase in the absence of an electric field:

$$C_{\text{ref}}e^{i\phi_{\text{ref}}} = C_0 e^{i\phi_0} \sum_{j=-1,1} P_j \int_0^\infty P(v)e^{i\phi_{\text{Sag}}(v)}dv. \tag{10}$$

We find the total phase and contrast of the interferometer in the presence of an electric field by adding the Sagnac phase to the polarizability phase shift before conducting the incoherent sum shown in Eq. (8). This procedure yields

$$\begin{aligned}C_{\text{total}}(x)&e^{i\phi_{\text{total}}(x)}\\&= C_0 e^{i\phi_0} \sum_{j=-1,1} P_j \int_0^\infty P(v)e^{i[\phi_{\alpha,j}(x,v)+\phi_{\text{Sag}}(v)]}dv. \end{aligned}\tag{11}$$

Finally, the measured phase shift and relative contrast are

$$\phi_{\text{measured}}(x) = \phi_{\text{total}}(x) - \phi_{\text{ref}}, \tag{12}$$

$$C_{\text{measured}}(x) = C_{\text{total}}(x)/C_{\text{ref}}. \tag{13}$$

As an alternative point of view, we may describe the measured phase shift in terms of a classical electrostatic force on the individual atomic dipoles instead of the quantum-mechanical phases acquired by an atom in the electric field. In the classical-mechanics picture, a neutral atom in an electric field experiences a force $F = -\nabla U_{\text{Stark}} = \alpha E\nabla E$. The deflection of the interferometer paths will cause the same displacement of the observed fringes as the phase-shift analysis discussed above.

III. VELOCITY MEASUREMENT

The velocity determines both the amount of time an atom interacts with the electric field and the spatial separation s of the paths inside the electric-field gradient. Therefore, an accurate determination of the beam velocity and the velocity distribution is essential for a precise polarizability measurement.

We determine the velocity of the atom beam by analyzing the far-field diffraction pattern from the first grating. The velocity distribution of the beam is modeled by

$$P(v)dv = Av^3 \exp\left[-(v-v_0)^2/\left(2\sigma_v^2\right)\right]dv, \tag{14}$$

where v is the velocity, v_0 is the flow velocity, σ_v describes the velocity distribution, and A is a normalization factor [21]. In the limit of a supersonic beam, $v_0/\sigma_v \gg 1$, the normalization factor can be written as $A = [\sqrt{2\pi}v_0\sigma_v(v_0^2 + 3\sigma_v^2)]^{-1}$. The location of the nth diffraction order at the detector plane is given by

$$x_n = \frac{\lambda_{\text{dB}}}{d_g}nz_{\text{det}} = \frac{hn}{mvd_g}z_{\text{det}}, \tag{15}$$

where the propagation distance z is equal to the distance from the first grating to the detector, z_{det}. We use $m = m_{\text{avg}}$, which is the average mass of the atomic species, rather than calculating and adding the diffraction patterns for each isotope. A reanalysis of a subset of our data shows that this approximation yields a small difference in velocity ($<0.02\%$) and polarizability ($<0.05\%$) when isotopes are taken into account. Next, we rearrange Eq. (15) to find

$$v(x_n) = \frac{z_{\text{det}}hn}{md_g x_n} \tag{16}$$

and use this to transform $P(v)dv$ to $P(x)dx$. Finally, we sum over all diffraction orders, each weighted by c_n, and add the zeroth-order peak to obtain the diffraction pattern for an infinitesimally thin beam and detector:

$$\begin{aligned}P(x)dx = &\left\{c_0\delta(x-0) + \sum_{n\neq0} c_n A\left(\frac{z_{\text{det}}hn}{md_g}\right)^4 x^5\right.\\&\left.\times \exp\left[-\left(\frac{z_{\text{det}}hn}{md_g x}-v_0\right)^2\Big/\left(2\sigma_v^2\right)\right]\right\}dx. \end{aligned}\tag{17}$$

The observed diffraction pattern (see Fig. 3) is a convolution of the spatial probability distribution given by Eq. (17) with the collimated beam and detector shapes. Two narrow collimating slits of width 20 and 10 μm separated by 890 mm determine the beam shape. We model the detector wire as a square aperture with width 70 μm. We fit the observed diffraction pattern to the convolution described above to find the flow velocity v_0. With four diffraction scans, we can determine v_0 with a statistical precision of 0.1%.

The diffraction orders are sufficiently close together, the beam is sufficiently broad, and the detector is sufficiently thick that we cannot use diffraction data alone to determine the velocity distribution σ_v with enough precision for the polarizability measurements. Instead, as discussed later, we find the velocity distribution parameter σ_v from
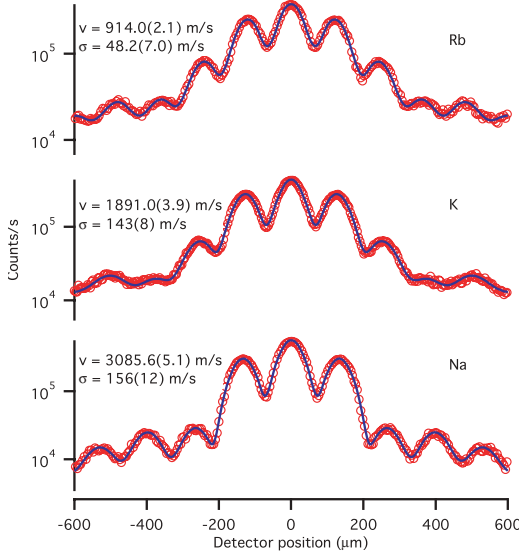
FIG. 3. (Color online) Diffraction of Rb, K, and Na atoms from the same nanograting. Best-fit flow velocity v_0 and velocity distribution σ_v with statistical errors are shown. As discussed in the text, the velocity distribution is found from contrast-loss measurements.

FIG. 4. (Color online) Phase shift and relative contrast vs. electrode position x. The best-fit polarizability and the statistical error for one data set are shown. We only fit the phase shift measurements with relative contrast greater than 75%. Residuals for the fit data points (circles) are shown with error bars. For reference, residuals for the unfit data points (filled diamonds) are also shown. The contrast loss determines v_0/σ_v.

the contrast loss measurements. We then fix σ_v when fitting the diffraction patterns to find the final flow velocity v_0.

IV. PHASE AND CONTRAST MEASUREMENT

After recording several diffraction scans to measure the flow velocity, we center the detector on the zeroth-order diffraction peak, replace the narrow collimating slits with wider ones (35 and 45 μm), and insert the second and third gratings into the beamline to form the interferometer. We use a wider beam for our interferometer than Ekstrom *et al.* [5] for two reasons. First, wide collimating slits allow more flux to reach the detector. Second, wide slits minimize the velocity-selective detection of interference fringes caused by the dispersive nature of diffraction. We calculate that the flow velocity of the atoms detected from the interferometers when the detector wire is centered on the beam is about 0.25% faster than the flow velocity of the entire beam. We use the adjusted flow velocity when determining the polarizability, yielding a 0.5% correction to the polarizability. The correction to the velocity distribution parameter σ_v is negligible. If we had used small slits with the detector on the centerline, this correction and the uncertainty in this correction would have been three times larger.

Next, we calibrate the position of the interaction region by eclipsing the beam with the cylindrical electrode and then moving the interaction region out of the beam path as we record the average flux through the interferometer and the position of the interaction region. We use the position at which the flux is 50% of the maximum to locate the center of the beam a distance

a from the ground plane. We then move the interaction region across the beam in steps of 100 μm and measure the phase shift [Eq. (12)] and contrast loss [Eq. (13)] at each position. Figure 4 shows the measured phase shift and contrast loss for a typical data set.

We determine the flow velocity, velocity distribution, and polarizability from the diffraction, contrast loss, and phase shift data, respectively. In Sec. III, we discussed how we find the flow velocity v_0. In Sec. II, we discussed how the contrast of the measured fringe pattern is reduced by performing an incoherent sum of the fringes formed by atoms of multiple velocities. We fit the contrast loss data to determine v_0/σ_v with an uncertainty of 10%. The primary source of error in this measurement of σ_v comes from vibration-induced fluctuations in the reference contrast. We then refit the diffraction data, holding σ_v fixed, to find the best-fit flow velocity v_0. This procedure yields a small correction to v_0 of less than 0.2%. Finally, we use v_0 and σ_v as inputs to the polarizability fit of the phase data. We exclude data points in which the relative contrast is less than 75% to minimize the uncertainty in the polarizability due to uncertainty in σ_v.

After fitting all the data, we apply small corrections to the polarizability due to beam thickness and isotope ratios. To account for beam thickness, we modify Eq. (11) to include an integral over the beam width. The correction to the polarizability due to beam thickness is $+0.04(2)\%$ for each atomic species. To account for isotope ratios we modify Eqs. (11) and (17) to include weighted sums over isotopes.
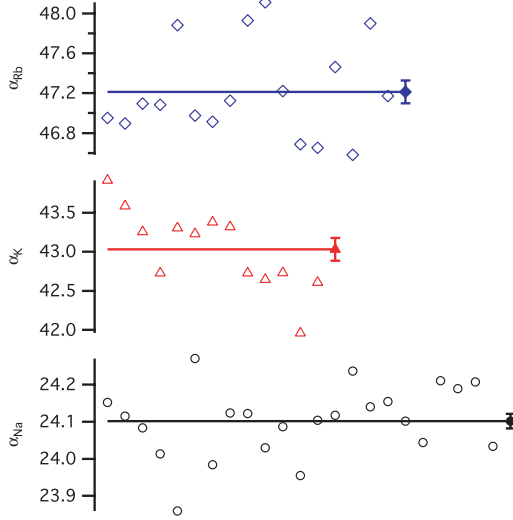
FIG. 5. (Color online) Multiple measurements of the polariz-ability of sodium (circles), potassium (triangles), and rubidium (diamonds). The mean polarizabilities are denoted by filled markers and lines. The error bars represent the standard error of the mean. Units are 10^{-24} cm^3. Final results are shown in Table I.

The correction to the polarizability from taking into account the isotope ratios is +0.04% for α_K and +0.02% for α_{Rb}.

The result of each data set is shown in Fig. 5. Each point on the plot represents one hour of data. We report the mean polarizability from all of our data in Table I. The reported statistical error is the standard error of the mean and is dominated by the reproducibility of the experiment rather than the statistical phase error of a typical data set. The systematic errors are discussed later.

Since we performed all measurements in the same apparatus under similar beam conditions and without changing any parameters that contribute to systematic error in the polar-izability, we can report polarizability ratios with uncertainties dominated by the statistical precision of our measurements. We show our measured polarizability ratios in Table II. Figure 6 shows a summary of measurements [3,13] and calculations [2,22–33] of the polarizability ratios of sodium, potassium, and rubidium, including this work. We added the reported uncertainties for each atom in quadrature to calculate the uncertainty in polarizability ratios for previous work [3,13].

TABLE I. Measured absolute and recommended atomic polar-izabilities in units of 10^{-24} cm^3. Our recommended polarizability values are based on our ratio measurements (see Table II) combined with the sodium polarizability measurement from reference [5].

	α_{abs} (stat.)(sys.)	α_{rec}(tot.)
Na	24.11(2)(18)	24.11(8)
K	43.06(14)(33)	43.06(21)
Rb	47.24(12)(42)	47.24(21)

TABLE II. Measured atomic polarizability ratios with statistical uncertainties. Also included are several polarizability ratios from *ab initio* and semi-empirical calculations. See Fig. 6 for more previous calculations and measurements of polarizability ratios.

Atoms	α_{ratio} (stat. unc.)			
	This work	Ref. [2]	Ref. [30]	Ref. [31]
Rb:Na	1.959(5)	1.959(5)	1.946	1.939
K:Na	1.786(6)	1.785(6)	1.779	1.781
Rb:K	1.097(5)	1.098(5)	1.094	1.089

If the reported uncertainties have systematic errors that would have canceled in ratio measurements, then this calculation will lead to an overestimate of the ratio uncertainties.

We calculate our recommended measurements of potassium and rubidium polarizability by combining our polarizability-ratio measurements with the sodium-polarizability measure-ment by Ekstrom *et al.* [5]. To calculate the total uncertainty of the recommended polarizabilities of potassium and rubidium, we add the total uncertainty of the Ekstrom *et al.* sodium measurement in quadrature with the statistical uncertainty of our appropriate polarizability ratio. Our recommended polarizability values and their total uncertainties are shown in Table I. Given the 0.8% uncertainty of our direct measurement of α_{Na}, the agreement between our measurement and that of Ekstrom *et al.* at the level of 0.04% is coincidental.

Table III shows a summary of the error budget. Most of the highly significant parameters in the error budget are related to the flow velocity v_0 or velocity distribution parameter σ_v. The
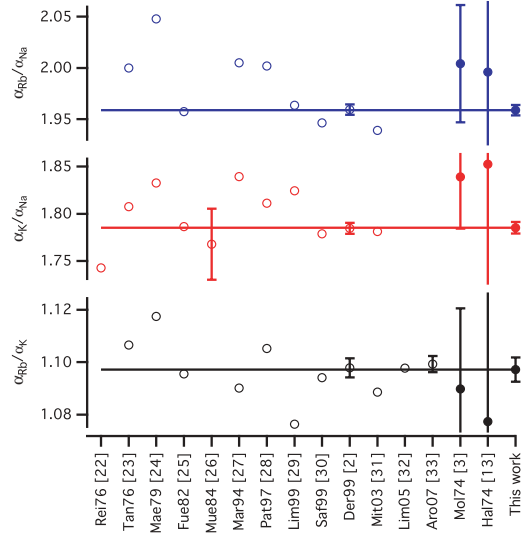
FIG. 6. (Color online) Previously calculated (unfilled) and mea-sured (filled) alkali-metal polarizability ratios. References are de-noted by the abbreviated name of the first author, the publication year, and the reference number. Calculations in references [2,33] incorporate state-lifetime measurements.

TABLE III. Systematic error budget for a single-sodium measurement. The potassium and rubidium systematic error budgets are similar.

| Source	Value (unc.)	Error in α (%)
First grating (1G)-detector distance z_{det}	2372.4(5.1) mm	0.43
Velocity (beam-shape model)	3023(4) m/s	0.25
Detector displacement x_1	135.00(3) μm	0.05
Detector translation $\parallel$	50 mrad	0.30
Velocity distribution σ_v	149(14) m/s	0.20
δ_v/v of interfering atoms	0.20(5)%	0.10
Spacer thickness a	1.998(2) mm	0.20
Electrode diameter $2R$	12.663(25) mm	0.10
Electrode voltage V	10670(16) V	0.30
Electrode orientation (x,y,z)	(20,0.1,20) mrad	0.05
1G-int. region distance z_{int}	802.6(2.0) mm	0.25
Grating period d_{g}	100.0(1) nm	0.10
Molecule fraction	0(1)%	0.10
Grating tilt and g	0.0(1) mrad	0.01
Beam thickness (phase avg.)	80(20) μm	0.02
Total Systematic Error		0.80

most significant parameter in the error budget is the distance from the first grating to the detector, z_{det}, due to its effect on our measurement of v_0. The details of the beam shape modify the best-fit flow velocity as well. We measure the displacement of our detector translation stage using a Heidenhain MT-2571 length gauge with a linear encoder and fractional uncertainty of 0.02%. If the detector translation along the x axis is not perpendicular to the beam path along the z axis, then we would also report an incorrect velocity. We previously discussed how the velocity-selective detection of interfering atoms modifies v_0 and adds uncertainty in the polarizability. The effect of the velocity distribution on the measured phase becomes larger as the phase shift increases and the contrast decreases. Therefore, to minimize the uncertainty due to the velocity distribution, we ignore phase data points for which the relative contrast is less than 75%. This procedure yields an uncertainty of 0.20% in the polarizability for a 10% uncertainty in σ_v. Uncertainty in the distance from the first grating to the interaction region, z_{int}, causes uncertainty in the diffracted path separation s in the interaction region. Uncertainty in the electrode spacing a, radius R, and applied voltage V causes uncertainty in the strength of the electric field. Uncertainty in the electrode orientation about the x, y, and z axes yields a small uncertainty in the polarizability, as well.

The possibility of a small fraction of molecules in the beam contributes an additional source of error. The diffraction scans

for the conditions under which we run the interferometer do not have sufficient resolution to determine the molecule fraction of the beam. By reducing the velocity of the beam and thus increasing the diffraction angle, we found that molecules contribute less than 1% of the flux. To calculate the corresponding uncertainty in our polarizability measurements we include a sum over two additional molecule interferometers in Eq. (11). We use the molecular polarizabilities measured by Tarnovsky *et al.* [14] in our calculations to find that the uncertainty in atomic polarizabilities due to the presence of molecules is less than 0.10%.

An additional source of error comes from the possible tilt of the entire interferometer board with respect to gravity. If the interferometer is tilted with respect to gravity by an angle θ, a dispersive phase shift of

$$\phi_{\text{grav}}(v) = \frac{2\pi L_{\text{g}}^2}{d_{\text{g}} v^2} g \sin \theta \qquad (18)$$

will result. This phase shift must be added to the total phase shift and the reference phase in the same way as the Sagnac phase. We estimate that $\theta < 0.1$ mrad and that the corresponding uncertainty in the polarizability is less than 0.01%.

V. CONCLUSIONS AND OUTLOOK

We measured both the absolute and relative polarizabilities of sodium, potassium, and rubidium using an atom interferometer with an electric-field gradient. Furthermore, we used our ratio measurements and the more-precise Ekstrom *et al.* measurement of sodium polarizability [5] to report higher-precision measurements of potassium and rubidium polarizability. These measurements provide benchmark tests of atomic theory calculations. Our ground-state polarizability measurements may be combined with transition Stark-shift measurements [34–37] to yield improved knowledge of excited-state polarizabilities and additional dipole matrix elements [33,38].

We are upgrading our apparatus to produce and detect beams of alkaline-earth-metal atoms. We are investigating new interaction region geometries and new ways to measure the flow velocity and velocity distribution of the atoms detected in the interferometer. We are also using diffraction from a nanograting to study ratios of van der Waals potentials for sodium, potassium, and rubidium [39].

[1] H. Gould and T. M. Miller, Adv. At., Mol., Opt. Phys. **51**, 343 (2005).

[2] A. Derevianko, W. R. Johnson, M. S. Safronova, and J. F. Babb, Phys. Rev. Lett. **82**, 3589 (1999).

[3] R. W. Molof, H. L. Schwartz, T. M. Miller, and B. Bederson, Phys. Rev. A **10**, 1131 (1974).

[4] A. Miffre, M. Jacquey, M. Büchner, G. Trénec, and J. Vigué, Phys. Rev. A **73**, 011603(R) (2006).

[5] C. R. Ekstrom, J. Schmiedmayer, M. S. Chapman, T. D. Hammond, and D. E. Pritchard, Phys. Rev. A **51**, 3883 (1995).

[6] M. Berninger, A. Stefanov, S. Deachapunya, and M. Arndt, Phys. Rev. A **76**, 013607 (2007).

[7] B. Deissler, K. J. Hughes, J. H. T. Burke, and C. A. Sackett, Phys. Rev. A **77**, 031604(R) (2008).

[8] J. M. Amini and H. Gould, Phys. Rev. Lett. **91**, 153001 (2003).

[9] A. D. Cronin, J. Schmiedmayer, and D. E. Pritchard, Rev. Mod. Phys. **81**, 1051 (2009).

[10] *Atom Interferometry*, edited by P. Berman (Academic Press, San Diego, 1997).

[11] J. D. Perreault and A. D. Cronin, Phys. Rev. A **73**, 033610 (2006).

[12] N. F. Ramsey, *Molecular Beams* (Oxford University Press, New York, 1956).

[13] W. D. Hall and J. C. Zorn, Phys. Rev. A **10**, 1141 (1974).

[14] V. Tarnovsky, M. Bunimovicz, L. Vušković, B. Stumpf, and B. Bederson, J. Chem. Phys. **98**, 3894 (1993).

[15] G. Tikhonov, V. Kasperovich, K. Wong, and V. V. Kresin, Phys. Rev. A **64**, 063202 (2001).

[16] S. Schäfer, M. Mehring, R. Schäfer, and P. Schwerdtfeger, Phys. Rev. A **76**, 052515 (2007).

[17] S. Schäfer, S. Heiles, J. A. Becker, and R. Schäfer, J. Chem. Phys. **129**, 044304 (2008).

[18] R. K. Wangsness, *Electromagnetic Fields*, 2nd ed. (John Wiley & Sons, New York, 1986).

[19] A. Lenef, T. D. Hammond, E. T. Smith, M. S. Chapman, R. A. Rubenstein, and D. E. Pritchard, Phys. Rev. Lett. **78**, 760 (1997).

[20] M. Jacquey, A. Miffre, G. Trénec, M. Büchner, J. Vigué, and A. Cronin, Phys. Rev. A **78**, 013638 (2008).

[21] H. Haberland, U. Buck, and M. Tolle, Rev. Sci. Instrum. **56**, 1712 (1985).

[22] E.-A. Reinsch and W. Meyer, Phys. Rev. A **14**, 915 (1976).

[23] K. T. Tang, J. M. Norbeck, and P. R. Certain, J. Chem. Phys. **64**, 3063 (1976).

[24] F. Maeder and W. Kutzelnigg, Chem. Phys. **42**, 95 (1979).

[25] P. Fuentealba, J. Phys. B **15**, L555 (1982).

[26] W. Müller, J. Flesch, and W. Meyer, J. Chem. Phys. **80**, 3297 (1984).

[27] M. Marinescu, H. R. Sadeghpour, and A. Dalgarno, Phys. Rev. A **49**, 5103 (1994).

[28] S. H. Patil and K. T. Tang, J. Chem. Phys. **106**, 2298 (1997).

[29] I. S. Lim, M. Pernpointner, M. Seth, J. K. Laerdahl, P. Schwerdtfeger, P. Neogrady, and M. Urban, Phys. Rev. A **60**, 2822 (1999).

[30] M. S. Safronova, W. R. Johnson, and A. Derevianko, Phys. Rev. A **60**, 4476 (1999).

[31] J. Mitroy and M. W. J. Bromley, Phys. Rev. A **68**, 052714 (2003).

[32] I. S. Lim, P. Schwerdtfeger, B. Metz, and H. Stoll, J. Chem. Phys. **122**, 104103 (2005).

[33] B. Arora, M. S. Safronova, and C. W. Clark, Phys. Rev. A **76**, 052516 (2007).

[34] K. E. Miller, D. Krause, and L. R. Hunter, Phys. Rev. A **49**, 5128 (1994).

[35] C. Krenn, W. Scherf, O. Khait, M. Musso, and L. Windholz, Z. Phys. D **41**, 229 (1997).

[36] M. Kawamura, W.-G. Jin, N. Takahashi, and T. Minowa, J. Phys. Soc. Jpn. **78**, 034301 (2009).

[37] M. Kawamura, W.-G. Jin, N. Takahashi, and T. Minowa, J. Phys. Soc. Jpn. **78**, 124301 (2009).

[38] C. Zhu, A. Dalgarno, S. G. Porsev, and A. Derevianko, Phys. Rev. A **70**, 032722 (2004).

[39] V. P. A. Lonij, C. E. Klauss, W. F. Holmgren, and A. D. Cronin (to be published) (2010).

APPENDIX B

REPRINT: ATOM BEAM VELOCITY MEASUREMENTS USING PHASE CHOPPERS

The following manuscript was published as a peer-reviewed article in the New Journal of Physics. The results of this article are discussed in section 2.2 and Chapter 4 provides supplementary information. The manuscript is reprinted with permission from IOP Publishing Ltd. Original reference: W. F. Holmgren, I. Hromada, C. E. Klauss, and A.D. Cronin, "*Atom beam velocity measurements using phase choppers*", New Journal of Physics **13**, 115007, (2011). Copyright (2011) by IOP Publishing Ltd.

New Journal of Physics
The open–access journal for physics

Atom beam velocity measurements using phase choppers

William F Holmgren, Ivan Hromada, Catherine E Klauss and Alexander D Cronin

Department of Physics, University of Arizona, Tucson, AZ, USA
E-mail: cronin@physics.arizona.edu

Abstract. We describe a new method to measure atom beam velocity in an atom interferometer using phase choppers. Phase choppers are analogous to mechanical chopping discs, but rather than being transmitted or blocked by mechanical choppers, an atom receives different differential phase shifts (e.g. zero or π radians) from phase choppers. Phase choppers yield 0.1% uncertainty measurements of beam velocity in our interferometer with 20 min of data and enable new measurements of polarizability with unprecedented precision.

Contents

1. Introduction

More accurate methods for measuring atomic velocity are needed to support high-precision atom interferometry experiments. For example, atom beam velocity is the leading source of uncertainty in several measurements of atomic and molecular polarizabilities [1–4]. This is

because phase shifts to atomic de Broglie waves depend on the time of flight for atoms propagating through an interaction region. Additionally, improved measurements of beam velocity can increase the accuracy of space-domain matter-wave inertial sensors [5, 6]. In this paper, we describe a novel and highly accurate method to measure the flow velocity and velocity distribution of atoms in an atom beam interferometer.

Many techniques exist to measure atom beam velocities, but few provide the 0.1% accuracy we demonstrate here using a new method. For comparison and background, we review a handful of velocity measurement techniques. First, two spinning mechanical choppers (slotted disks) separated by a distance L and blocking the beam at frequency f can transmit atoms with velocity $v = nLf$, where n is an integer. Molecular beam velocity has been measured using this technique with 0.2% uncertainty [7, 8], but this requires moving parts inside a vacuum system and can cause unacceptable vibrations. Another approach uses the small gravitational free fall of an atom beam through separated apertures at different heights to define the velocity of transmitted atoms with 1% uncertainty [9]. Doppler shifts of an atomic transition observed with a resonant laser enable measurements of velocity with 0.8% uncertainty [3]. Similar uncertainty (0.8%) was obtained with Bragg diffraction from standing waves of light by analyzing rocking curves [3]. Atom diffraction using a nanograting has been used by our group to measure beam velocity with 0.3% uncertainty [1]. Finally, pulsed beams and time-resolved detection were recently used to achieve 0.03% uncertainty velocity measurements of pulsed metastable helium beams [10], but this technique is less applicable to continuous beams of ground state atoms.

Our new velocity measurement technique uses *phase choppers* to measure the velocity of atoms in an interferometer. Phase choppers do not block any atoms, do not require resolved diffraction, have no moving parts, work for continuous or pulsed beams, and work well for many types of atoms and molecules. Phase choppers are similar to the phase shifters described in [11] and their utility for measuring beam velocity was first proposed in [12]. This paper develops a significantly more thorough analysis of atom beam velocity measurements using phase choppers and we demonstrate velocity measurements with 0.1% uncertainty. We tested phase choppers with supersonic beams of Li, Na, K and Cs, and we use the velocity measurements as inputs to atomic polarizability measurements. To demonstrate the utility of phase choppers for precision measurements, we present consistent measurements of Cs polarizability with 0.1% precision using beams that had different velocities (spanning 925–1680 m s^{-1}).

2. Phase choppers theory

The principle behind phase choppers is similar to that behind mechanical choppers. An atom with velocity v will travel a distance L from the first chopper to the second chopper in a time $\tau = L/v$, corresponding to a fundamental chopping frequency $f_0 = v/L$. Mechanical choppers simply block or transmit atoms, leading to a maximum in the transmitted flux when the chopping frequency is any integer multiple of f_0. In the method we present in this paper, phase choppers are switched on and off by a function generator to periodically apply phase shifts to atomic de Broglie waves in an interferometer. We will explain how this leads to a maximum in the interferometer contrast, instead of the flux, when the chopping frequency satisfies $f = nf_0$. Additionally, the ability to control wavefunction phase, rather than amplitude, allows atoms to contribute to the interference fringes in unique ways and provides new measurement possibilities, as we describe next.

To explain how phase choppers enable velocity measurements, we will describe how the atom interference pattern changes when the phase choppers are switched on and off at several
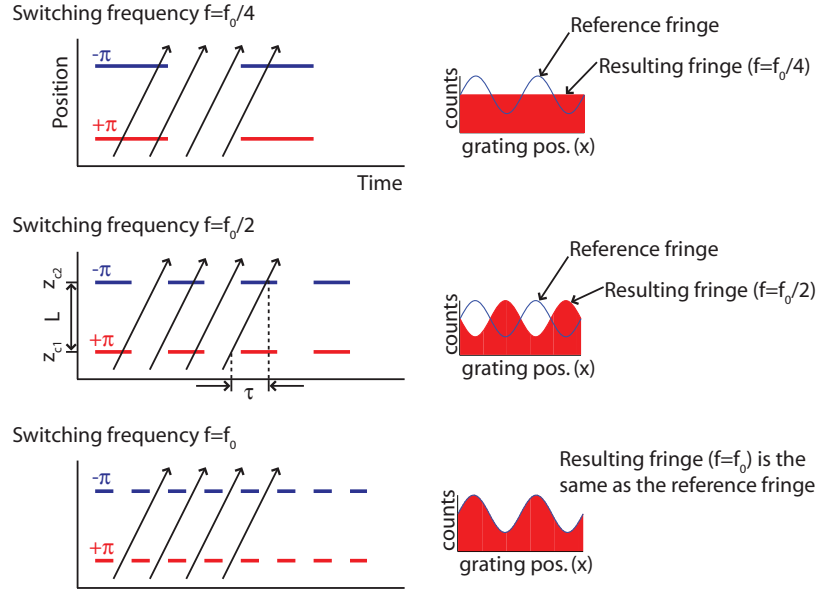
Figure 1. Atoms with different starting times will acquire 0, $+\pi$ (red) or $-\pi$ (blue) phase shifts as they pass through choppers 1 and 2, depending on their velocity v and the chopping frequency f. The time it takes an atom with velocity v to travel the distance L between the choppers is τ and $f_0 = 1/\tau$. We measure the average of the sinusoidal probability distributions formed by each atom interfering with itself, shown at the right. The reference interference pattern with the choppers off is shown in blue and the resulting interference patterns with the choppers on are shown in red.

particular frequencies. Before turning on the phase choppers, the atom interference pattern is given by $\langle N \rangle (1 + C_0 \sin(kx + \phi_0))$, where $\langle N \rangle$ is the average flux, C_0 is the reference contrast and ϕ_0 is the reference phase. This interference pattern represents a sum of the sinusoidal probability distributions of each detected atom (see [13, 14] for additional information). Depending on its start time and velocity and the chopping frequency, an atom will pass through the choppers in one of four possible pairs of conditions (off–off, on–off, off–on or on–on) and produce a probability distribution phase-shifted by an amount equal to the sum of the differential phase shifts applied by each phase chopper. For clarity, we specify the differential phase shift from chopper 1 to be π, the differential phase shift from chopper 2 to be $-\pi$, and the duty cycle to be 50%; however, we stress that phase choppers still enable velocity measurements when using other phase shifts and duty cycles. We now describe what happens to the interference pattern created by atoms with a single velocity v when the choppers are switched at four particular frequencies (see figure 1):

- $f \ll f_0$. Atoms experience the off–off (0 net differential phase shift) or on–on (0 net differential phase shift) pairs of conditions with equal likelihood, and all atoms emerge with 0 net phase shift. The contrast and phase of the detected ensemble remain unchanged.

4

IOP Institute of Physics ⏀ DEUTSCHE PHYSIKALISCHE GESELLSCHAFT

- $f = f_0/4$. Atoms experience each of the four possible pairs of conditions, off–off (0), on–off (π), off–on ($-\pi$) and on–on (0), with equal likelihood. Therefore, half of the ensemble will acquire a 0 net differential phase shift, and half will acquire a π net differential phase shift. The ensemble contrast is 0 and phase is indeterminate. Contrast minima repeat at frequencies $f = (2n+1)f_0/4$, where n is an integer.

- $f = f_0/2$. Atoms experience on–off (π) and off–on ($-\pi$) pairs of conditions with equal likelihood. The ensemble contrast remains unchanged, but the phase shifts by π (modulo 2π). Contrast revivals with π phase shifts repeat at frequencies $f = (2n+1)f_0/2$.

- $f = f_0$. Once again, all atoms experience the off–off (0) or on–on (0) states. The ensemble contrast and phase remain unchanged. Contrast revivals with no phase shift repeat at frequencies $f = nf_0$.

These simple cases show how by finding the value of f_0 one can find the velocity of an atom beam through the relation $v = Lf_0$. The contrast revivals and minima that occur at large n provide a way of leveraging small changes in velocity into large changes in revival/minima frequency. In practice, we find the velocity of our atom beam by measuring the contrast at many frequencies and fitting the contrast data to a model discussed below. Figure 3 shows fitted data from a typical chopper frequency scan using a more rigorous model that we develop next. The major corrections to the simple model include methods to account for velocity distribution, velocity-dependent phase shifts from the choppers, application of non-π average phase shifts, and velocity-dependent phase shifts due to the Sagnac effect.

The contrast and phase of the measured interference pattern are given by an average of the fringe patterns formed by atoms with different start times, t, and velocities, v, weighted by the velocity probability distribution $P(v)$:

$$C(f)\mathrm{e}^{\mathrm{i}\phi(f)} = C_0\mathrm{e}^{\mathrm{i}\phi_0} f \int_{t=0}^{1/f} \int_{v=0}^{\infty} P(v)\mathrm{e}^{\mathrm{i}(\phi_1(v,t)+\phi_2(v,t+L/v))} \, \mathrm{d}t \, \mathrm{d}v, \tag{1}$$

where $C(f)$ and $\phi(f)$ are the contrast and phase of the measured fringe pattern, and $\phi_1(v,t)$ and $\phi_2(v,t)$ are the differential phase shifts applied by choppers 1 and 2.

The nonzero width of the velocity distribution of the atom beam modifies the chopper revivals in two ways. Firstly, different velocity classes correspond to different fundamental frequencies f_0 and this causes a decay of the contrast revival envelope. Secondly, the differential phase shift acquired by an atom passing through a chopper is velocity dependent, and therefore it is impossible to apply the same differential phase shift to all atoms. This phase dispersion decreases the contrast at $f = (2n+1)f_0/2$ revivals and increases the contrast at $f = nf_0$ revivals.

We model the velocity distribution of the supersonic atom beam used in our interferometer by

$$P(v, v_0, r)\mathrm{d}v = Av^3\mathrm{e}^{-\frac{r^2}{2}(v/v_0-1)^2} \, \mathrm{d}v, \tag{2}$$

where v is the velocity, v_0 is the flow velocity, r describes the sharpness of the velocity distribution and A is a normalization factor [7]. For sharp velocity distributions, $r \gg 1$, the normalization factor can be written as $A = (\sqrt{2\pi}v_0^4(r^{-1}+3r^{-3}))^{-1}$. In the next section, we describe how we build and operate the phase choppers and fit the measured contrast versus chopping frequency to find v_0 and r (see figure 3).

IOP Institute of Physics ⬤ DEUTSCHE PHYSIKALISCHE GESELLSCHAFT
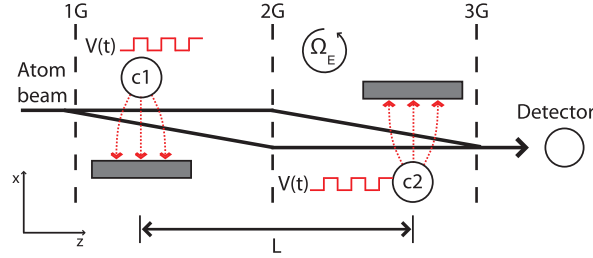
Figure 2. Nanogratings 1G, 2G and 3G form a Mach–Zehnder interferometer. Two phase choppers (c1 and c2) are placed a distance $L = 1270.68(25)$ mm apart. A voltage $V(t)$ applied across the choppers creates an electric field (dashed lines). Atoms with velocity v passing through choppers 1 and 2 acquire net differential phase shifts $\phi_1(t) + \phi_2(t + L/v)$. The Earth rotation rate Ω_E modifies the measured contrast and phase via the Sagnac effect, especially for slow beams. A hot-wire detector counts the atoms. Diagram not to scale.

3. Experimental design

Before describing in detail how the phase choppers enable velocity measurements, we briefly review our atom interferometer and the construction of the phase choppers. We use three 100 nm period nanogratings to diffract a supersonic beam of atoms and create a Mach–Zehnder interferometer (see figure 2). An atom diffracted by the first and second gratings will be found with a sinusoidal probability distribution at the plane of the third grating. The third grating acts as a mask of this interference pattern. We measure the flux as a function of grating position to determine the phase and contrast of the fringe pattern. The gratings are each separated by 940 mm. We detect $\langle N \rangle \approx 10^5$ atoms s^{-1} with a typical contrast of $C_0 \approx 25\%$ using a hot-wire detector 0.5 m beyond the third grating. See [1, 13, 14] for additional information.

We implemented phase choppers with electric field gradients switched on and off at a frequency f ranging from 0 to 30 kHz. We create the electric field gradient by periodically applying a voltage $V(t)$ of 1–5 kV to a $D = 1.57$ mm diameter copper wire at a distance $a = 1$ mm from a grounded aluminum strip. See [11], figure 3 for a schematic of the phase chopper. The high voltage is switched on and off in less than 200 ns with a DEI PVX-4130 pulse generator controlled by an SRS DS345 function generator. We place chopper 1 at a distance of approximately 300 mm after the first grating (and chopper 2 at a similar distance before the third grating). We measured the chopper 1 to chopper 2 distance as $L = 1270.68(25)$ mm. Two translation stages allow us to move the choppers perpendicular to the beam.

An atom with velocity v passing through the 1 mm gap in phase chopper i will acquire a differential phase shift

$$\phi_i(v, t) = c\frac{\alpha V(t)^2}{v}\frac{s(v)(2x_{0i} + s(v))}{(b^2 - x_{0i}^2)(b^2 - (x_{0i} + s(v))^2)}, \tag{3}$$

where $c = 8\pi^2 b/h \ln^{-2}((a + D/2 + b)/(a + D/2 - b))$, α is the atomic polarizability, v is the velocity of the atom, x_0 is the beam position relative to the ground plane, m is the mass of the atom, $b = a\sqrt{1 + D/a}$, $s(v) = hL_{gc}/mvd_g$ is the path separation at the chopper, d_g is the

IOP Institute of Physics **Φ** DEUTSCHE PHYSIKALISCHE GESELLSCHAFT
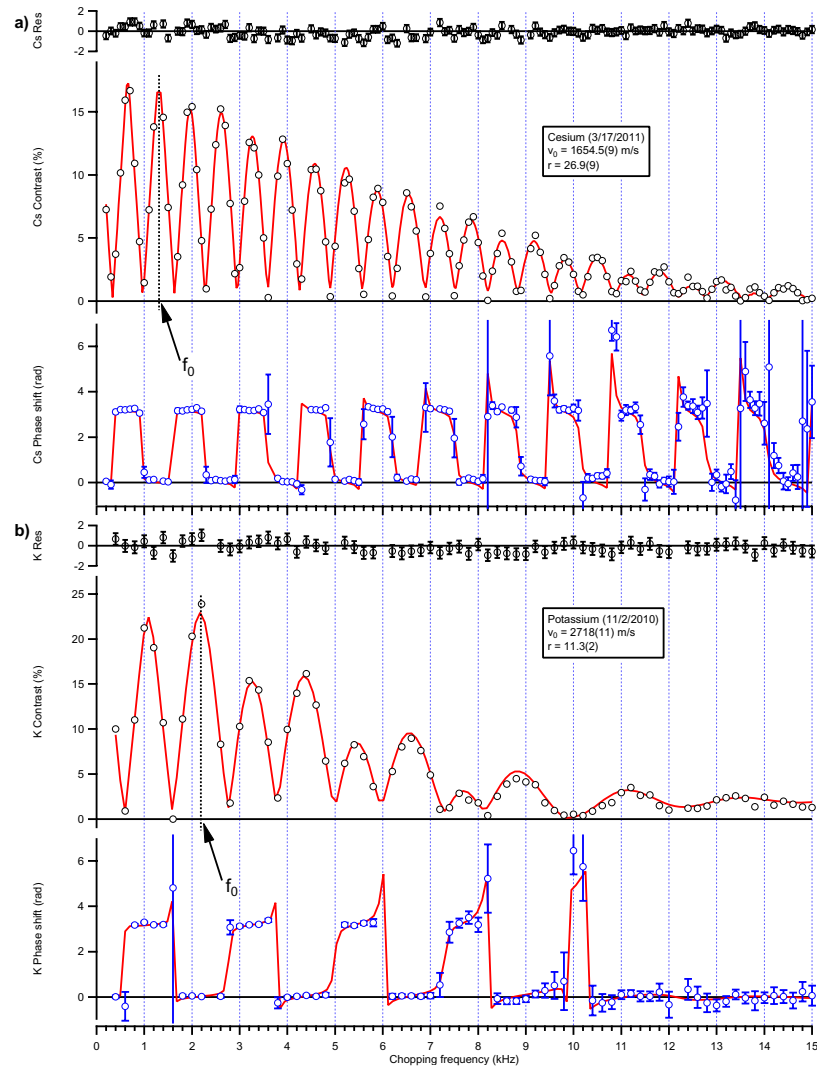
Figure 3. Phase chopper data (circles) and corresponding best-fit functions (red curves) for (a) a cesium atom beam with a 70% helium, 30% argon carrier gas and (b) a potassium atom beam with a 100% helium carrier gas and using ϕ_1 and ϕ_2 as free parameters in the least-squares fit rather than fixed at the measured values $\phi_{i\mathrm{DC}}$. f_0 for each data set is labeled. We fit the contrast (black) to find the flow velocity v_0 and velocity ratio r. The statistical error for each contrast measurement is shown in fit residuals. The measured phase (blue) is also shown, but is not fit. Each point is derived from 5 s of data.

grating period, L_{gc} is the distance from the first grating to chopper 1 or from the third grating to chopper 2, and h is Planck's constant. Classically, one may describe the differential phase shift by a transverse deflection in an electric field where the force is given by $\boldsymbol{F} = \alpha \boldsymbol{E} \boldsymbol{\nabla} \boldsymbol{E}$. See [1] for a full derivation of the acquired phase with a similar electrode geometry.

While equation (3) is useful for designing the chopper geometry for an expected atom beam velocity, we cannot use it directly to measure beam velocity. Doing so would require not only more accurate knowledge of the chopper geometry, but also knowledge of polarizability— the very quantity that we would like to eventually measure. Instead, we empirically tune the choppers to induce π and $-\pi$ differential phase shifts by adjusting the voltage V applied to both choppers and the position x_0 of each chopper individually. We refer to the actual induced differential phase shift as $\phi_{i\mathrm{DC}}$, where i is the chopper number. For 0.1% uncertainty velocity measurements, we can tolerate phase differences $(\phi_{i\mathrm{DC}} - \pi)/\pi$ as large as 5%, provided that the uncertainty in the measured phase shift is less than 0.5%.

After tuning and accurately measuring the chopper 1 and chopper 2 DC differential phase shifts $\phi_{i\mathrm{DC}}$, we are nearly ready to substitute them into equation (1) and measure contrast versus frequency to find velocity. First, however, we must make a correction to undo the effect of the velocity spread on the measurement of $\phi_{i\mathrm{DC}}$. The proper phase shift to input into equation (1) for velocity measurements is ϕ_{i0}, defined by

$$C_{i\mathrm{DC}}\mathrm{e}^{\mathrm{i}\phi_{i\mathrm{DC}}} = C_0 \int_{v=0}^{\infty} P(v, v_0, r)\mathrm{e}^{\mathrm{i}\phi_{i0}(v_0/v)^2}\,\mathrm{d}v. \tag{4}$$

Using the parameter ϕ_{i0} and the fact that $s(v) \ll x_0$, equation (3) can now be well approximated by

$$\phi_i(v, t) \approx \phi_{i0} \left(\frac{v_0}{v}\right)^2 \left(\frac{V(t)}{V_{\mathrm{DC}}}\right)^2. \tag{5}$$

Note that the $1/v^2$ dispersion comes from the fact that $s(v)$ in equation (3) is inversely proportional to v. In the limit of a very sharp velocity distribution, $r \to \infty$ and $\phi_{i0} \to \phi_{i\mathrm{DC}}$. Ignoring this correction and assuming $\phi_{i0} = \phi_{\mathrm{DC}}$ results in an error in v_0 of 0.1% for beams with $r = 10$, and 0.01% for beams with $r = 40$.

We proceed to measure the contrast and phase of the interference pattern at a series of chopping frequencies. We perform a least-squares fit of measured contrast using equation (1). Because ϕ_i depends on $P(v)$ through equations (4) and (5), we must numerically solve equation (4) for each iteration of the fit routine. The measured phase $\phi(f)$ provides a consistency check of the results of the contrast fit, but by itself is a less sensitive measure of velocity.

4. Results and errors

Figure 3(a) shows a chopper frequency scan from a beam with a slow v_0 and sharp r, and figure 3(b) shows a chopper frequency scan from a beam with a fast v_0 and broad r. We perform a least-squares fit of the contrast data to equation (1) to find v_0 and r. The error budget of the measurement is shown in table 1 and each parameter is discussed below. We estimate the uncertainty in v_0 and r due to each parameter by performing fits of the data at a parameter's central value and $+/-$ its uncertainty. We also tested the stability of the least-squares fits with respect to uncertainty in each parameter by halving and doubling the uncertainties.

IOP Institute of Physics ⏀ DEUTSCHE PHYSIKALISCHE GESELLSCHAFT

Table 1. Error budget for a typical velocity measurement with phase choppers.

Parameter	Value (Unc.)	Uncertainty in v_0 (%)
Stat error in v		0.04
L	1270.68(25) mm	0.02
ϕ_{1DC}/π	1.000(5)	0.01
ϕ_{2DC}/π	1.000(5)	0.01
Beam width	100(30) μm	0.04
Initial contrast C_0	25(2)%	0.04
Transit time	2 μs	0.005
Switching time	200 ns	0.001
Duty cycle	50.0(3)%	0.005
Sagnac phase shift	1.46(2) rad	0.005
Molecules	10(10)%	0.02
Total		0.08

We measured the distance between the two choppers, L, by inserting the ends of a calibrated tape measure between the wire and ground plane of each chopper. We subdivided the millimeter markings on the tape measure by analyzing high-resolution digital photographs of the tape measure inserted into each chopper. We took care to take the pictures with the chopper wire centered in the frame and from normal incidence to the ground plane. Thermal expansion may change the distance between choppers by no more than 150 μm (0.01%), significantly less than the measurement uncertainty in L.

Adding the Sagnac phase shift from the Earth's rotation into the analysis also yields small corrections to the best fit v_0 and r. The corrections to v_0 and r can be as large as 0.2 and 4%, respectively, for slower beams with smaller r. Holmgren *et al* [1] explains how we incorporate the Sagnac phase shift in our interferometer model. The uncertainty in this correction is negligible.

We add a correction to the phase chopper model to account for the nonzero width of the atom beam and additional interferometers formed by other diffraction orders. We model this correction by making $\phi_i(v, t)$ (equation (3)) a function of x_0 as well and then introducing an additional average over beam width (x_0) in equation (1). For the widest beams, the correction to v_0 and r is less than 0.1%, and the uncertainty in v_0 due to the beam width is less than 0.04%.

Despite accounting for the averaging of fringe patterns from the velocity distribution and beam width, the measured reference contrast is systematically 1–2% larger than the best-fit contrast parameter C_0. Fixing C_0 at its measured value in a least-squares fit of the chopper frequency scan typically results in an unrealistically small r, which then requires slightly slower v_0 to fit the data well. We estimate the uncertainty from this parameter by taking the full difference in fitted v_0 when using the two different initial contrasts. Future work is needed to discover the source of this uncertainty.

The voltage switching time and the transit time for atoms through the choppers introduce additional mechanisms by which the phase shifts may be different than desired. The switching time can be thought of as making the phase shifts depicted in figure 1 have fuzzy edges in time, while the finite extent of the electric field causes fuzzy edges in space. Both these corrections are negligible at our level of precision (see table 1).

Alkali dimer molecules slightly influence the chopper data as well. The rotationally averaged alkali dimer polarizabilities are slightly less than twice the atomic polarizabilities [15], but the de Broglie wavelength, and hence path separation $s(v)$, for the dimers is half as large. Therefore, dimers acquire slightly smaller differential phase shifts than atoms. We estimate the number of alkali dimers in the atom beam in three ways. Firstly, we examine the far-field diffraction pattern from the first grating when the diffraction angle (determined by the atoms' mass and velocity) is sufficiently large to observe resolved diffraction orders. Molecules produce diffraction peaks at 1/2 the diffraction angle of atoms and we can determine the fraction of molecules in the beam by comparing diffraction order intensities between atoms and molecules. Secondly, although we cannot use a measurement of the DC phase shift, ϕ_{iDC}, to determine atomic polarizabilities, as discussed in section 3, we can use it to estimate the number of molecules in the beam. Molecule fractions greater than 10% would produce DC phase shifts inconsistent with what we expect from the phase choppers at a given position and voltage. Finally, the quality of the least-squares fit to the chopper data noticeably decreases when the molecule fraction rises above 10%.

We tested phase chopper velocity measurements against less precise velocity measurements using diffraction from a nanograting. We found no discrepancy between the two methods. However, as described in [1], we must account for a small difference between the velocity distribution of the entire beam (as measured by diffraction) and the velocity distribution of the atoms detected in the interferometer (as measured by phase choppers). The difference exists because the dispersive nature of the nanogratings, combined with detector size and beam width, leads to a velocity distribution in the atom interferometer that depends on the position of the detector. For precision measurements, it is preferable to directly measure the velocities of atoms that contribute to the detected interference pattern and thus avoid the correction (0.25% in v_0) and its associated uncertainty (0.1%). In this respect, phase choppers are better than nanograting diffraction for measuring beam velocity in an atom interferometer.

We also tested the phase choppers by measuring the static ground state polarizability of cesium using beams with three very different flow velocities on three different days. Each day we alternated between measurements of beam velocity and polarizability every hour to account for small changes in velocity ($<0.5\%$) over the course of a day due to instability in beam source temperature. The statistical error of each measurement of velocity was less than 0.1%. To measure polarizability, we used a third electric field gradient region that will be described in a future publication. We find the cesium polarizability (stat. unc.) to be 59.84(4), 59.71(7) and 59.85(8) Å^3 at flow velocities of 925, 1345 and 1680 m s^{-1}. These polarizability measurements are subject to a systematic correction due to the third gradient region, but the consistency of the polarizability measurements provides strong evidence that our velocity measurements using phase choppers are reproducible at the 0.1% level.

Finally, we have also modeled and tested the phase choppers in the $\phi_{1DC} = +\pi$ and $\phi_{2DC} = +\pi$ mode. In the limit of an infinitely sharp velocity distribution ($r \to \infty$), there is no difference between the $+\pi$, $+\pi$ configuration and the $+\pi$, $-\pi$ configuration. However, the finite velocity spread and the fact that ϕ_{iDC} never exactly equals $\pm\pi$ results in the $+\pi$, $-\pi$ configuration yielding slightly more precise results than the $+\pi$, $+\pi$ configuration.

5. Conclusion

We used phase choppers to measure the velocity of atoms in an atom interferometer with 0.1%
uncertainty. Phase choppers work for continuous or pulsed beams, do not require resolved
diffraction, have no moving parts, and work well for many types of atoms and molecules.
These velocity measurements enable high-precision absolute and ratio measurements of atomic
polarizabilities. This work was supported by NSF Award no. 0969348.

References

[1] Holmgren W F, Revelle M C, Lonij V P A and Cronin A D 2010 Absolute and ratio measurements of the polarizability of Na, K, and Rb with an atom interferometer *Phys. Rev.* A **81** 053607
[2] Berninger M, Stefanov A, Deachapunya S and Arndt M 2007 Polarizability measurements of a molecule via a near-field matter-wave interferometer *Phys. Rev.* A **76** 013607
[3] Miffre A, Jacquey M, Büchner M, Trenec G and Vigué J 2006 Measurement of the electric polarizability of lithium by atom interferometry *Phys. Rev.* A **73** 011603
[4] Ekstrom C R, Schmiedmayer J, Chapman M S, Hammond T D and Pritchard D E 1995 Measurement of the electric polarizability of sodium with an atom interferometer *Phys. Rev.* A **51** 3883–8
[5] Lenef A, Hammond T D, Smith E T, Chapman M S, Rubenstein R A and Pritchard D E 1997 Rotation sensing with an atom interferometer *Phys. Rev. Lett.* **78** 760–3
[6] Gustavson T L, Bouyer P and Kasevich M A 1997 Precision rotation measurements with an atom interferometer gyroscope *Phys. Rev. Lett.* **78** 2046–9
[7] van den Meijdenberg C J N 1988 *Atomic and Molecular Beam Methods* vol 1, ed G Scoles (Oxford: Oxford University Press)
[8] Tikhonov G, Wong K, Kasperovich V and Kresin V V 2002 Velocity distribution measurement and two-wire field effects for electric deflection of a neutral supersonic cluster beam *Rev. Sci. Instrum.* **73** 1204–11
[9] Brezger B, Hackermüller L, Uttenthaler S, Petschinka J, Arndt M and Zeilinger A 2002 Matter-wave interferometer for large molecules *Phys. Rev. Lett.* **88** 100404
[10] Christen W, Krause T, Kobin B and Rademann K 2011 Precision velocity measurements of pulsed supersonic jets *J. Phys. Chem.* A **115** 6997–7004
[11] Roberts T D, Cronin A D, Tiberg M V and Pritchard D E 2004 Dispersion compensation for atom interferometry *Phys. Rev. Lett.* **92** 060405
[12] Roberts T D 2002 Measuring atomic properties with an atom interferometer *PhD Thesis* Massachusetts Institute of Technology
[13] Cronin A D, Schmiedmayer J and Pritchard D E 2009 Optics and interferometry with atoms and molecules *Rev. Mod. Phys.* **81** 1051
[14] Berman P (ed) 1997 *Atom Interferometry* (San Diego, CA: Academic)
[15] Tarnovsky V, Bunimovicz M, Vušković L, Stumpf B and Bederson B 1993 Measurements of the dc electric dipole polarizabilities of the alkali dimer molecules, homonuclear and heteronuclear *J. Chem. Phys.* **98** 3894

APPENDIX C

REPRINT: MEASUREMENT OF A WAVELENGTH OF LIGHT FOR WHICH
THE ENERGY SHIFT FOR AN ATOM VANISHES

The following manuscript was published as a peer-reviewed article in Physical Review Letters. The results of this article are discussed in section 2.3 and Chapter 5 provides supplementary information. The manuscript is reprinted with permission from the American Physical Society. Original reference: W. F. Holmgren, R. Trubko, I. Hromada, and A. D. Cronin, "*Measurement of a Wavelength of Light for Which the Energy Shift for an Atom Vanishes*", Physical Review Letters **109**, 243004, (2012). Copyright (2012) by the American Physical Society.

Measurement of a Wavelength of Light for Which the Energy Shift for an Atom Vanishes

William F. Holmgren,[1] Raisa Trubko,[2] Ivan Hromada,[1] and Alexander D. Cronin[1,2]

[1]*Department of Physics, University of Arizona, Tucson, Arizona 85721, USA*
[2]*College of Optical Sciences, University of Arizona, Tucson, Arizona 85721, USA*
(Received 22 August 2012; published 14 December 2012)

Light at a magic-zero wavelength causes a zero energy shift for an atom. We measured the longest magic-zero wavelength for ground state potassium atoms to be $\lambda_{\mathrm{zero}} = 768.9712(15)$ nm, and we show how this measurement provides an improved experimental benchmark for atomic structure calculations. This λ_{zero} measurement determines the ratio of the potassium atom $D1$ and $D2$ line strengths with record precision. It also demonstrates a new application for atom interferometry, and we discuss how decoherence will fundamentally limit future measurements of magic-zero wavelengths.

The light-induced energy shift of an atom depends on the light wavelength, and there exist *magic-zero wavelengths* for which the energy shift vanishes [1,2]. A magic-zero wavelength (λ_{zero}) is found between atomic resonances, where the light is red-detuned from one resonance and blue-detuned from another. Opposing contributions from these resonances produce a root in the energy shift spectrum at λ_{zero}. In this Letter, we report a measurement of a magic-zero wavelength made with an atom interferometer.

LeBlanc and Thywissen [1] referred to λ_{zero} as *tune-out wavelengths* and discussed their utility for multispecies atom traps. Since then, various λ_{zero} have been used in experiments to study entropy exchange [3], quantum information processing [4], and diffraction of matter waves from an ultracold atom crystal [5]. However, the light used in experiments [3–5] to minimize energy shifts can be hundreds of picometers different than the λ_{zero} values calculated in Refs. [1,2] due to impure optical polarization. LeBlanc and Thywissen predicted a λ_{zero} for each alkali atom with 10 pm precision based on the wavelengths of their principal ($D1$ and $D2$) transitions. More recently, Arora, Safronova, and Clark [2] predicted magic-zero wavelengths by using state-of-the-art atomic theory calculations of dipole matrix elements for several transitions in each atom, including core electron excitations. For the λ_{zero} we measured, Arora, Safronova, and Clark stated a theoretical uncertainty of 3 pm. In comparison, our measurement has an uncertainty of 1.5 pm. Because calculations of dipole matrix elements similar to those used in Ref. [2] are needed to calculate static polarizabilities, state lifetimes, line strengths, van der Waals potentials, and magic wavelengths [6–8], we are motivated to explore how measurements of magic-zero wavelengths can serve as new benchmark tests of atomic structure calculations.

In this Letter, we present a measurement of the magic-zero wavelength for potassium between the 770 ($D1$) and 767 nm ($D2$) transitions. Our measurement of $\lambda_{\mathrm{zero}} = 768.9712(14)_{\mathrm{stat}}(6)_{\mathrm{sys}}$ is a novel test of atomic structure calculations and provides the most precise determination

yet of the ratio of the $D1$ and $D2$ line strengths S_1 and S_2. We find the ratio

$$R = \frac{S_2}{S_1} = \frac{|\langle 4s||D||4p_{3/2}\rangle|^2}{|\langle 4s||D||4p_{1/2}\rangle|^2} = 2.0005(40). \quad (1)$$

The ratio of degeneracies for the excited states would make $R = 2$; however, relativistic corrections slightly reduce the predicted ratio to $R = 1.9987$ [9]. Our measurement is consistent with the prediction in Ref. [2], and our measurement uncertainty is half as much as the theoretical uncertainty quoted in Ref. [2].

Most measurements of static and dynamic polarizabilities [10–14] are limited by uncertainty in the electric field strength and uncertainty in the time an atom interacts with the field. However, our measurement of the wavelength at which the polarizability is zero is not subject to uncertainty from these factors. Instead, we will discuss systematic errors in λ_{zero} measurements caused by laser spectra and statistical limitations caused by contrast loss and small (mrad/pm) phase shifts near λ_{zero}.

The longest magic-zero wavelengths for alkali atoms are determined mostly by the transition energies $\hbar\omega_1$ and $\hbar\omega_2$ and the ratio R of the line strengths. We use the sum-over-states approach to describe the dynamic polarizability $\alpha(\omega)$ near these two transitions by

$$\alpha(\omega) = \frac{1}{3\hbar} S_1 \left(\frac{\omega_1}{\omega_1^2 - \omega^2} + R \frac{\omega_2}{\omega_2^2 - \omega^2} \right) + A, \quad (2)$$

where A accounts for contributions from core excitations, higher energy valence transitions, and core-valence coupling [6,15]. At the longest magic-zero wavelength of potassium, A is 0.02% of the nearly equal and opposite contributions from the principal transitions to the polarizability and A changes λ_{zero} by 0.15(1) pm [9]. Therefore, the uncertainty in this magic-zero wavelength calculation is nearly entirely determined by uncertainty in the ratio of the line strengths, R.

The line strengths S_1 and S_2, and thus R, can also be determined from state lifetime measurements. To our knowledge, the most precise *independent* measurements of the $4p_{1/2}$ and $4p_{3/2}$ state lifetimes were performed by Volz and Schmoranzer using beam-gas-laser spectroscopy [16]. They reported lifetime uncertainties of 0.25% and a similar uncertainty for R (which leads to a 2 pm uncertainty in λ_{zero}). In comparison, our measurement of R has an uncertainty of 0.20%. State lifetimes can also be derived from molecular or photoassociation spectroscopy [17,18]. However, these spectroscopy experiments [17,18] do not distinguish between the $4p_{1/2}$ and $4p_{3/2}$ state lifetimes (they depend on an average), so they cannot be used to determine R or λ_{zero}.

To measure the magic-zero wavelength, we focused 500 mW of laser light asymmetrically on the paths of our three grating Mach-Zehnder atom interferometer [19–21]. Atom waves propagating along each interferometer path acquired a phase shift $\phi(\omega)$ proportional to the dynamic polarizability $\alpha(\omega)$ at the laser frequency ω. We found the laser frequency $\omega_{zero} = 2\pi c/\lambda_{zero}$ at which the dynamic polarizability vanishes by measuring the phase shift as a function of laser wavelength.

The phase shift $\phi_0(\omega)$ along one interferometer path is given by

$$\phi_0(\omega) = \frac{\alpha(\omega)}{2\epsilon_0 c \hbar v} \int_{-\infty}^{\infty} I(x, z) dz, \tag{3}$$

where $v \approx 1600$ m/s is the atom velocity, $I(x, z)$ is the laser beam intensity (assumed to be monochromatic for now), x is the transverse coordinate in the plane of the interferometer, and z is the longitudinal coordinate. The laser beam intensity was 400 W/cm^2 (500 mW focused to a beam waist of ≈ 200 μm). We measure the differential phase shift $\phi(\omega)$ for two components of the atomic wave functions that are separated by 60 μm in our atom interferometer. Figure 1 shows the differential phase shift and contrast of the interferometer as the laser wavelength is scanned 5 nm across the $D1$ and $D2$ lines.

Equation (3) is useful for understanding the origin of the phase shift, similar to $\phi(\omega)$ shown in Refs. [11,13]. But our measurements of λ_{zero} do not depend on precise knowledge of the atom beam velocity or the focused laser beam irradiance. Changes in these parameters would affect only the magnitude of the phase shift, not the zero crossing. Therefore, we reduce Eq. (3) to simply

$$\phi(\omega) = b\alpha(\omega), \tag{4}$$

where b is a parameter proportional to the laser beam intensity and the interaction time. To precisely measure λ_{zero}, we studied phase shifts within 100 pm of λ_{zero}, as shown in Fig. 2. The laser power changed with wavelength and drifted over time, so we monitored the power incident on the atom beam and normalized the measured phase shifts. We reproduced this 1 h experiment 35 times over a period of 5 d. We fit these data to Eqs. (2) and (4), with R
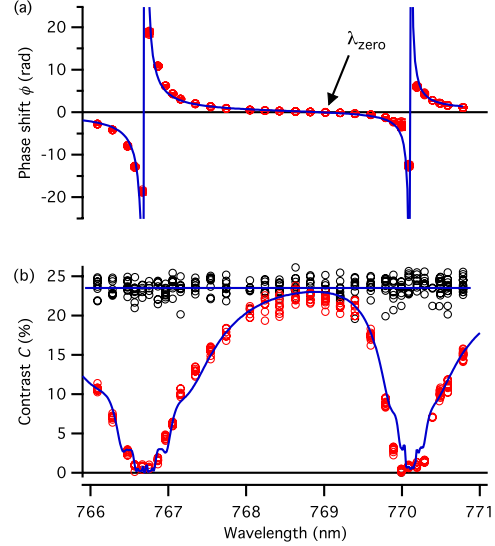
FIG. 1 (color online). Measurements of the interferometer (a) phase shift ϕ and (b) contrast C as a function of laser wavelength. The measured phase shifts are normalized by the laser power at that wavelength. The reference contrast C_0 is shown as black circles.

and b as the only free parameters. The precision with which we can determine λ_{zero} is determined by the slope $d\phi/d\lambda$. This slope is typically 1 mrad/pm, and our phase uncertainty from shot noise is $\delta\phi \approx 1$ mrad with 5 min of data.

Our reported measurement of the magic-zero wavelength is the average of 35 individual measurements of

FIG. 2 (color online). Measurements of phase shift and laser wavelength. Each point represents 5 min of data. The fit uses Eqs. (2) and (4) described in the text, with free parameters R and b. R determines λ_{zero}.

λ_{zero} after discarding the highest and lowest 10% of the measurements. The reported statistical error (1.4 pm) is twice the standard error of the mean of the trimmed data set. Figure 3 shows the 35 λ_{zero} m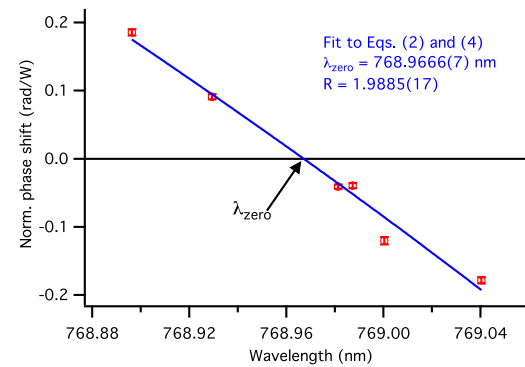easurements and the trimmed mean. Table I shows a summary of the error budget, and we discuss systematic errors associated with the laser system below.

We generated 2 W of laser light using a master oscillator power amplifier system [22,23]. We used a Littrow extended cavity diode laser with wavelength-dependent pointing compensation [24] to keep the seed light well coupled into a tapered amplifier over a 5 nm tuning range. A Bristol Instruments 621B wavelength meter calibrated against a saturated absorption signal in a vapor cell measured the vacuum wavelength of the seed laser with an uncertainty of 0.3 pm.

After spatial filtering with a single mode fiber, 1% of the power was in a broadband spectral component from spontaneous emission in the tapered amplifier [25]. To quantify the uncertainty in λ_{zero} caused by this broadband component, we characterized the laser spectrum with a grating spectrometer, and we accounted for the laser spectrum by modifying Eq. (3) with an additional integral over the frequency-dependent laser intensity. We calculated that the broadband light introduces an uncertainty of 0.5 pm to our measurement of λ_{zero}.

We also measured the crossing angle between the laser and atom beams and applied a 0.56(5) pm correction to λ_{zero} due to the Doppler shift. We note that our measurement was performed on an atom beam with a natural abundance of potassium isotopes. If we assume that R is the same for ^{39}K and ^{41}K, then the measured λ_{zero} is predicted to be 0.03 pm less than the ^{39}K λ_{zero}. Finally, we calculated that, at the intensity we are using, the hyperpolarizability of the ground state causes a shift for λ_{zero} on

the order of 0.001 pm. This is negligible in our current experiment but suggests an interesting opportunity for future measurements of intensity-dependent shifts in λ_{zero} due to higher order effects.

Contrast loss due to several factors analogous to inhomogeneous broadening limits the precision with which λ_{zero} can be measured. Averaging over the width of the atom beam and accounting for $+1$ and -1 diffraction orders from the first nanograting explains most of the observed contrast loss in Fig. 1(b) [19]. The velocity spread of the atom beam ($\sigma_v \approx v_0/15$) slightly reduced the observable contrast as well. The small contrast loss due to light at λ_{zero} can be explained by unintended elliptical polarization of the laser beam. Circular polarization causes different Zeeman substates (m_F) to acquire different phase shifts even at λ_{zero}. Averaging over all eight $|F, m_F\rangle$ states in our experiment reduces the contrast but introduces little error to λ_{zero} thanks to the equal (thermally distributed) populations of all m_F in our atom beam. We allow for a conservative 0.1 pm uncertainty in λ_{zero} due to unaccounted-for effects such as quadratic Zeeman shifts or optical pumping compounded with the light polarization.

Because of the contrast loss from all these mechanisms, if we could optimize our experiment just by increasing the laser power without bound, we would choose only 10 times more power. Furthermore, this would result in only 5 times better sensitivity, approaching 50 pm/$\sqrt{\text{Hz}}$. If we had power to spare, one way to maintain higher contrast would be to use a triangular mask for a large area light beam. This would cause the differential phase shift to be independent of position in the atom beam.

Next, we explore how photon scattering, analogous to homogeneous broadening, imposes a fundamental limit on the precision with which any magic-zero wavelength can be measured, even in different types of experiments. Atom interferometers are, in principle, ideal tools for studying the small energy shifts that result from light near λ_{zero}. However, magic-zero wavelengths may also be measured with other methods. For example, atom loss rates in an optical dipole trap would increase near λ_{zero}. A Bose-Einstein condensate imprinted by a light beam redder
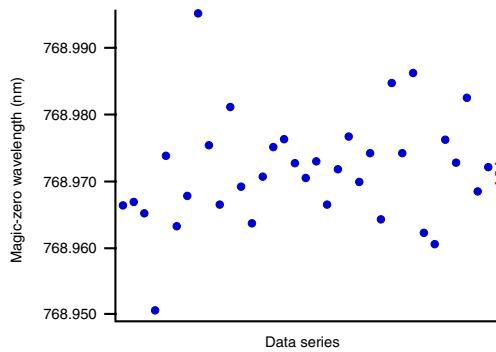
FIG. 3 (color online). The 35 separate λ_{zero} measurements (solid blue) and the trimmed mean (open red). We assumed that the statistical errors of all measurements were the same, and we report twice the standard error of the trimmed mean as the final statistical error.

TABLE I. Magic-zero wavelength error budget.

Source of error	λ_{zero} error (pm)
Laser wavelength	0.3
Broadband light	0.5
Polarization	0.1
Doppler shift	0.05
Total systematic error	0.6
Total statistical error	1.4
Total error	1.5

(or bluer) than the magic-zero wavelength may produce light (or dark) solitons. Studying vortex excitation probability from a laser stir stick [26] may provide another way to measure λ_{zero} in Bose-Einstein condensate systems. Atoms can diffract from an optical lattice near (but not at) λ_{zero}, and atom beam deflections can be induced by light detuned from λ_{zero} [12]. But all of these methods essentially rely on changes to the center of mass motion for atoms or, equivalently, changes to the de Broglie wave that represents this motion. Atomic clocks provide similar (picometer) precision for measurements of the magic wavelengths (λ_{magic}) that depend on the differential light shift for two states [7,8], but, because clocks are affected by shifts in both ground and excited states, they are less ideal for measurement of magic-zero wavelengths (λ_{zero}) discussed here. Furthermore, all of these proposed experiments are limited by decoherence or heating due to photon scattering.

To quantify this fundamental limitation due to decoherence in our experiment, let Δ_i be the detuning from resonance i, Ω_i be the Rabi frequency, and T be the time that an atom is exposed to the laser beam. In the large detuning limit ($\Delta_i^2 \gg \Omega_i^2$), the slope $d\phi/d\lambda$ is proportional to $\sum_i T \Omega_i^2/\Delta_i^2$, whereas the phase uncertainty increases exponentially with the same factor [27]. This indicates that a more powerful laser or a longer interaction time offers diminishing returns for the experimental sensitivity to λ_{zero}. To minimize the shot noise limited uncertainty in λ_{zero}, we should increase the pulse area (IT) until we obtain a contrast reduction of $C/C_0 = e^{-1}$.

Our experiment could be significantly improved by increasing the atom interferometer path separation so the laser can be entirely focused (with homogeneous irradiance) on one interferometer path. The elliptical polarization could be reduced by a factor of 10^5 by passing the laser beam through a high quality polarizer immediately before it crosses the atom beam, and the broadband light component could be reduced by using a different type of laser or filtering the light with a grating and aperture. In this more ideal situation, decoherence is the only remaining source of contrast loss. We calculated a maximum achievable slope $d\phi/d\lambda$ of

$$\frac{d\phi}{d\omega} \approx \frac{1}{2\Gamma} P_s, \qquad (5)$$

where P_s is the probability that an atom scatters one or more photons and Γ is the excited state decay rate. With optimized contrast loss due to scattering ($P_s = 1 - e^{-1}$), the slope becomes as large as $d\phi/d\lambda = 40$ rad/pm. In this way, future measurements of magic-zero wavelengths can be made with very high precision, possibly with accuracy limited by a shot noise sensitivity better than picometers per $\sqrt{\mathrm{Hz}}$ with current technology. Perhaps this can be achieved in an ultracold atom interferometer [11]; however, such experiments typically would measure the magic-zero wavelength of a particular $|F, m_F\rangle$ state and therefore may be more sensitive to uncertainties in the laser polarization and magnetic fields.

As an outlook, the λ_{zero} measurement presented here provides a foundation for a new set of experimental benchmarks that can be used to test atomic structure calculations. Future measurements of several other magic-zero wavelengths in potassium and other atoms can be accomplished with similar techniques. For example, in potassium atoms, two additional magic-zero wavelengths occur near the $4s$ to $5p_j$ transitions. One magic-zero wavelength near 405.96 (4) nm is between the $4s - 4p$ and $4s - 5p$ transitions, while the other magic-zero wavelength near 404.72(4) nm is between the $4s - 5p_{1/2}$ and $4s - 5p_{3/2}$ transitions. Therefore, measurements of two other λ_{zero} combined with the one reported here could be used to specify ratios of four line strengths. However, α_{core} [the largest component of the semiempirical parameter A in Eq. (2)] more strongly affects λ_{zero} near 405 nm [9]. Therefore, new λ_{zero} measurements will also provide benchmark tests for the contributions from core electrons to polarizabilities. Magic-zero wavelength measurements in heavier atoms, where the fine-structure splitting is larger, will be more sensitive to both core-electron contributions and relativistic corrections to the line strength ratio R. Measurements of hyperpolarizability may also be accomplished by measuring energy shifts at magic-zero wavelengths that depend on intensity squared (i.e., E^4).

In summary, we measured the longest magic-zero wavelength of potassium with 1.5 pm uncertainty. The measured phase shifts and resulting precision in λ_{zero} could be increased by 3 orders of magnitude in future work by focusing a laser beam entirely on one path of the atom interferometer, more accurate measurements of the laser spectrum, and more careful control of the laser polarization.

Note added.—Recently, we became aware of a recent λ_{zero} measurement in rubidium [28].

[1] L. J. LeBlanc and J. H. Thywissen, Phys. Rev. A **75**, 053612 (2007).

[2] B. Arora, M. S. Safronova, and C. W. Clark, Phys. Rev. A **84**, 043401 (2011).

[3] J. Catani, G. Barontini, G. Lamporesi, F. Rabatti, G. Thalhammer, F. Minardi, S. Stringari, and M. Inguscio, Phys. Rev. Lett. **103**, 140401 (2009).

[4] A. J. Daley, M. M. Boyd, J. Ye, and P. Zoller, Phys. Rev. Lett. **101**, 170504 (2008).

[5] B. Gadway, D. Pertot, J. Reeves, and D. Schneble, Nat. Phys. **8**, 544 (2012).

[6] J. Mitroy, M. S. Safronova, and C. W. Clark, J. Phys. B **43**, 202001 (2010).

PHYSICAL REVIEW LETTERS

[7] A. Derevianko and H. Katori, Rev. Mod. Phys. **83**, 331 (2011).

[8] A. D. Ludlow, T. Zelevinsky, G. K. Campbell, S. Blatt, M. M. Boyd, M. H. G. de Miranda, M. J. Martin, J. W. Thomsen, S. M. Foreman, J. Ye, T. M. Fortier, J. E. Stalnaker, S. A. Diddams, Y. Le Coq, Z. W. Barber, N. Poli, N. D. Lemke, K. M. Beck, and C. W. Oates, Science **319**, 1805 (2008).

[9] M. S. Safronova (personal communications).

[10] J. M. Amini and H. Gould, Phys. Rev. Lett. **91**, 153001 (2003).

[11] B. Deissler, K. J. Hughes, J. H. T. Burke, and C. A. Sackett, Phys. Rev. A **77**, 031604 (2008).

[12] H. Gould and T. Miller, Adv. At. Mol. Opt. Phys. **51**, 343 (2005).

[13] A. Morinaga, T. Tako, and N. Ito, Phys. Rev. A **48**, 1364 (1993).

[14] L. Hackermüller, K. Hornberger, S. Gerlich, M. Gring, H. Ulbricht, and M. Arndt, Appl. Phys. B **89**, 469 (2007).

[15] M. S. Safronova, B. Arora, and C. W. Clark, Phys. Rev. A **73**, 022505 (2006).

[16] U. Volz and H. Schmoranzer, Phys. Scr. **T65**, 48 (1996).

[17] S. Falke, I. Sherstov, E. Tiemann, and C. Lisdat, J. Chem. Phys. **125**, 224303 (2006).

[18] H. Wang, P. L. Gould, and W. C. Stwalley, J. Chem. Phys. **106**, 7899 (1997).

[19] W. F. Holmgren, M. C. Revelle, V. P. A. Lonij, and A. D. Cronin, Phys. Rev. A **81**, 053607 (2010).

[20] A. D. Cronin, J. Schmiedmayer, and D. E. Pritchard, Rev. Mod. Phys. **81**, 1051 (2009).

[21] *Atom Interferometry*, edited by P. Berman (Academic Press, San Diego, 1997).

[22] V. Bolpasi and W. von Klitzing, Rev. Sci. Instrum. **81**, 113108 (2010).

[23] R. A. Nyman, G. Varoquaux, B. Villier, D. Sacchet, F. Moron, Y. L. Coq, A. Aspect, and P. Bouyer, Rev. Sci. Instrum. **77**, 033105 (2006).

[24] C. J. Hawthorn, K. P. Weber, and R. E. Scholten, Rev. Sci. Instrum. **72**, 4477 (2001).

[25] D. Voigt, E. Schilder, R. Spreeuw, and H. van Linden van den Heuvell, Appl. Phys. B **72**, 279 (2001).

[26] T. W. Neely, E. C. Samson, A. S. Bradley, M. J. Davis, and B. P. Anderson, Phys. Rev. Lett. **104**, 160401 (2010).

[27] By using the rotating wave approximation, $\phi(\omega) \propto \sum_i T\Omega_i^2/\Delta_i$ and $d\phi/d\omega \propto \sum_i T\Omega_i^2/\Delta_i^2$. Because of photon scattering, the contrast $C \propto \exp(-\sum_i T\Omega_i^2/\Delta_i^2)$, and $\delta\phi \propto C^{-1}$.

[28] C. D. Herold, V. D. Vaidya, X. Li, S. L. Rolston, J. V. Porto, and M. S. Safronova, preceding Letter, Phys. Rev. Lett. **109**, 243003 (2012).

APPENDIX D

LIST OF PUBLICATIONS CO-AUTHORED BY W.F. HOLMGREN

Peer-reviewed publications:

1. W.F. Holmgren, R. Trubko, I. Hromada, and A.D. Cronin, *"Measurement of a Wavelength of Light for Which the Energy Shift for an Atom Vanishes"* Physical Review Letters **109**, 243004, (2012).

2. W.F. Holmgren, I. Hromada, C.E. Klauss, and A.D. Cronin, *"Atom beam velocity measurements using phase choppers"* New Journal of Physics 13, 115007 (2011).

3. V.P.A. Lonij, C.E. Klauss, W.F. Holmgren, and A.D. Cronin, *"Can atom-surface potential measurements test atomic structure models?"*, Journal of Physical Chemistry **115**, 7134 (2011).

4. V.P.A. Lonij, C.E. Klauss, W.F. Holmgren, and A.D. Cronin, *"Ratio measurements of atom-surface potentials reveal effect of core electrons"*, Physical Review Letters **105**, 233202 (2010).

5. W.F. Holmgren, M.C. Revelle, V.P.A. Lonij, and A.D. Cronin *"Absolute and ratio measurements of the polarizability of Na, K, and Rb with an atom interferometer"*, Physical Review A **81**, 053607 (2010).

6. V.P.A. Lonij, W.F. Holmgren, and A.D. Cronin, *"Magic ratio of window width to grating period for van der Waals potential measurements using material gratings"*, Physical Review A **80**, 062904 (2009).

Presentations and posters:

1. Chemical Physics Program Seminar, UA Chemistry Dept., 2012, Talk: *"Magic-zero wavelengths and their applications"* W.F. Holmgren, R. Trubko, I. Hromada, and A.D. Cronin.

2. APS DAMOP 2012, Anaheim, Talk: *"Measurement of the first tune-out wavelength of K with an atom interferometer"* W.F. Holmgren, R. Trubko, I. Hromada, and A.D. Cronin.

3. APS DAMOP 2011, Atlanta, Talk: *"Polarizability measurements of the ground and metastable states of Sr, Yb, and Ba"* W.F. Holmgren, I. Hromada, C.E. Klauss, V.P.A Lonij, and A.D. Cronin.

4. APS DAMOP 2010, Houston, Talk: *"Absolute and ratio measurements of the polarizability of Na, K, and Rb"* W.F. Holmgren, M.C. Revelle, V.P.A. Lonij, and A.D. Cronin.

5. APS DAMOP 2010, Houston Poster: *"A multispecies atom interferometer"* I. Hromada, C.E. Klauss, W.F. Holmgren, V.P.A. Lonij, and A.D. Cronin.

6. Low Energy Seminar, UA Physics Dept., 2010, Talk: *"Absolute and ratio measurements of the polarizability of Na, K, and Rb"* W.F. Holmgren, M.C. Revelle, V.P.A. Lonij, and A.D. Cronin.

7. Frontiers of Matterwave Optics 2010, Crete, Greece, Poster: *"Absolute and ratio measurements of the polarizability of Na, K, and Rb"* W.F. Holmgren, M.C. Revelle, V.P.A. Lonij, and A.D. Cronin.

8. APS DAMOP 2009, Charlottesville, Poster: *"Atom interferometry measurements of the polarizability of Na, K, and Rb"*, W.F. Holmgren, M. C. Revelle, V. P. A. Lonij, and A. D. Cronin.

9. APS DAMOP 2007, Poster: *Portable Atom Chip Vacuum Cell for Rapid BEC Production* , M. B. Squires, E. A. Salim, W.F. Holmgren, D. Z. Anderson, S. E. McBride, S. A. Lipp, J. F. Denatale, R. E. Mihailovich.

Other works:

1. A.D. Cronin and W.F. Holmgren, *"Matter waves in a new light"* Nature Physics **9**, 137, (2013).

2. A.D. Cronin, W.F. Holmgren, I. Hromada, C.E. Klauss, V.P.A. Lonij, B.J. McMorran, *"New applications for nanogratings in matter wave optics"* Appendix H in V.P.A. Lonij's thesis, available at www.atomwave.org

3. S.E. McBride, S.A. Lipp, J.J. Michalchuk, D.Z. Anderson, W.F. Holmgren, M.B. Squires, *Alkali metal dispenser and uses for same*, U.S. Patent No. 7955551.

REFERENCES

[1] B. Bederson and E. J. Robinson, *Beam Measurements of Atomic Polarizabilities* (John Wiley & Sons, Inc., 1966), pp. 1–27.

[2] T. Miller, *CRC Handbook of Chemistry and Physics* (CRC Press/Taylor and Francis, Boca Raton, 2012), chap. Atomic and molecular polarizabilities, pp. 10–187, 93rd ed.

[3] A. D. Ludlow, T. Zelevinsky, G. K. Campbell, S. Blatt, M. M. Boyd, M. H. G. de Miranda, M. J. Martin, J. W. Thomsen, S. M. Foreman, J. Ye, et al., Science **319**, 1805 (2008).

[4] A. Derevianko and H. Katori, Rev. Mod. Phys. **83**, 331 (2011).

[5] C. S. Wood, S. C. Bennett, D. Cho, B. P. Masterson, J. L. Roberts, C. E. Tanner, and C. E. Wieman, Science **275**, 1759 (1997).

[6] K. Tsigutkin, D. Dounas-Frazer, A. Family, J. E. Stalnaker, V. V. Yashchuk, and D. Budker, Phys. Rev. Lett. **103**, 071601 (2009).

[7] A. Derevianko and S. Porsev, The European Physical Journal A - Hadrons and Nuclei **32**, 517 (2007).

[8] W. F. Holmgren, M. C. Revelle, V. P. A. Lonij, and A. D. Cronin, Phys. Rev. A **81**, 053607 (2010).

[9] W. F. Holmgren, I. Hromada, C. E. Klauss, and A. D. Cronin, New Journal of Physics **13**, 115007 (2011).

[10] W. F. Holmgren, R. Trubko, I. Hromada, and A. D. Cronin, Phys. Rev. Lett. **109**, 243004 (2012).

[11] J. Mitroy, M. S. Safronova, and C. W. Clark, Journal of Physics B: Atomic, Molecular and Optical Physics **43**, 202001 (2010).

[12] H. Gould and T. Miller, Advances in Atomic Molecular and Optical Physics **51**, 343 (2005).

[13] U. Hohm, Vacuum **58**, 117 (2000).

[14] T. M. Miller and B. Bederson (Academic Press, 1989), vol. 25 of *Advances in Atomic and Molecular Physics*, pp. 37 – 60.

[15] T. M. Miller and B. Bederson (Academic Press, 1978), vol. 13 of *Advances in Atomic and Molecular Physics*, pp. 1 – 55.

[16] H. Scheffers and J. Stark, Physik. Z **35**, 625 (1934).

[17] B. Bederson, J. Eisinger, K. Rubin, and A. Salop, Review of Scientific Instruments **31**, 852 (1960).

[18] A. Salop, E. Pollack, and B. Bederson, Phys. Rev. **124**, 1431 (1961).

[19] W. D. Hall and J. C. Zorn, Phys. Rev. A **10**, 1141 (1974).

[20] R. W. Molof, H. L. Schwartz, T. M. Miller, and B. Bederson, Phys. Rev. A **10**, 1131 (1974).

[21] R. W. Molof, T. M. Miller, H. L. Schwartz, B. Bederson, and J. T. Park, The Journal of Chemical Physics **61**, 1816 (1974).

[22] H. L. Schwartz, T. M. Miller, and B. Bederson, Phys. Rev. A **10**, 1924 (1974).

[23] T. M. Miller and B. Bederson, Phys. Rev. A **14**, 1572 (1976).

[24] V. Tarnovsky, M. Bunimovicz, L. Vušković, B. Stumpf, and B. Bederson, J. Chem. Phys. **98**, 3894 (1993).

[25] C. R. Ekstrom, J. Schmiedmayer, M. S. Chapman, T. D. Hammond, and D. E. Pritchard, Phys. Rev. A **51**, 3883 (1995).

[26] A. Miffre, M. Jacquey, M. Büchner, G. Trenec, and J. Vigué, Phys. Rev. A **73**, 011603 (2006).

[27] S. Lepoutre, V. Lonij, H. Jelassi, G. Trénec, M. Büchner, A. Cronin, and J. Vigué, The European Physical Journal D - Atomic, Molecular, Optical and Plasma Physics **62**, 309 (2011).

[28] J. B. Fixler, G. T. Foster, J. M. McGuirk, and M. A. Kasevich, Science **315**, 74 (2007).

[29] A. Lenef, T. D. Hammond, E. T. Smith, M. S. Chapman, R. A. Rubenstein, and D. E. Pritchard, Phys. Rev. Lett. **78**, 760 (1997).

[30] T. L. Gustavson, P. Bouyer, and M. A. Kasevich, Phys. Rev. Lett. **78**, 2046 (1997).

[31] M. Berninger, A. Stefanov, S. Deachapunya, and M. Arndt, Phys. Rev. A **76**, 013607 (2007).

[32] B. Deissler, K. J. Hughes, J. H. T. Burke, and C. A. Sackett, Phys. Rev. A **77**, 031604 (2008).

[33] J. M. Amini and H. Gould, Phys. Rev. Lett. **91**, 153001 (2003).

[34] S. G. Porsev, K. Beloy, and A. Derevianko, Phys. Rev. Lett. **102**, 181601 (2009).

[35] S. Schäfer, S. Heiles, J. A. Becker, and R. Schäfer, J. Chem. Phys. **129**, 044304 (2008).

[36] J. Levine, R. J. Celotta, and B. Bederson, Phys. Rev. **171**, 31 (1968).

[37] T. P. Guella, T. M. Miller, B. Bederson, J. A. D. Stockdale, and B. Jaduszliwer, Phys. Rev. A **29**, 2977 (1984).

[38] T. Guella, T. M. Miller, J. A. D. Stockdale, B. Bederson, and L. Vušković, The Journal of Chemical Physics **94**, 6857 (1991).

[39] W. D. Knight, K. Clemenger, W. A. de Heer, and W. A. Saunders, Phys. Rev. B **31**, 2539 (1985).

[40] G. Tikhonov, V. Kasperovich, K. Wong, and V. V. Kresin, Phys. Rev. A **64**, 063202 (2001).

[41] A. Dalgarno, Advances in Physics **11**, 281 (1962).

[42] E.-A. Reinsch and W. Meyer, Phys. Rev. A **14**, 915 (1976).

[43] W. Müller, J. Flesch, and W. Meyer, J. Chem. Phys. **80**, 3297 (1984).

[44] A. Derevianko, W. R. Johnson, M. S. Safronova, and J. F. Babb, Phys. Rev. Lett. **82**, 3589 (1999).

[45] M. S. Safronova, W. R. Johnson, and A. Derevianko, Phys. Rev. A **60**, 4476 (1999).

[46] I. S. Lim, P. Schwerdtfeger, B. Metz, and H. Stoll, J. Chem. Phys. **122**, 104103 (2005).

[47] M. S. Safronova, B. Arora, and C. W. Clark, Phys. Rev. A **73**, 022505 (2006).

[48] L.-Y. Tang, Z.-C. Yan, T.-Y. Shi, and J. Mitroy, Phys. Rev. A **81**, 042521 (2010).

[49] B. Arora, M. S. Safronova, and C. W. Clark, Phys. Rev. A **76**, 052516 (2007).

[50] B. Arora and B. K. Sahoo, Phys. Rev. A **86**, 033416 (2012).

[51] N. F. Ramsey, *Molecular Beams* (Oxford University Press, 1956).

[52] P. Berman, ed., *Atom Interferometry* (Academic Press, San Diego, 1997).

[53] A. Miffre, M. Jacquey, M. Büchner, G. Trénec, and J. Vigué, Physica Scripta **74**, C15 (2006).

[54] A. D. Cronin, J. Schmiedmayer, and D. E. Pritchard, Rev. Mod. Phys. **81**, 1051 (2009).

[55] K. Hornberger, S. Gerlich, P. Haslinger, S. Nimmrichter, and M. Arndt, Rev. Mod. Phys. **84**, 157 (2012).

[56] D. W. Keith, C. R. Ekstrom, Q. A. Turchette, and D. E. Pritchard, Phys. Rev. Lett. **66**, 2693 (1991).

[57] M. R. Andrews, C. G. Townsend, H.-J. Miesner, D. S. Durfee, D. M. Kurn, and W. Ketterle, Science **275**, 637 (1997).

[58] B. Brezger, L. Hackermüller, S. Uttenthaler, J. Petschinka, M. Arndt, and A. Zeilinger, Phys. Rev. Lett. **88**, 100404 (2002).

[59] Y.-J. Wang, D. Z. Anderson, V. M. Bright, E. A. Cornell, Q. Diot, T. Kishimoto, M. Prentiss, R. A. Saravanan, S. R. Segal, and S. Wu, Phys. Rev. Lett. **94**, 090405 (2005).

[60] O. Garcia, B. Deissler, K. J. Hughes, J. M. Reeves, and C. A. Sackett, Phys. Rev. A **74**, 031601 (2006).

[61] S. Hofferberth, I. Lesanovsky, B. Fischer, J. Verdu, and J. Schmiedmayer, Nature Physics Phys **2**, 710 (2006).

[62] S. Gerlich, L. Hackermueller, K. Hornberger, A. Stibor, H. Ulbricht, M. Gring, F. Goldfarb, T. Savas, M. Mueri, M. Mayor, et al., Nature Physics **3**, 711 (2007).

[63] S.-w. Chiow, T. Kovachy, H.-C. Chien, and M. A. Kasevich, Phys. Rev. Lett. **107**, 130403 (2011).

[64] D. A. Kokorowski, Ph.D. thesis, MIT (2001).

[65] T. D. Roberts, Ph.D. thesis, MIT (2002).

[66] J. D. Perreault, Ph.D. thesis, University of Arizona (2005).

[67] B. McMorran, Ph.D. thesis, University of Arizona (2009).

[68] V. P. A. Lonij and A. D. Cronin, Ph.D. thesis, University of Arizona (2011).

[69] H. Haberland, U. Buck, and M. Tolle, Rev. Sci. Instrum. **56**, 1712 (1985).

[70] C. J. N. van den Meijdenberg, *Atomic and Molecular Beam Methods* (Oxford University Press, 1988), vol. 1.

[71] R. Delhuille, A. Miffre, E. Lavallette, M. Buchner, C. Rizzo, G. Trenec, J. Vigue, H. J. Loesch, and J. P. Gauyacq, Review of Scientific Instruments **73**, 2249 (2002).

[72] V. P. A. Lonij, W. F. Holmgren, and A. D. Cronin, Phys. Rev. A **80**, 062904 (2009).

[73] V. P. A. Lonij, C. E. Klauss, W. F. Holmgren, and A. D. Cronin, Phys. Rev. Lett. **105**, 233202 (2010).

[74] J. D. Perreault, A. D. Cronin, and T. A. Savas, Phys. Rev. A **71**, 053612 (pages 6) (2005).

[75] J. Mitroy and M. W. J. Bromley, Phys. Rev. A **68**, 052714 (2003).

[76] C. E. Klauss, Ph.D. thesis, University of Arizona (2011).

[77] T. D. Roberts, A. D. Cronin, M. V. Tiberg, and D. E. Pritchard, Phys. Rev. Lett. **92**, 060405 (2004).

[78] J. Catani, G. Barontini, G. Lamporesi, F. Rabatti, G. Thalhammer, F. Minardi, S. Stringari, and M. Inguscio, Phys. Rev. Lett. **103**, 140401 (2009).

[79] A. J. Daley, M. M. Boyd, J. Ye, and P. Zoller, Phys. Rev. Lett. **101**, 170504 (2008).

[80] B. Gadway, D. Pertot, J. Reeves, and D. Schneble, Nat Phys **8**, 544 (2012).

[81] M. S. Safronova (2012), personal communications.

[82] R. C. Hilborn, American Journal of Physics **50**, 982 (1982).

[83] M. S. Chapman, C. R. Ekstrom, T. D. Hammond, R. A. Rubenstein, J. Schmiedmayer, S. Wehinger, and D. E. Pritchard, Phys. Rev. Lett. **74**, 4783 (1995).

[84] D. A. Kokorowski, A. D. Cronin, T. D. Roberts, and D. E. Pritchard, Phys. Rev. Lett. **86**, 2191 (2001).

[85] C. J. Hawthorn, K. P. Weber, and R. E. Scholten, Review of Scientific Instruments **72**, 4477 (2001).

[86] V. Bolpasi and W. von Klitzing, Review of Scientific Instruments **81**, 113108 (pages 4) (2010).

[87] R. A. Nyman, G. Varoquaux, B. Villier, D. Sacchet, F. Moron, Y. L. Coq, A. Aspect, and P. Bouyer, Review of Scientific Instruments **77**, 033105 (pages 7) (2006).

[88] D. Voigt, E. Schilder, R. Spreeuw, and H. van Linden van den Heuvell, Applied Physics B: Lasers and Optics **72**, 279 (2001).

[89] N. D. Lemke, A. D. Ludlow, Z. W. Barber, T. M. Fortier, S. A. Diddams, Y. Jiang, S. R. Jefferts, T. P. Heavner, T. E. Parker, and C. W. Oates, Physical Review Letters **103**, 063001 (2009).

[90] T. Middelmann, S. Falke, C. Lisdat, and U. Sterr, Phys. Rev. Lett. **109**, 263004 (2012).

[91] J. A. Sherman, N. D. Lemke, N. Hinkley, M. Pizzocaro, R. W. Fox, A. D. Ludlow, and C. W. Oates, Phys. Rev. Lett. **108**, 153002 (2012).

[92] W. Mende, K. Bartschat, and M. Kock, Journal of Physics B: Atomic, Molecular and Optical Physics **28**, 2385 (1995).

[93] K. Vant, J. Chiaverini, W. Lybarger, and D. J. Berkeland (2006).

[94] S. U. Haq, S. Mahmood, M. A. Kalyar, M. Rafiq, R. Ali, and M. A. Baig, The European Physical Journal D - Atomic, Molecular, Optical and Plasma Physics **44**, 439 (2007).

[95] R. L. Targat, J.-J. Zondy, and P. Lemonde, Optics Communications **247**, 471 (2005).

[96] Y. Shimada, Y. Chida, N. Ohtsubo, T. Aoki, M. Takeuchi, T. Kuga, and Y. Torii, Review of Scientific Instruments **84**, 063101 (pages 7) (2013).

[97] B. Wang, J. W. Zhang, C. Gao, and L. J. Wang, Opt. Express **19**, 16438 (2011).

[98] S. ul Haq, S. Mahmood, N. Amin, Y. Jamil, R. Ali, and M. A. Baig, Journal of Physics B: Atomic, Molecular and Optical Physics **39**, 1587 (2006).

[99] S. G. Porsev, A. D. Ludlow, M. M. Boyd, and J. Ye, Physical Review A **78**, 032508 (pages 9) (2008).

[100] G. Giusfredi, A. Godone, E. Bava, and C. Novero, Journal of Applied Physics **63**, 1279 (1988).

[101] J. Deiglmayr, M. Aymar, R. Wester, M. Weidemüller, and O. Dulieu, The Journal of Chemical Physics **129**, 064309 (2008).

[102] M. S. Chapman, Ph.D. thesis, MIT (1995).

[103] H. Goldstein, C. Poole, and J. Safko, *Classical Mechanics* (Addison Wesley, 2002), 3rd ed.